UC San Diego
UC San Diego Electronic Theses and Dissertations

Title

RAPID 3D BIOPRINTING OF BIOMIMETIC LIVER TISSUES FOR MODELING HEALTHY AND DISEASE STATES IN VITRO

Permalink

https://escholarship.org/uc/item/0z647878

Author

Ma, Xuanyi

Publication Date

2018

Peer reviewed|Thesis/dissertation

UNIVERSITY OF CALIFORNIA SAN DIEGO

RAPID 3D BIOPRINTING OF BIOMIMETIC LIVER TISSUES FOR

MODELING HEALTHY AND DISEASE STATES IN VITRO

A dissertation submitted in partial satisfaction of the

requirements for the degree Doctor of Philosophy

in

Bioengineering

by

Xuanyi Ma

Committee in charge:

       Professor Shaochen Chen, Chair
       Professor Yingxiao Wang, Co-Chair
       Professor Shu Chien
       Professor Gen-Sheng Feng
       Professor Farah Sheikh

2018

The Dissertation of Xuanyi Ma is approved, and it is acceptable in quality and form for publication on microfilm and electronically:

_____

_____

_____

_____
                                                          Co-chair

_____
                                                          Chair

University of California San Diego

2018

DEDICATION

To my beloved husband and parents

EPIGRAPH

The heart of the discerning acquires knowledge, for the ears of the wise seek it out.

Proverbs 18:15

TABLE OF CONTENTS

LIST OF ABBREVIATIONS

ABAM	Antibiotic/Antimycotic
ADSC	Adipose-derived Stem Cell
AFP	Alpha-fetoprotein
ALB	Albumin
ANOVA	Analysis of Variance
ATP	Adenosine Triphosphate
BMP4	Bone Morphogenetic Protein 4
CYP	Cytochrome P450
dECM	Decellularized Extracellular Matrix
DLP	Digital Light Processing
DMD	Digital Micromirror Device
DNA	Deoxyribonucleic acid
DOPsL	Dynamic Optical Projection Stereolithography
DPBS	Phosphate Buffered Saline without Calcium and Magnesium
ECM	Extracellular Matrix
ELISA	Enzyme-linked Immunosorbent Assay
FACS	Fluorescence Activated Cell Sorting
FGF2	Fibroblast Growth Factor 2
GAG	Glycosaminoglycans
GAPDH	Glyceraldehyde 3-phosphate Dehydrogenase
HA	Hyaluronic acid
HCC	Hepatocellular Carcinoma
HCM	Hepatocyte Culture Medium
HGF	Hepatocyte Growth Factor
HLC	Hepatocyte Like Cell
HNF4α	Hepatocyte Nuclear Factor 4α
HSC	Hepatic Stellate Cell
HUVEC	Human Umbilical Vein Endothelial Cell
H&E	Hematoxylin and Eosin
KC	Kupffer cell
LAP	Lithium Phenyl-2,4,6-trimethylbenzoylphosphinate
LSEC	Liver sinusoidal Endothelial Cell
MA	Methacrylic Anhydride
NPC	Nonparenchymal cell
OSM	Oncostatin-M
PBS	Phosphate Buffered Saline
PDMS	Polydimethylsiloxane
PEG	Polyethylene Glycol
PEGDA	Polyethylene Glycol Diacrylate
PFA	Paraformaldehyde Phosphate
PMSF	Phenylmethylsulfonyl Fluoride
qPCR	Real-time Polymerase Chain Reaction

SDS	Sodium Dodecyl Sulfate
SEM	Standard Error of the Mean
TTR	Transthyretin
UV	Ultraviolet
2D	Two Dimensional
3D	Three Dimensional
μCOP	Microscale Continuous Printing

LIST OF FIGURES

ACKNOWLEDGEMENTS

I would like to acknowledge Professor Shaochen Chen for his invaluable support as the advisor of my doctoral training and the chair of my committee. Through his mentorship, I learn to develop creative ideas, think critically in big picture, and manage diverse and successful collaborations. I am also very grateful for the guidance and teaching on both research and life from all my committee members: Professors Peter Wang, Shu Chien, Gen-Sheng Feng and Farah Sheikh.

I would also like to acknowledge all the past and present members of the Chen lab, who have been a part of my journey and made me a better scientist: Dr. Justin Liu, for wonderful discussions on ideas and experiments, and providing suggestions on all small and big things; Dr. Xin Qu, for teaching me the importance of details and training me on experiments when I just started; Peter Chung, for providing unique perspectives during many discussions; Pengrui Wang, for all supports as a lab mate and a friend throughout my PhD journey; Dr. Wei Zhu, for sharing experience on solving problems both during experiments and in daily life; Dr. Claire Yu, for kind supports on both writing and experiments; Jacob Schimelman, for all inspiring chats and discussions; all my undergraduate mentees, for helping me with all my projects on weekdays and weekends.

Finally, I would like to thank my husband Dr. Antony Chi Shing Chan, and my parents Guoqiang Ma and Honglin Guo for all their love, care, support, understanding and believing in me throughout this journey.

Chapter 1, in part, is a reprint of the published article, "3D bioprinting of functional tissue models for personalized drug screening and *in vitro* disease modeling." Ma X, Liu

J, Zhu W, Tang M, Lawrence N, Yu C, Gou M, Chen SC. Advanced Drug Delivery Reviews, 2018. The dissertation author was the primary investigator and author of this paper.

Chapter 2, in part, is a reprint of the published article, "Deterministically patterned biomimetic human iPSC-derived hepatic model via rapid 3D bioprinting." Ma X, Qu X, Zhu W, Li Y, Yuan S, Zhang H, Liu J, Wang P, Lai CSE., Zanella F, Feng G-S, Sheikh F, Chien S, Chen SC. Proceedings of the National Academy of Sciences, 2016. This chapter, in part, has also been submitted for publication of the material as it may appear in the Journal of Biomaterials, 2018, Ma X, Yu C, Wang P, Xu W, Wan X, Lai CSE, Liu J, Koroleva-maharajh A, Chen SC. The dissertation author was the primary investigator and author of these papers.

Chapter 3, in full, is a reprint of the published article, "Deterministically patterned biomimetic human iPSC-derived hepatic model via rapid 3D bioprinting." Ma X, Qu X, Zhu W, Li Y, Yuan S, Zhang H, Liu J, Wang P, Lai CSE., Zanella F, Feng G-S, Sheikh F, Chien S, Chen SC. Proceedings of the National Academy of Sciences, 2016. The dissertation author was the primary investigator and author of this paper.

Chapter 4, in full, has been submitted for publication of the material as it may appear in the Journal of Biomaterials, 2018, Ma X, Yu C, Wang P, Xu W, Wan X, Lai CSE, Liu J, Koroleva-maharajh A, Chen SC. The dissertation author was the primary investigator and author of this paper.

Chapter 5, in part, is a reprint of the published article, "3D bioprinting of functional tissue models for personalized drug screening and *in vitro* disease modeling." Ma X, Liu

J, Zhu W, Tang M, Lawrence N, Yu C, Gou M, Chen SC. Advanced Drug Delivery Reviews, 2018. This chapter, in part, is also a reprint of the published article, "Deterministically patterned biomimetic human iPSC-derived hepatic model via rapid 3D bioprinting." Ma X, Qu X, Zhu W, Li Y, Yuan S, Zhang H, Liu J, Wang P, Lai CSE., Zanella F, Feng G-S, Sheikh F, Chien S, Chen SC. Proceedings of the National Academy of Sciences, 2016. This chapter, in part, has also been submitted for publication of the material as it may appear in the Journal of Biomaterials, 2018, Ma X, Yu C, Wang P, Xu W, Wan X, Lai CSE, Liu J, Koroleva-maharajh A, Chen SC. The dissertation author was the primary investigator and author of these papers.

VITA

Education

2012	Bachelor of Engineering, University of Hong Kong
2015	Master of Science, University of California San Diego
2018	Doctor of Philosophy, University of California San Diego

Honors and Awards

2015	Interdisciplinary Research Awards, University of California San Diego
2015	Outstanding Presentation Award, TERMIS World Congress
2016	Frontiers of Innovation Scholars Program Fellowships, University of California San Diego
2017	Institute of Engineering in Medicine Graduate Student Researcher Scholarship, University of California San Diego
2017	Friends of International Center Graduate Student Fellowship, University of California San Diego
2017	Life Science Awards, Merck KGaA
2018	Siebel Scholar Class of 2018, Siebel Foundation

Journal Articles

Chik TK, <u>Ma XY</u>, Choy TH, Li YY, Diao HJ, Teng WK, Han SJ, Cheung KMC, Chan BP. Photochemically crosslinked collagen annulus plug: a potential solution solving the leakage problem of cell-based therapies for disc degeneration. ***Acta Biomaterialia***. 2013;9(9):8128-8139.

Hribar KC, Finlay D, <u>Ma X</u>, Qu X, Ondeck MG, Chung PH, Zanella F, Engler AJ, Sheikh F, Vuori K, Chen SC. Nonlinear 3D projection printing of concave hydrogel microstructures for long-term multicellular spheroid and embryoid body culture. ***Lab on a Chip***. 2015;15(11):2412-2418.

Aung A, Bhullar I, Theprungsirikul J, Davey SK, Lim HL, Chiu YJ, Ma X, Dewan S, McCulloch A, Varghese S. 3D cardiac μtissues within a microfluidic device with real-time contractile stress readout. *Lab on a Chip*. 2016;16(1):153-162.

Zhu W, Ma X, Gou M, Mei D, Zhang K, Chen SC. 3D printing of functional biomaterials for tissue engineering. *Current Opinion in Biotechnology*. 2016;40:103-112.

Ma X, Qu X, Zhu W, Li Y, Yuan S, Zhang H, Liu J, Wang P, Lai CSE., Zanella F, Feng G-S, Sheikh F, Chien S, Chen SC. A deterministically patterned biomimetic human iPSC-derived hepatic model via rapid 3D bioprinting. *Proceedings of the National Academy of Sciences*. 2016;113(8):2206-2211.

Zhu W, Qu X, Zhu J, Ma X, Patel S, Liu J, Wang P, Lai CS, Gou M, Xu Y, Zhang K, Chen SC, Direct 3D bioprinting of prevascularized tissue constructs with complex microarchitecture. *Biomaterials*. 2017;124:106-115.

Huang Q, Lee J, Arce FT, Yoon I, Angsantikul P, Liu J, Villanueva J, Thamphiwatana S, Ma X, Zhang L, Chen SC, Lal R, Sirbuly DJ, Nanofiber optic force transducers with sub-piconewton resolution via near-field plasmon-dielectric interactions. *Nature Photonics*. 2017;11:352–355.

Ma X, Liu J, Zhu W, Tang M, Lawrence N, Yu C, Gou M, Chen SC, 3D bioprinting of functional tissue models for personalized drug screening and in vitro disease modeling, *Advanced Drug Delivery Reviews*. 2018; In press.

Ma X, Yu C, Wang P, Xu W, Wan X, Lai CSE, Liu J, Koroleva-maharajh A, Chen SC, 3D bioprinted liver dECM-based scaffold with tunable stiffness for studying liver cancer growth and invasion under cirrhotic mechanical environment, *Biomaterials*. 2018; under review.

Yu C, Ma X, Zhu W, Wang P, Miller K, Stupin J, Koroleva-Maharajh A, Hairabedian A, Chen SC, Scanningless and continuous 3D bioprinting of human tissues with decellularized extracellular matrix, *Advanced Functional Materials*. 2018. under review.

Ren J, Han P, Ma X, Farah E, Zeng XI, Bloomekatz J, Zhang R, Kim J, Witty AD, Knight HG, Deshpande R, Xu W, Yelon D, Chen SC, Chi NC, Canonical Wnt5b signaling directs outlying Nkx2.5+ mesoderm into cardiac pacemaker cells, *Nature*. 2018. In preparation.

Ma X, Dewan S, Liu J, Lawrence N, Tang M, Miller K, McCulloch AD, Chen SC, 3D printed micro-scale force gauge towards high throughput platform for human cardiac tissue maturation and drug testing, *Lab on a chip*. 2018. In preparation.

ABSTRACT OF THE DISSERTATION

RAPID 3D BIOPRINTING OF BIOMIMETIC LIVER TISSUES FOR MODELING

HEALTHY AND DISEASE STATES IN VITRO

by

Xuanyi Ma

Doctor of Philosophy in Bioengineering

University of California San Diego, 2018

Professor Shaochen Chen, Chair
Professor Yingxiao Wang, Co-Chair

Drug-induced liver toxicity is the leading cause of acute liver failure and post-market drug withdrawals. In addition, liver associated chronic diseases are major contributors of morbidity and mortality in the United States. Conventional animal models are often costly and unreliable in translation to human studies. Therefore, effective *in vitro* human liver models that can recapitulate native liver function and disease states are highly demanded to better understand disease mechanism and serve as drug screening platforms.

Over the past decades, liver tissue engineering has made significant progress towards the establishment of in vitro liver models for both fundamental pathophysiological

studies and drug screening. However, current platforms are still limited of in terms of their inability to reproduce complex liver microarchitecture, maintain long-term liver functions and reproduce cellular behaviors in diseased conditions. Rapid 3D bioprinting technology, with its potential to pattern cells and biomaterials in a precise manner, provides a great tool to build novel and biomimetic liver models with increasing structural complexity.

In this dissertation, I present the application of digital light processing (DLP)-based rapid 3D bioprinting technology to build *in vitro* liver tissue constructs for modeling healthy and disease conditions. To address the need of liver models for personalized drug screening, I developed a 3D triculture model that embeds human induced pluripotent stem cell (iPSC)-derived hepatic cells with supporting cells in a biomimetic hexagonal architecture. In comparison with 2D monolayer culture and a 3D hepatic cell-only model, the 3D triculture model demonstrates enhancements in liver-specific gene expression, functions and drug metabolism potential. Furthermore, to study liver cancer progression in fibrotic matrix conditions, a liver cancer invasion model possessing tissue-scale organization and patterning of distinct regional stiffness was developed. Tumor cells in cirrhotic condition demonstrated reduced growth along with upregulated invasion markers compared to healthy controls. Cancer stromal invasion from the nodule with cirrhotic stiffness was also visualized using the cancer invasion model. Overall, these models demonstrate the capability of DLP-based 3D bioprinting to build novel and complex structure that mimic native liver tissues in various conditions, and the potential to be applied to *in vitro* drug testing and disease modeling.

Chapter 1 Introduction

1.1 Liver function and gross anatomy

The liver is the largest and heaviest internal organ in the human body, consists of 4 distinct lobes - the left, right, caudate, and quadrate lobes (1). It is roughly triangular in shape and extends across the entire abdominal cavity just inferior to the diaphragm (1). The liver is made of pinkish-brown tissues encapsulated by a connective tissue capsule, which is reinforced by the peritoneum to hold it in place within the abdominal cavity. The organ receives blood through the hepatic portal vein and then drains the blood into the hepatic veins that lead to the vena cava and return to the heart (2). It also has its own system of arteries and arterioles that provide oxygenated blood to support liver tissues.

The liver carries out more than 500 functions, which can be divided mainly into six categories including digestion, proteins production, storage, metabolism, immunity, and detoxification (2, 3). It has an active role in the digestion process through the secretion of bile that is collected through hepatic duct into gallbladder. Bile then released into the duodenum from gallbladder assists lipid digestion. Many essential compounds in blood, including clotting factors, heparin, and albumin, are produced by the liver (3). Plenty of important fat soluble compounds, vitamins and minerals - such as vitamins A, D, E, K, and the iron and copper - are stored in the liver before their consumption by cells throughout the body (3). The liver is also the major storage site for glycogen and serves an essential role to adjust blood glucose levels through the processes of glycogenolysis, glycogenesis, or gluconeogenesis (3). Fatty acids and amino acids in the blood passing through the liver

can also be metabolized and processed to produce energy in the form of adenosine triphosphate (ATP).

In addition to its role in the synthesis and storage of many essential compounds, the liver has a crucial role in the removal of toxic compounds from the body system, such as cellular metabolic waste and xenobiotics (4). It is responsible for the breakdown of bilirubin from the breakdown of hemoglobin in dying red blood cells. It also metabolizes and excretes ethanol, drug compounds and toxins through three phases of enzymatic reactions and processing. The final excreted products are largely excreted through bile and urine (5). Lastly, the liver functions as part of the immune system through capturing and digesting bacteria, fungi, parasites, blood cells, and cellular debris when blood passes the sinusoids.

1.2 Liver lobule, cell population and extracellular matrix composition

The hepatic lobule is defined as a hexagonal region of parenchyma surrounding the central vein at the microscopic or histological scale (Figure 1a) (6, 7). It is the building block of the liver matter, consisting of portal triads, layers of hepatocytes between a sinusoidal capillary network, and a central vein. Blood from each of the portal triad, which is composed of a portal vein and hepatic artery, and a bile duct positioned at the periphery of the lobule, flows through liver parenchyma via the capillary network and drains to the central vein. Liver parenchyma is in close proximity to sinusoidal capillaries (Figure 1b), which have fenestrated endothelium to maximize molecular diffusion in between blood and hepatocytes (6, 7). Bile canaliculi however run in parallel but opposite direction to the

liver sinusoids to collect bile from hepatocytes, and merge with the biliary tree to deliver bile towards gall bladder (6, 7).

The liver lobule consists of parenchymal cells, i.e., hepatocytes, and nonparenchymal cells (NPCs). Hepatocytes constitute around 60% of the cell number and 80% of the total liver volume, and perform the majority of numerous liver functions (8). They are polarized cells arranged in plates with basolateral side of the membrane communicating with the hepatic sinusoid, while the apical part of the membrane facing the bile canaliculus (Figure 1b) (2, 7). The two domains of the membrane are separated by tight junctions. The basolateral membrane of the hepatocyte is covered with microvilli which extend into the perisinusoidal space between the hepatocyte and the endothelial layer, called the space of Disse. These microvilli structures facilitate the interactions between the hepatocyte and the blood plasma by greatly expanding the cell surface area (2).

Nonparenchymal cells in liver constitute around 40% of the cell number and 6.5% of the total liver volume (2, 7). They are largely located in the sinusoidal compartment of the tissue (Figure 1b). Liver sinusoidal endothelial cells (LSECs) form a fenestrated endothelium of the sinusoidal capillaries and constitute 20% of the total liver cell number (2, 7). They interact with other liver cell types through the secretion of cytokines, growth factors, and other compounds into the circulation. LSECs also secrete autocrine vasoactive compounds to regulate blood flow. Kupffer cells (KCs), representing only a small portion of all liver cells, are star-shaped immune cells located in the sinusoidal vessels (2). They secrete inflammatory cytokines and growth factors in response to various stimuli. They are responsible to eliminate damaged blood cells, cancer cells, and liver cells, as well as

bacteria and other foreign entities. Hepatic stellate cells (HSCs), representing 5-8% of the liver cell population, are located in the space of Disse (2). In their quiescent state, HSCs are responsible for the storage of lipid droplets and fat soluble compounds such as vitamin A. Upon activation by physical or chemical signals, spindle-shaped HSCs transdifferentiate into myofibroblast morphology and are highly involved in liver extracellular matrix (ECM) modification. Cholangiocytes are epithelial cells lining the extrahepatic and intrahepatic bile ductules and are responsible for secreting electrolytes and other components of bile (2). Altogether, NPCs have respective roles in the liver and also communicate with hepatocytes and each other through paracrine signaling to function and regulate liver homeostasis.

Liver ECM, though accounts for only 10% volume of the organ, provides essential role to regulate cell functions and activities both in healthy and disease states. Liver ECM consists of largely collagens, and supported by glycoproteins and glycosaminoglycans (GAGs). Fibrillar collagens, including collagens I, III, and V, have triple helix structures compactly arranged in bundles to provide strength and contribute to tissue mechanical property (9). Collagen I, the most prevalent fibrillar collagen, is found largely in the periportal and pericentral regions (10). It provides direct binding sites for cell attachment and also interact with many other ECM components (51). Collagen III is mainly associated with collagen I bundles and can be found throughout liver. Collagen V have thin fibers that link different collagen types together (9). Non-fibrillar collagens in the liver include collagen IV, VI and VIII, with collagen IV being the major constituent of the basement membrane. They have fragmented triple-helical structures that secure other basement

4

membrane proteins like laminin. Fibronectin and laminin are the two major non-collagenous glycoproteins in the liver (9, 10). Plasma fibronectin, produced by hepatocytes, is the most abundant glycoprotein in the tissue. Cellular fibronectin is an insoluble form that exists at low levels in healthy liver tissue. Both forms of fibronectin are important for the injury repair (9). Laminin is found primarily in the basement membrane of the portal region and sinusoidal wall. It provides binding sites for cell attachment and has supports vascular structural together with other ECM components. GAGs are another important ECM components that bind to ECM proteins like collagen, fibronectin, and laminin to promote cell adhesion and function (9). It also binds with many growth factors including hepatocyte growth factor (HGF) to protect them from proteolytic degradation and enhance their utilization by cells. Hyaluronic acid (HA), as one of the GAGs, comprises only a small portion of the liver ECM but contribute significantly to the physical properties of liver (9, 10). HA helps maintain ECM hydration, supports cell motility and liver tissue regeneration.

1.3 Chronic liver diseases

Chronic liver diseases, defined as the progressive loss of liver function, can eventually lead to irreversible end-stage liver disease and failure. There are many types of chronic liver disease. Here the focus is put on liver fibrosis, the subsequent cirrhosis and liver cancer.

1.3.1   Liver fibrosis and cirrhosis

Liver fibrosis, mostly caused by chronic liver damage, is the excessive accumulation of ECM proteins particular collagen (Figure 2) (7, 11). Damages to liver tissue caused by a variety of reasons, including drug toxicity, alcohol or infections, lead to the release of inflammatory mediators and cytokines that can activate HSCs to adopt a myofibroblast phenotype. Activated HSCs proliferate fast and deposit excessive ECM proteins mainly in form of collagen (Figure 2) (7, 11). This loss of balance in ECM synthesis and degradation can mostly be reverted when the cause to damage is not sustained. However, with repetitive damages over time, excessive ECM and continuous HSC activation will aggravate the disease progression. The increase in collagen I throughout liver tissue can initiate further HSC activation and ECM deposition (11). Folds of increase in collagen, laminin and perlecan in the space of Disse of the periportal region can close off the fenestrated sinusoids, blocking molecular diffusion (12). This can lead to a series of detrimental consequences like toxin build-up in the body, insufficient metabolism of compounds like bilirubin and lipid build-up in vessels (11). Portal hypertension can happen in patients with constricted sinusoids and liver vessels. When a significant amount of healthy tissues is replaced by scar tissues, cirrhosis happens and liver loses its function (11). Liver replacement then becomes the only way to cure the disease.

One major consequence of excessive collagen deposition and crosslinking is the increase in liver tissue stiffness. Due to the high correlation of liver tissue stiffness with fibrosis progression, it becomes an important parameter in the prognosis of fibrotic stage(13). Elevated liver stiffness is also a precursor for the development of various liver cancers (14). It is highly correlated with both the tumor appearance and metastatic potential

(15). Increased stiffness is related to increased cancer cell proliferation and resistance to chemotherapeutic agents (15).

1.3.2 Hepatocellular carcinoma (HCC)

HCC is the most common type of primary liver cancer in adults, and is one of the most common cause of cancer-related death worldwide (16). The majority of HCC develops in liver tissues with chronic inflammation particular in the form of advanced liver fibrosis or cirrhosis, which are closely linked to viral hepatitis infection or continuous exposure to toxins like alcohol or aflatoxin. Regardless of its cause, cirrhosis, remains as the most significant risk factor in HCC development and progression (17). Other metabolic syndrome and certain diseases like hemochromatosis also increase the risk of HCC development.

HCC mostly develops within the stiff hepatocellular nodules separated by fibrous septa in an advanced fibrotic or cirrhotic liver. The mitogenic and mutagenic environment in these liver tissues act as a significant contributor to the random genetic and chromosomal damage and lead to the development of HCC. Past studies already demonstrated that chronic immune-mediated liver cell injury is sufficient to cause HCC (18).

In addition to the biochemical factors, liver tissue stiffness has been shown as another significant factor to HCC development and invasion, which are strongly correlated to stiffness values greater than that of healthy liver parenchyma (19, 20). Once developed, tumors progress with local expansion in the nodule, intrahepatic spread through stromal invasion, and distant metastases (21).

1.4 Current *in vitro* liver tissue models and limitations

Over the past decades, liver tissue engineering has made significant progress towards the establishment of *in vitro* liver models for both fundamental pathophysiological studies and drug screening (22–25). The sources of cells used for these *in vitro* liver models include primary hepatocytes, hepatic cell lines isolated from tumors or liver slices, and stem cell-derived hepatic cells (25–27). Monolayer culture, spheroid culture and co-culture platforms have been established using culture dishes (28, 29), micropatterning (30), hanging drop method, commercially available wells (31), microfluidic perfusable chip (32, 33), and physical mask-based additive photopatterning methods (26) (Figure 3). More in-depth discussion will be carried out below on the various types of liver culture models.

1.4.1 Liver models in healthy state

To establish an *in vitro* liver tissue model in healthy state where key hepatic functions are well maintained, mimicking liver tissue microenvironment in terms of 3D microarchitecture, multiple cell types and suitable matrix materials are the keys. In the early days, 2D monolayer culture and sandwiched culture of hepatocytes have been largely carried out. Sandwiched culture of primary hepatocytes have been shown to better maintain hepatocyte phenotypes and functions (34). Despite the success of sandwich culture, it cannot provide the 3D environment as in native liver. Later when 3D patterning and organoid formation emerges, 3D culture becomes more popular. Studies have shown that 3D hepatocyte spheroids exhibit distinct molecular phenotypes when compared to those cultured in sandwiched method (35). Moreover, 3D spheroids have demonstrated higher

metabolic activity and better distinction between the toxic effects of similar drugs compared to sandwiched cultured cells (35).

In addition to mono-culture of hepatocytes alone, various systems have been used to carry out co-culture and tri-culture of hepatocytes with NPCs. The first few successful 2D co-culture systems include the work from Khetani RS and Bhatia SN on micropatterned hepatocyte circle islands surrounded by fibroblasts (26). Similarly, co-culture of hepatocytes with endothelial cells has also been demonstrated (36). More complex co-culture systems that involve 3D co-culture or tri-culture systems have been developed using various methods, including commercially available culture dish (31, 37), microfluidic perfusable chip (32, 33), micropatterned fibrous mats (38). These liver tissue models have demonstrated liver-specific functional improvements when compared to controls using hepatocyte alone or 2D controls.

1.4.2   Liver fibrosis and HCC models

To model liver fibrosis, the most widely used approach is animal model with chemical induced liver damage (39). Nevertheless, recent efforts have been made to develop *in vitro* platforms on studying the effects of some disease parameters on liver cells and functions. The widely used *in vitro* platform to study the effects of pro- or anti-fibrotic compounds on HSC activation is using 2D primary HSC mono-culture (40). Similarly, researches have been carried out to study the effects of matrix stiffness on HSC activation using polyacrylamide gel whose stiffness can be varied based on the degree of polymerization (41). More advanced platforms using monolayer co-culture systems based

on micropatterning (26), transwell (42) or microfluidic systems (43) have been developed to include hepatocytes, HSCs and other relevant cells types. Using these systems, interactions between the cell types can be studied.

For *in vitro* HCC models, the widely used models are monolayer culture and spheroid culture of HCC cells (44). 3D spheroids have gained popularity based on their consistent expression profile, growth and metastatic potential in spite of long term expansion (45). Study of environment factors like ECM stiffness and testing of drugs have been carried out using these these simple models.

1.4.3 Needs for better *in vitro* liver tissue models

Despite the various methods used to create complex 3D co-culture systems, the liver specific functions of hepatocytes cultured in such platforms still declined over weeks of *in vitro* culture (25, 28, 29, 46, 47). More complex platforms that not only create a 3D environment and co-culture of various cell types, but also better recapitulate liver 3D cellular assembly in a biomimetic way are in great needs. In addition, patient-specific platforms are becoming more and more important due to the large variations between individual therapeutic response and tolerance to drug toxicity. Human induced pluripotent stem cells (iPSC)-derived hepatocytes become preferred candidates as cell source than primary hepatocytes which were used by most of the past studies.

Current *in vitro* fibrosis models are largely based on monolayer culture and simple spheroid culture. There is no system that demonstrates incorporation of multiple fibrotic liver features like stiffness, 3D culture, and distorted tissue architecture. HCC models that

can recapitulate the fibrotic or cirrhotic conditions from which they develop are in great needs to better carry out pathophysiological studies and test drugs *in vitro*. Advanced technologies like 3D bioprinting, with capability to pattern cells and biomaterials in a precise manner to form complex microscale structures, becomes a promising tool to achieve novel and biomimetic *in vitro* liver models.

1.5 3D bioprinting in liver tissue engineering

Three dimensional (3D) bioprinting, an extension of 3D printing, is based on additive manufacturing technology and provides controlled fabrication of 3D structures in all X, Y, and Z directions (48–50). The complex structures to be formed can be designed using a computer-aided design (CAD) software or scanned from medical images including magnetic resonance imaging (MRI) or computed tomography (CT) scans (51, 52). 3D bioprinting has emerged as a promising technology for fabricating complex tissue constructs with tailored biological components and mechanical properties (48). By utilizing this transformative technology, bioinks, including hydrogels, cells, and growth factors, can be precisely positioned to create 3D *in vitro* culture environments (53, 54). In this way, native tissue architecture, cellular composition and vasculature can be recapitulated *in vitro* to create biomimetic tissue models, which can be used for studying disease mechanisms, screening drugs and other clinical applications (55, 56). The application of this technology is particularly attractive and useful to engineer liver tissue where hepatocytes and supporting NPCs are arranged in a 3D complex hexagonal lobule unit to support liver functions.

1.5.1 3D printing technology

3D bioprinting has the advantage of reconstructing complex structures from CT or MRI images and producing accurate structures from predetermined digital designs such as CAD models. In order to build functional tissue models, the combination of 3D bioprinting technology with appropriate choice of cells and biomaterials is essential (48, 57, 58). The fabrication capability of the 3D printer and the requirement on materials are highly dependent on the type of printer (59, 60). The choice of cell source also leads to various application potentials of the tissue model, whether it being drug testing or disease modeling (61, 62). The primary types of 3D bioprinting technologies include inkjet-based, extrusion-based, and light-assisted printing (Figure 4). Each of the 3D printing approaches has the capability to both print scaffolds for cell seeding and encapsulate cells directly within scaffolds to build tissue constructs. However, these platforms differ in various aspects including their printing mechanisms, resolution, time, and material choice.

Inkjet-based bioprinting systems are modified from conventional desktop inkjet printers to dispense precise picoliter droplets of bioink (material solution or cell-material mixture) on printing stage (Figure 4a) (63, 64). For current inkjet-based bioprinters, a printing speed in the range of hundreds of millimeters per second and a printing resolution as high as 20 μm has been reported (57, 65). Resolution of the printed constructs relies on the nozzle diameter as well as the properties of the bioink. Smaller diameter nozzle heads generally render higher printing resolution but also increases the potential for clogging, thus the variety of materials that can be printed with inkjet-based method is limited. Generally, only materials with relatively low viscosity or water-based materials are suitable

in order to minimize the chance of clogging. This requirement in turn limits the size and structural integrity of the constructs produced by this printing technology. While inkjet-based method is flexible and inexpensive, the limitations on materials, frequent nozzle clogging, slow printing speed due to point-by-point deposition, and potential damage to cells from shear or thermal stress are issues waiting to be resolved before the expansion of its applications to building more complex tissue models.

Extrusion-based bioprinting systems deposit continuous filaments compared to the individual droplets of inkjet-based bioprinters (Figure 4b). This technology uses a set of automated motors to control the stage or the printer nozzle and a dispensing system to deposit bioink at a precise time and location that is digitally controlled by a computer. For microscale nozzle printing, a more versatile selection of bioinks are compatible with this technology. These include cell spheroid suspension, decellularized extracellular matrix (dECM) solutions, and hydrogels with a wider range of viscosity such as poly(ethylene glycol) (PEG)-based hydrogels, gelatin, HA, and alginate (66–69). Printing of more viscous hydrogels can provide a stronger mechanical support in the final structure. Notably, the flexibility of using more biocompatible inks during extrusion-based printing also make it more suitable for building a variety of tissue models. In addition to the wider choice of printing materials, extrusion-based printing is also advantageous in terms of printing and deposition speed as well as upscaling potential. However, extrusion-based bioprinting has the lowest reported printing speed among the three types of printing approaches, in the range of 10 to 50 µm/s (48, 57). Additionally, the resolution of the printed constructs is generally compromised to allow for 3D structures with a larger footprint. The reported

minimal printed feature resolution can be 5μm but is generally over 100 μm (48, 67, 70). Extrusion-based printing also suffers from shear induced cell death, which is similar to inkjet printing technology (48, 67, 70).

Light-assisted bioprinting methods have gained popularity in recent decades for their high cell viability post-printing as well as superior printing speed and resolution. Among the many types of light assisted technology, Digital light processing (DLP)-based platform is the most commonly used for bioprinting applications. It utilizes a digital micro-mirror device (DMD) chip, a motorized translational stage, and a motorized printing head that are all controllable by computer (Figure 4c) (71, 72). The DMD chip consists of around two million micro-mirrors, which allows for precise light projection patterning as each micro-mirror can be turned on or off independently throughout the printing process. The illumination of UV light or other light source projects onto the pre-polymer solution only when the micro-mirror is in its arbitrary "on" state (57). Two bioprinting systems, dynamic optical projection stereolithography (DOPsL) and microscale continuous printing (μCOP), emerged recently as DLP-based bioprinting platforms with DOPsL highlighting the dynamic printing while μCOP highlighting the continuous printing.

The resolution of DLP-based printers is usually at the microscale level, depending on the focal size of the light beam from each of the micro-mirrors. With DLP-based bioprinting, there is no artificial interface between dots as with inkjet printing or between lines as with extrusion-based printing. This is because an entire plane of pattern is projected onto the prepolymer solution all at once, and the stage moves while the printing patterns continuously refresh. Absence of the artificial interfaces results in better mechanical

integrity of the printed structure. DLP-based printers fabricate the entire volume of a structure in a few seconds such that the printing speed is based on a volumetric scale of a few cubic millimeter per second, which is much faster than the printing speed of other conventional approaches (57). The flexible pattern input, rapid printing speed, and high printing resolution allow researchers to build complex structures with high precision, including microwells (73), microfluidic mixing chambers (74), complex tissue structure (75–79), fractal geometries (80), and constructs with tunable Poisson ratios (81, 82). Materials that are compatible with this printing technique include various photopolymerizable polymers, such as gelatin methacrylate (GelMA), poly(ethylene glycol) diacrylate (PEGDA), and glycidyl methacrylate hyaluronic acid (GMHA). While the material selection is confined within photopolymerizable materials, the limitation can be mitigated with the expanding library of photocurable materials.

With the highest printing resolution and speed compared to inkjet-based and extrusion-based 3D printers, DLP-based bioprinting has the greatest potential to build complex tissue structures with microscale resolution for liver tissue engineering. With the capability of modulating scaffold mechanical property, DLP-based bioprinting can also be used to print liver disease models.

1.5.2 Cells for bioprinting

To build 3D printed *in vitro* liver tissue models, cells are encapsulated into the scaffolds during the printing process. In particular, a cell suspension solution is premixed

with the biomaterial solution and allowed to solidify through various methods such as light exposure in the case of DLP-based 3D printing approach.

In general, there are mainly three sources of cells commonly used for building 3D printed liver tissue models: primary hepatocytes, liver cell lines, and stem cell-derived cells. Primary hepatocytes are great candidates to recapitulate the liver-specific tissue functions. However, they quickly lose functions in many of the *in vitro* culture conditions (83). Also their availability is low and there are always batch-to-batch or donor-to-donor variations. The tissue constructs that use primary cells are also not patient specific, making it less preferable for personalized platforms. Liver cell lines are good candidates for trial studies and cancer studies. They are cheaper and easily accessible, and likely have standard culture procedure. However, these cells are mostly modified so their structures and functional performance may differ from hepatocytes in healthy liver tissue. Stem cell-derived cell type is the third kind of cells commonly used in 3D printed tissue constructs. When primary cells are less available and cell lines are not ideal, stem cell-derived cells are often good choices to consider. These include mesenchymal stem cells (MSC), embryonic stem cells (ESC) and iPSC-derived cells. In particular, human iPSC-derived cells are gaining increasing popularity for their potential to recapitulate individual differences. They are widely applied in many kinds of *in vitro* tissue models. These cells however still have limitations in that they are often not functionally mature enough and the also there can be inconsistency between differentiation batches (84, 85). Recently co-culture platforms are gaining increasing attention in liver tissue engineering due to the better support they provide on hepatocyte survival and tissue function (75, 76, 86, 87).

16

Including multiple types of cells in the printing process therefore is becoming a more common strategy.

Regardless of the type of cell source chosen, there can always be high variations between cells used for different batches of 3D printing. Such variations come from a variety of sources including but not limited to user handling techniques, culture medium and chemicals (88), variations in culture environment (88), aging and mutations of cells (89–91), and differentiation inconsistency (89). Therefore, implementing certain assays or methods to characterize cells before printing is essential to achieve consistency and reproducibility between experiments (92, 93). The specific assay and methods chosen are usually highly cell type dependent, but general characterizations on cell viability, purity and phenotype can be applied to all cell types (75, 93, 94). Such characterizations can also be used following printing to study the impacts on cells due to the cell preparation technique, printing process, and 3D culture method.

1.5.3 Materials for bioprinting

To design tissue scaffolds with the desired physical and chemical properties in 3D bioprinting, proper biomaterial selection is an important consideration. More specifically, biomaterials can be divided into two main categories: naturally-derived (e.g. collagen [30], gelatin (96), fibrin (96), hyaluronic acid (96), silk proteins (96), chitosan (97), alginate (69), dECM (98)) and synthetic (e.g. poly(lactic acid) (PLA) (97), poly(lactic-glycolic) acid (PLGA) (99), PEGDA (74)). Naturally-derived materials are attractive because the complexity of their biophysical and biochemical constituents closely recapitulate the native

17

extracellular matrix (ECM). In turn, these intrinsic properties have been demonstrated to strongly support cell adhesion, proliferation, differentiation, migration, and biocompatibility (100). However, natural biomaterials are often mechanically weak with higher potential for variation between batches. Synthetic materials are highly defined and can be easily reproduced to control for a wide range of properties including degradation rate, cell adhesive moieties, mechanical strength, and structure (100). For instance, synthetic polymer backbones can be decorated with cell recognition peptides sequences such as RGD and YIGSR to improve cell adhesion onto the substrates (101). This flexibility enables the user to adopt a bottom-up approach to engineer a microenvironment mimicking the chemical and physical elements of the ECM found *in vivo*. Despite these advantages, it remains difficult to fully recapitulate components of the native tissue ECM artificially and the potential for poor tissue integration as well as the production of cytotoxic degradable byproducts may pose concerns with respect to long term biocompatibility (102).

As we move towards the production of biomimetic tissues there is an increasing need to develop novel biomaterials that possess complex biophysical and biochemical cues to promote tissue-specific function and maturation. While most naturally-derived bioinks for liver tissue printing utilize gelatin, collagen, and hyaluronic acid these materials only represent single components of the ECM and lack other important constituents such as growth factors, proteoglycans, glycosaminoglycans, laminin, fibronectin, and elastin (103). As a result, the use of dECM derived from liver tissues has gained interest for applications in tissue engineering and regenerative medicine. The process of decellularization aims to

remove all cellular components using a combination of mechanical, chemical, and enzymatic treatments to yield a collagenous matrix material while retaining constituents of the native ECM. Studies have also demonstrated that ECM derived from different tissues are compositionally distinct and cells respond to these matrices in a tissue-specific manner that is important in maintaining phenotype and functionality (103–105).

In addition to supporting cell viability and functions, other material properties are also in consideration to ensure the compatibility to the printing systems. In the context of 3D bioprinting, the biomaterials must be able to quickly form a hydrogel network during the printing process either through chemical or physical crosslinking mechanisms. In the case of light-assisted 3D bioprinting systems crosslinking is achieved through free-radical polymerization of photopolymerizable bioinks (106). Therefore, the system is limited to photocurable bioinks which requires synthetic and natural biomaterials to be functionalized with photocrosslinkable groups such as PEGDA, GelMA, and GMHA. In addition, the opacity of the chosen biomaterial is also an important consideration since this will impact the light penetration depth and subsequently affect the resolution and quality of the final structure (107).

The choice of biomaterials for liver tissue bioprinting largely focuses on collagen-based materials to mimic native liver ECM. To build *in vitro* tissue models for disease modeling and personalized drug screening, research is needed to develop materials with high tunability on the mechanical, chemical, and biological properties to recapitulate the protein composition as well as the native tissue environment at the targeted health stage.

1.5.4 Current 3D printed liver tissue models and limitations

Different 3D bioprinting approaches have been utilized to create liver tissue constructs. Faulkner-Jones et al. reported the use of inkjet-based bioprinter to encapsulate human iPSC and ESC-derived hepatocyte like cells (HLCs) in alginate hydrogels to create 3D ring structures (108). The cell laden alginate droplets were exposed to calcium chloride solution followed by barium chloride before incubating in culture medium (108). The viability and albumin secreting function of HLCs were maintained following this valve-based bioprinting. Kang et al. used extrusion-based bioprinting to generate a 3D hepatic structure (109). Here, a five-layer alginate scaffold containing mouse induced hepatocyte-like cells, each measuring 25 by 25 millimeters, was constructed. During *in vitro* culture, the expression of albumin, ASGR1 and HNF4a gradually increased (109). The construct was also transplanted *in vivo* with increased proliferation and higher albumin expression observed (109). This work demonstrated the use of 3D bioprinted liver scaffold as an effective option for liver therapy. Kizawa et al. also demonstrated a scaffold-free 3D bioprinting technology to build liver tissue that could stably maintain bile acid secretion as well as drug, glucose, and lipid metabolism for weeks (110). This was achieved by connecting spheroids of human primary hepatocytes using the 3D printer. Their work provided insight on the long term culture of 3D bioprinted liver construct *in vitro*. In particular, the group studied the expression and activity of CYP3A4 enzymes and showed that both were maintained for around a period of 2 months. Directly printing into a microfluidic chamber to build liver-on-a-chip platform has also been demonstrated by Bhise and colleagues (111). Droplets of HepG2 spheroid-GelMA mixture were printed on

a glass slide within the cell culture chamber of a bioreactor, followed by immediate UV crosslinking (111). The engineered hepatic construct expressed liver-specific proteins during the 30-day culture period (111).

The applications of inkjet-based and extrusion-based 3D printing technology to build *in vitro* liver models as shown in the above examples have demonstrated great benefits in providing long term *in vitro* culture with good viability and liver-specific gene and protein expressions. Nevertheless, limited studies using 3D printing have demonstrated the capability of stem cell-derived hepatocytes in maintaining liver-specific functions and drug metabolism potential over weeks to months. Further work on recapitulating the complex liver structure, cell population and ECM is needed to promote *in vitro* hepatocyte functional maintenance and drug metabolizing potential.

1.6. Acknowledgments
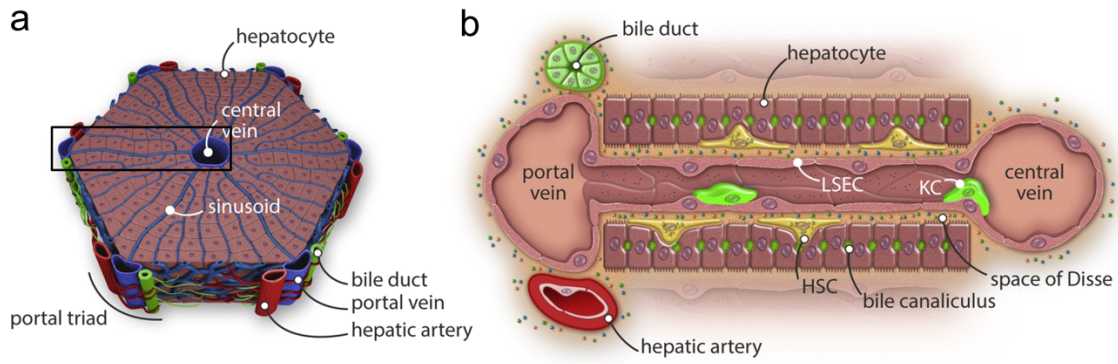
Figure 1-1. Schematic diagram of liver lobule structure, adapted from van Grunsven LA (7). (a) A hexagonal liver lobule unit. (b) Section of liver lobule (black rectangle of panel a) illustrating cell population and arrangement around portal triad, sinusoid and central vein.
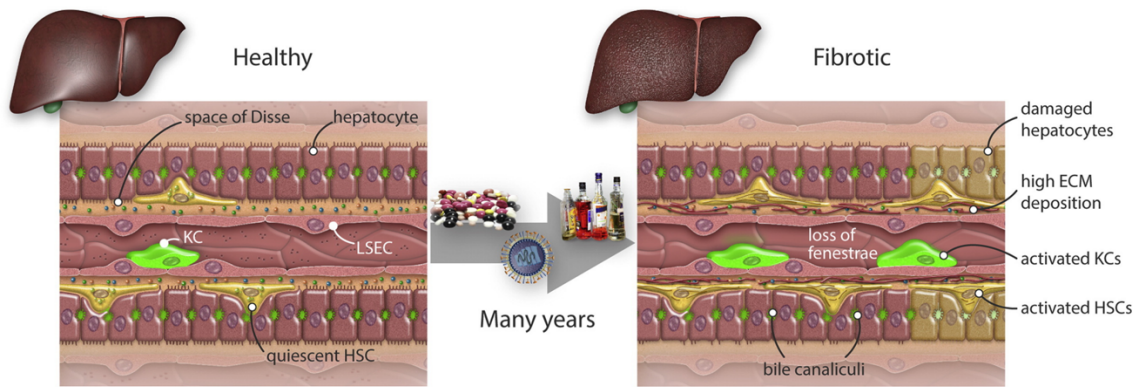
Figure 1-2. Schematic diagram representing a healthy and a fibrotic sinusoid, adapted from van Grunsven LA (7). Upon repetitive hepatocyte damage (yellowish hepatocyte), HSCs proliferate and acquire a myofibroblast phenotype characterized by less lipid droplets, more stress fibers and an increased ECM deposition. LSECs lose fenestrae and KCs expand and acquire a profibrotic phenotype.
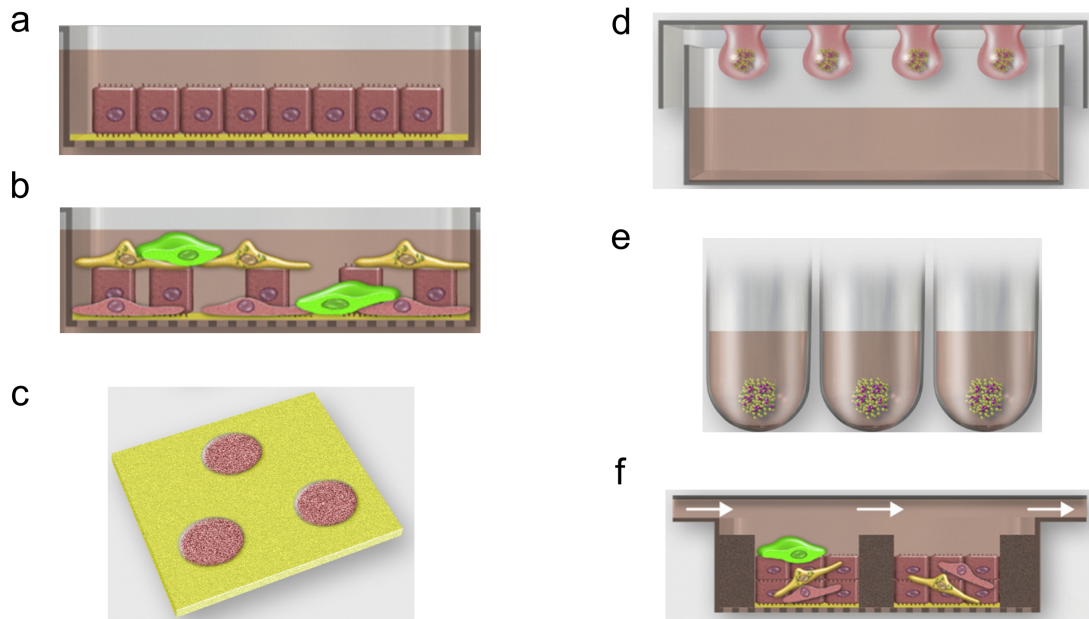
Figure 1-3. Schematic diagrams of commonly adopted liver tissue models and culture methods, adapted from van Grunsven LA (7). (a) Monolayer culture in dish. (b) Co-culture in dish. (c) Patterned co-culture via micropatterning. (d) Spheroid culture by hanging drop method. (e) Spheroid culture by commercially available wells. (f) Co-culture in microfluidic perfusable chip.
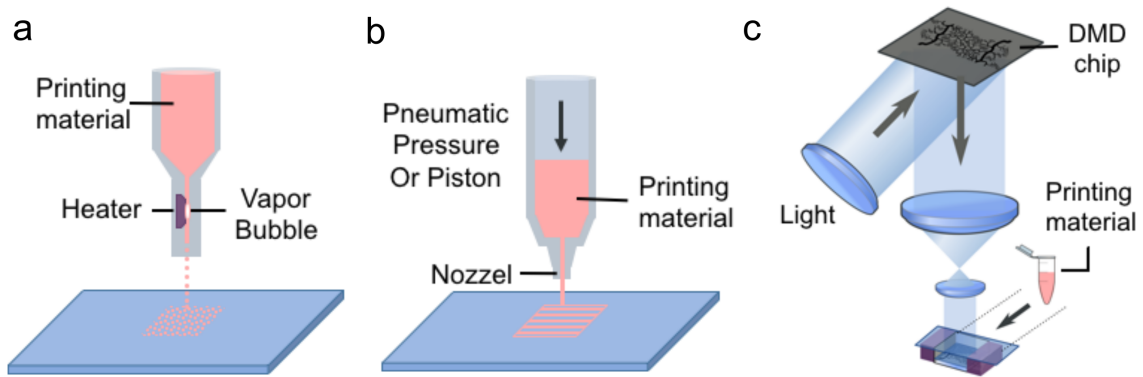
Figure 1-4. Schematic diagrams illustrating the 3D printing approaches. (a) Inkjet-based bioprinting systems. (b) Extrusion-based bioprinting systems. (c) DLP-based bioprinting platforms.

1.7 References

1. R. M. Juza and E. M. Pauli, "Clinical and surgical anatomy of the liver: A review for clinicians," Clin. Anat. **27**, 764–769 (2014).

2. D. S. Irwin Arias, Allan Wolkoff, James Boyer, *The Liver: Biology and Pathobiology* (2011).

3. J. K. Corless and H. M. Middleton, "Normal liver function. A basis for understanding hepatic disease.," Arch. Intern. Med. **143**, 2291–4 (1983).

4. E. L. LeCluyse, R. P. Witek, M. E. Andersen, and M. J. Powers, "Organotypic liver culture models: meeting current challenges in toxicity testing.," Crit. Rev. Toxicol. **42**, 501–48 (2012).

5. C. Xu, C. Y.-T. Li, and A.-N. T. Kong, "Induction of phase I, II and III drug metabolism/transport by xenobiotics.," Arch. Pharm. Res. **28**, 249–68 (2005).

6. D. E. Malarkey, K. Johnson, L. Ryan, G. Boorman, and R. R. Maronpot, "New insights into functional aspects of liver morphology," Toxicol. Pathol. **33**, 27–34 (2005).

7. L. A. van Grunsven, "3D in vitro models of liver fibrosis," Adv. Drug Deliv. Rev. **121**, 133–146 (2017).

8. P. Gissen and I. M. Arias, "Structural and functional hepatocyte polarity and liver disease," J. Hepatol. **63**, 1023–1037 (2015).

9. R. McClelland, E. Wauthier, J. Uronis, and L. Reid, "Gradients in the Liver's Extracellular Matrix Chemistry from Periportal to Pericentral Zones: Influence on Human Hepatic Progenitors," Tissue Eng. Part A **14**, 59–70 (2008).

10. A. Baiocchini, C. Montaldo, A. Conigliaro, A. Grimaldi, V. Correani, F. Mura, F. Ciccosanti, N. Rotiroti, A. Brenna, M. Montalbano, G. D'Offizi, M. R. Capobianchi, R. Alessandro, M. Piacentini, M. E. Schininà, B. Maras, F. Del Nonno, M. Tripodi, and C. Mancone, "Extracellular matrix molecular remodeling in human liver fibrosis evolution," PLoS One **11**, e0151736 (2016).

11. R. Bataller and D. Brenner, "Liver fibrosis," J. Clin. Invest. **115**, 209–218 (2005).

12. I. D. Munsterman, T. Kendall, N. Khelil, M. Popa, R. Lomme, J. P. H. Drenth, and E. T. T. L. Tjwa, "Extracellular matrix components indicate remodelling activity in different fibrosis stages of human non-alcoholic fatty liver disease," Histopathology (2018).

13. S. Mueller and L. Sandrin, "Liver stiffness: a novel parameter for the diagnosis of liver disease.," Hepat. Med. **2**, 49–67 (2010).

14. R. Zhang, M. Ma, G. Dong, R.-R. Yao, J.-H. Li, Q.-D. Zheng, Y.-Y. Dong, H. Ma, D.-M. Gao, J.-F. Cui, Z.-G. Ren, and R.-X. Chen, "Increased matrix stiffness promotes tumor progression of residual hepatocellular carcinoma after insufficient heat treatment.," Cancer Sci. **108**, 1778–1786 (2017).

15. J. Schrader, T. T. Gordon-Walker, R. L. Aucott, M. van Deemter, A. Quaas, S. Walsh, D. Benten, S. J. Forbes, R. G. Wells, and J. P. Iredale, "Matrix stiffness modulates proliferation, chemotherapeutic response, and dormancy in hepatocellular carcinoma cells," Hepatology **53**, 1192–1205 (2011).

16. J. Ferlay, I. Soerjomataram, R. Dikshit, S. Eser, C. Mathers, M. Rebelo, D. M. Parkin, D. Forman, and F. Bray, "Cancer incidence and mortality worldwide: Sources, methods and major patterns in GLOBOCAN 2012," Int. J. Cancer **136**, E359–E386 (2015).

17. M. Pinter, M. Trauner, M. Peck-Radosavljevic, and W. Sieghart, "Cancer and liver cirrhosis: implications on prognosis and management," ESMO Open **1**, e000042 (2016).

18. H. Okuda, "Hepatocellular carcinoma development in cirrhosis," Best Pract. Res. Clin. Gastroenterol. **21**, 161–173 (2007).

19. R. Masuzaki, R. Tateishi, H. Yoshida, T. Sato, T. Ohki, T. Goto, H. Yoshida, S. Sato, Y. Sugioka, H. Ikeda, S. Shiina, T. Kawabe, and M. Omata, "Assessing liver tumor stiffness by transient elastography," Hepatol. Int. **1**, 394–397 (2007).

20. W. Ling, Q. Lu, C. Lu, J. Quan, L. Ma, J. Li, D. He, J. Liu, J. Yang, T. Wen, H. Wu, H. Zhu, and Y. Luo, "Effects of vascularity and differentiation of hepatocellular carcinoma on tumor and liver stiffness: In vivo and in vitro studies," Ultrasound Med. Biol. **40**, 739–746 (2014).

21. F. Kondo, "Histological features of early hepatocellular carcinomas and their developmental process: for daily practical clinical application," Hepatol Int **3**, 283–293 (2009).

22. C. Guguen-Guillouzo, A. Corlu, and A. Guillouzo, "Stem cell-derived hepatocytes and their use in toxicology," Toxicology **270**, 3–9 (2010).

23. D. Yoon No, K.-H. Lee, J. Lee, and S.-H. Lee, "3D liver models on a microplatform: well-defined culture, engineering of liver tissue and liver-on-a-chip," Lab Chip **15**, 3822–3837 (2015).

24. S. N. Bhatia, G. H. Underhill, K. S. Zaret, and I. J. Fox, "Cell and tissue engineering for liver disease," Sci. Transl. Med. **6**, 245sr2 (2014).

25. L. G. Sivaraman, A Leach, J K Townsend, S Iida, T Hogan, B J Stolz, D B Fry, R Samson, L D Tannenbaum, S R Griffith, "A microscale in vitro physiological model of the liver: predictive screens for drug metabolism and enzyme induction," Curr. Drug Metab. **6**, 569–591 (2005).

26. S. R. Khetani and S. N. Bhatia, "Microscale culture of human liver cells for drug development.," Nat. Biotechnol. **26**, 120–126 (2008).

27. N. J. Hewitt, M. J. Gómez Lechón, J. B. Houston, D. Hallifax, H. S. Brown, P. Maurel, J. G. Kenna, L. Gustavsson, C. Lohmann, C. Skonberg, A. Guillouzo, G. Tuschl, A. P. Li, E. LeCluyse, G. M. M. Groothuis, and J. G. Hengstler, "Primary hepatocytes: current understanding of the regulation of metabolic enzymes and transporter proteins, and pharmaceutical practice for the use of hepatocytes in metabolism, enzyme induction, transporter, clearance, and hepatotoxicity studies," Drug Metab. Rev. **39**, 159–234 (2007).

28. Y. Du, R. Han, F. Wen, S. Ng San San, L. Xia, T. Wohland, H. L. Leo, and H. Yu, "Synthetic sandwich culture of 3D hepatocyte monolayer," Biomaterials **29**, 290–301 (2008).

29. K. Takayama, K. Kawabata, Y. Nagamoto, K. Kishimoto, K. Tashiro, F. Sakurai, M. Tachibana, K. Kanda, T. Hayakawa, M. K. Furue, and H. Mizuguchi, "3D spheroid culture of hESC/hiPSC-derived hepatocyte-like cells for drug toxicity testing," Biomaterials **34**, 1781–1789 (2013).

30. C.-T. Ho, R.-Z. Lin, R.-J. Chen, C.-K. Chin, S.-E. Gong, H.-Y. Chang, H.-L. Peng, L. Hsu, T.-R. Yew, S.-F. Chang, and C.-H. Liu, "Liver-cell patterning lab c hip: mimicking the morphology of liver lobule tissue.," Lab Chip **13**, 3578–3587 (2013).

31. H. Gaskell, P. Sharma, H. E. Colley, C. Murdoch, D. P. Williams, and S. D. Webb, "Characterization of a functional C3A liver spheroid model.," Toxicol. Res. (Camb). **5**, 1053–1065 (2016).

32. K. Domansky, W. Inman, J. Serdy, A. Dash, M. H. M. Lim, and L. G. Griffith, "Perfused multiwell plate for 3D liver tissue engineering.," Lab Chip **10**, 51–58 (2010).

33. Y.-C. Toh, T. C. Lim, D. Tai, G. Xiao, D. van Noort, and H. Yu, "A microfluidic 3D hepatocyte chip for drug toxicity testing," Lab Chip **9**, 2026–2035 (2009).

34. J. Keemink, M. Oorts, and P. Annaert, "Primary Hepatocytes in Sandwich Culture,"

in *Methods in Molecular Biology (Clifton, N.J.)* (2015), Vol. 1250, pp. 175–188.

35. C. C. Bell, A. C. A. Dankers, V. M. Lauschke, R. Sison-Young, R. Jenkins, C. Rowe, C. E. Goldring, K. Park, S. L. Regan, T. Walker, C. Schofield, A. Baze, A. J. Foster, D. P. Williams, A. W. M. van de Ven, F. Jacobs, J. van Houdt, T. Lähteenmäki, J. Snoeys, S. Juhila, L. Richert, and M. Ingelman-Sundberg, "Comparison of hepatic 2D sandwich cultures and 3d spheroids for long-term toxicity applications: A multicenter study," Toxicol. Sci. **162**, 655–666 (2018).

36. G. Wang, Y. Zheng, Y. Wang, Z. Cai, N. Liao, J. Liu, and W. Zhang, "Co-culture system of hepatocytes and endothelial cells: two in vitro approaches for enhancing liver-specific functions of hepatocytes," Cytotechnology (2018).

37. T. Takebe, K. Sekine, M. Enomura, H. Koike, M. Kimura, T. Ogaeri, R.-R. Zhang, Y. Ueno, Y.-W. Zheng, N. Koike, S. Aoyama, Y. Adachi, and H. Taniguchi, "Vascularized and functional human liver from an iPSC-derived organ bud transplant," Nature **499**, 481–484 (2013).

38. Y. Liu, L. Zhang, H. Li, S. Yan, J. Yu, J. Weng, and X. Li, "Electrospun fibrous mats on lithographically micropatterned collectors to control cellular behaviors," Langmuir **28**, 17134–17142 (2012).

39. B. Delire, P. Stärkel, and I. Leclercq, "Animal models for fibrotic liver diseases: What we have, what we need, and what is under development," J. Clin. Transl. Hepatol. **3**, 53–66 (2015).

40. S. A. Day, A. M. Lakner, C. C. Moore, M.-H. Yen, M. G. Clemens, E. S. Wu, and L. W. Schrum, "Opioid-like compound exerts anti-fibrotic activity via decreased hepatic stellate cell activation and inflammation," Biochem. Pharmacol. **81**, 996–1003 (2011).

41. A. L. Olsen, S. a Bloomer, E. P. Chan, M. D. a Gaça, P. C. Georges, B. Sackey, M. Uemura, P. a Janmey, and R. G. Wells, "Hepatic stellate cells require a stiff environment for myofibroblastic differentiation.," Am. J. Physiol. Gastrointest. Liver Physiol. **301**, G110–G118 (2011).

42. R. Kostadinova, F. Boess, D. Applegate, L. Suter, T. Weiser, T. Singer, B. Naughton, and A. Roth, "A long-term three dimensional liver co-culture system for improved prediction of clinically relevant drug-induced hepatotoxicity," Toxicol. Appl. Pharmacol. **268**, 1–16 (2013).

43. M. J. Powers, K. Domansky, M. R. Kaazempur-Mofrad, A. Kalezi, A. Capitano, A. Upadhyaya, P. Kurzawski, K. E. Wack, D. B. Stolz, R. Kamm, and L. G. Griffith, "A microfabricated array bioreactor for perfused 3D liver culture," Biotechnol.

Bioeng. **78**, 257–269 (2002).

44. A. Takai, V. Fako, H. Dang, M. Forgues, Z. Yu, A. Budhu, and X. W. Wang, "Three-dimensional organotypic culture models of human hepatocellular carcinoma," Sci. Rep. **6**, 21174 (2016).

45. L. Broutier, G. Mastrogiovanni, M. M. Verstegen, H. E. Francies, L. M. Gavarró, C. R. Bradshaw, G. E. Allen, R. Arnes-Benito, O. Sidorova, M. P. Gaspersz, N. Georgakopoulos, B. K. Koo, S. Dietmann, S. E. Davies, R. K. Praseedom, R. Lieshout, J. N. M. IJzermans, S. J. Wigmore, K. Saeb-Parsy, M. J. Garnett, L. J. W. Van Der Laan, and M. Huch, "Human primary liver cancer-derived organoid cultures for disease modeling and drug screening," Nat. Med. **23**, 1424–1435 (2017).

46. D. R. Berger, B. R. Ware, M. D. Davidson, S. R. Allsup, and S. R. Khetani, "Enhancing the functional maturity of iPSC-derived human hepatocytes via controlled presentation of cell-cell interactions in vitro.," Hepatology 1–44 (2014).

47. K. Kim, K. Ohashi, R. Utoh, K. Kano, and T. Okano, "Preserved liver-specific functions of hepatocytes in 3D co-culture with endothelial cell sheets," Biomaterials **33**, 1406–1413 (2012).

48. S. V Murphy and A. Atala, "3D bioprinting of tissues and organs.," Nat. Biotechnol. **32**, 773–785 (2014).

49. M. M. Stanton, J. Samitier, and S. Sánchez, "Bioprinting of 3D hydrogels," Lab Chip **15**, 3111–3115 (2015).

50. S. Irvine and S. Venkatraman, "Bioprinting and differentiation of stem cells," Molecules **21**, 1188 (2016).

51. S. F. Collins, "Bioprinting is changing regenerative medicine forever," Stem Cells Dev. **23**, 79–82 (2014).

52. A. A. Giannopoulos, D. Mitsouras, S.-J. Yoo, P. P. Liu, Y. S. Chatzizisis, and F. J. Rybicki, "Applications of 3D printing in cardiovascular diseases," Nat. Rev. Cardiol. **13**, 701–718 (2016).

53. U. Jammalamadaka and K. Tappa, "Recent advances in biomaterials for 3D printing and tissue engineering," J. Funct. Biomater. **9**, 22 (2018).

54. A. Skardal and A. Atala, "Biomaterials for integration with 3-D bioprinting," Ann. Biomed. Eng. **43**, 730–746 (2015).

55. K. Markstedt, A. Mantas, I. Tournier, H. Martínez Ávila, D. Hägg, and P.

Gatenholm, "3D bioprinting human chondrocytes with nanocellulose–alginate bioink for cartilage tissue engineering applications," Biomacromolecules **16**, 1489–1496 (2015).

56. H. Cui, W. Zhu, B. Holmes, and L. G. Zhang, "Biologically inspired smart release system based on 3D bioprinted perfused scaffold for vascularized tissue regeneration," Adv. Sci. **3**, 1600058 (2016).

57. W. Zhu, X. Ma, M. Gou, D. Mei, K. Zhang, and S. Chen, "3D printing of functional biomaterials for tissue engineering," Curr. Opin. Biotechnol. **40**, 103–112 (2016).

58. J. M. Lee and W. Y. Yeong, "Design and printing strategies in 3D bioprinting of cell-hydrogels: A review," Adv. Healthc. Mater. **5**, 2856–2865 (2016).

59. J. Huang, H. Fu, C. Li, J. Dai, and Z. Zhang, "Recent advances in cell-laden 3D bioprinting: materials, technologies and applications," J. 3D Print. Med. **1**, 245–268 (2017).

60. S. Ji and M. Guvendiren, "Recent advances in bioink design for 3D bioprinting of tissues and organs.," Front. Bioeng. Biotechnol. **5**, 23 (2017).

61. A. N. Leberfinger, D. J. Ravnic, A. Dhawan, and I. T. Ozbolat, "Concise review: Bioprinting of stem cells for transplantable tissue fabrication," Stem Cells Transl. Med. **6**, 1940–1948 (2017).

62. W. Peng, P. Datta, B. Ayan, V. Ozbolat, D. Sosnoski, and I. T. Ozbolat, "3D bioprinting for drug discovery and development in pharmaceutics," Acta Biomater. **57**, 26–46 (2017).

63. K. Hölzl, S. Lin, L. Tytgat, S. Van Vlierberghe, L. Gu, and A. Ovsianikov, "Bioink properties before, during and after 3D bioprinting," Biofabrication **8**, 32002 (2016).

64. R. F. Pereira and P. J. Bártolo, "3D bioprinting of photocrosslinkable hydrogel constructs," J. Appl. Polym. Sci. **132**, 42458 (2015).

65. H.-W. Kang, S. J. Lee, I. K. Ko, C. Kengla, J. J. Yoo, and A. Atala, "A 3D bioprinting system to produce human-scale tissue constructs with structural integrity," Nat. Biotechnol. **34**, 312–319 (2016).

66. A. D. Graham, S. N. Olof, M. J. Burke, J. P. K. Armstrong, E. A. Mikhailova, J. G. Nicholson, S. J. Box, F. G. Szele, A. W. Perriman, and H. Bayley, "High-resolution patterned cellular constructs by droplet-based 3D printing," Sci. Rep. **7**, 7004 (2017).

67. I. T. Ozbolat and M. Hospodiuk, "Current advances and future perspectives in extrusion-based bioprinting," Biomaterials **76**, 321–343 (2016).

68. W. Jia, P. S. Gungor-Ozkerim, Y. S. Zhang, K. Yue, K. Zhu, W. Liu, Q. Pi, B. Byambaa, M. R. Dokmeci, S. R. Shin, and A. Khademhosseini, "Direct 3D bioprinting of perfusable vascular constructs using a blend bioink," Biomaterials **106**, 58–68 (2016).

69. E. Axpe and M. L. Oyen, "Applications of alginate-based bioinks in 3D bioprinting," Int. J. Mol. Sci. **17**, E1976 (2016).

70. F. You, B. F. Eames, and X. Chen, "Application of extrusion-based hydrogel bioprinting for cartilage tissue engineering," Int. J. Mol. Sci. **18**, 1597 (2017).

71. K. C. Hribar, P. Soman, J. Warner, P. Chung, and S. Chen, "Light-assisted direct-write of 3D functional biomaterials," Lab Chip **14**, 268–275 (2014).

72. M. Gou, X. Qu, W. Zhu, M. Xiang, J. Yang, K. Zhang, Y. Wei, and S. Chen, "Bio-inspired detoxification using 3D-printed hydrogel nanocomposites.," Nat. Commun. **5**, 3774 (2014).

73. K. C. Hribar, D. Finlay, X. Ma, X. Qu, M. G. Ondeck, P. H. Chung, F. Zanella, A. J. Engler, F. Sheikh, K. Vuori, and S. Chen, "Nonlinear 3D projection printing of concave hydrogel microstructures for long-term multicellular spheroid and embryoid body culture," Lab Chip **15**, 2412–2418 (2015).

74. J. Liu, H. H. Hwang, P. Wang, G. Whang, and S. Chen, "Direct 3D-printing of cell-laden constructs in microfluidic architectures.," Lab Chip **16**, 1430–1438 (2016).

75. X. Ma, X. Qu, W. Zhu, Y.-S. Li, S. Yuan, H. Zhang, J. Liu, P. Wang, C. S. E. Lai, F. Zanella, G.-S. Feng, F. Sheikh, S. Chien, and S. Chen, "Deterministically patterned biomimetic human iPSC-derived hepatic model via rapid 3D bioprinting," Proc. Natl. Acad. Sci. **113**, 2206–2211 (2016).

76. W. Zhu, X. Qu, J. Zhu, X. Ma, S. Patel, J. Liu, P. Wang, C. S. E. Lai, M. Gou, Y. Xu, K. Zhang, and S. Chen, "Direct 3D bioprinting of prevascularized tissue constructs with complex microarchitecture," Biomaterials **124**, 106–115 (2017).

77. S. P. Grogan, P. H. Chung, P. Soman, P. Chen, M. K. Lotz, S. Chen, and D. D. D'Lima, "Digital micromirror device projection printing system for meniscus tissue engineering," Acta Biomater. **9**, 7218–7226 (2013).

78. P. Soman, B. T. D. Tobe, J. W. Lee, A. A. M. Winquist, I. Singec, K. S. Vecchio, E. Y. Snyder, and S. Chen, "Three-dimensional scaffolding to investigate neuronal

derivatives of human embryonic stem cells," Biomed. Microdevices **14**, 829–838 (2012).

79.   C. Cha, P. Soman, W. Zhu, M. Nikkhah, G. Camci-Unal, S. Chen, and A. Khademhosseini, "Structural reinforcement of cell-laden hydrogels with microfabricated three dimensional scaffolds," Biomater. Sci. **2**, 703–709 (2014).

80.   J. Warner, P. Soman, W. Zhu, M. Tom, and S. Chen, "Design and 3D printing of hydrogel scaffolds with fractal geometries," ACS Biomater. Sci. Eng. **2**, 1763–1770 (2016).

81.   J. W. Lee, P. Soman, J. H. Park, S. Chen, and D. W. Cho, "A tubular biomaterial construct exhibiting a negative poisson's ratio," PLoS One **11**, 1–14 (2016).

82.   P. Soman, D. Y. Fozdar, J. W. Lee, A. Phadke, S. Varghese, and S. Chen, "A three-dimensional polymer scaffolding material exhibiting a zero Poisson's ratio," Soft Matter **8**, 4946 (2012).

83.   M. Shulman and Y. Nahmias, "Long-term culture and coculture of primary rat and human hepatocytes.," Methods Mol. Biol. **945**, 287–302 (2013).

84.   S. P. Medvedev, A. I. Shevchenko, and S. M. Zakian, "Induced pluripotent stem cells: problems and advantages when applying them in regenerative medicine.," Acta Naturae **2**, 18–28 (2010).

85.   Y.-C. Li, K. Zhu, and T.-H. Young, "Induced pluripotent stem cells, form in vitro tissue engineering to in vivo allogeneic transplantation.," J. Thorac. Dis. **9**, 455–459 (2017).

86.   L. Gao, M. E. Kupfer, J. P. Jung, L. Yang, P. Zhang, Y. Da Sie, Q. Tran, V. Ajeti, B. T. Freeman, V. G. Fast, P. J. Campagnola, B. M. Ogle, and J. Zhang, "Myocardial tissue engineering with cells derived from human-induced pluripotent stem cells and a native-like, high-resolution, 3-dimensionally printed scaffold," Circ. Res. **120**, 1318–1325 (2017).

87.   F. Xu, J. Celli, I. Rizvi, S. Moon, T. Hasan, and U. Demirci, "A three-dimensional in vitro ovarian cancer coculture model using a high-throughput cell patterning platform," Biotechnol. J. **6**, 204–212 (2011).

88.   T. Yao and Y. Asayama, "Animal-cell culture media: History, characteristics, and current issues," Reprod. Med. Biol. **16**, 99–117 (2017).

89.   G. Morrison, C. Liu, C. Wing, S. M. Delaney, W. Zhang, and M. E. Dolan, "Evaluation of inter-batch differences in stem-cell derived neurons," Stem Cell Res.

16, 140–148 (2016).

90. N. Kinarivala, K. Shah, T. J. Abbruscato, and P. C. Trippier, "Passage variation of PC12 cells results in inconsistent susceptibility to externally induced apoptosis," ACS Chem. Neurosci. **8**, 82–88 (2017).

91. P. Liu, A. Kaplan, B. Yuan, J. H. Hanna, J. R. Lupski, and O. Reiner, "Passage number is a major contributor to genomic structural variations in mouse iPSCs," Stem Cells **32**, 2657–2667 (2014).

92. J. Carmen, S. R. Burger, M. McCaman, and J. A. Rowley, "Developing assays to address identity, potency, purity and safety: cell characterization in cell therapy process development," Regen. Med. **7**, 85–100 (2012).

93. L. Wang, M. Xu, L. Luo, Y. Zhou, and P. Si, "Iterative feedback bio-printing-derived cell-laden hydrogel scaffolds with optimal geometrical fidelity and cellular controllability," Sci. Rep. **8**, 2802 (2018).

94. Y. Fang and R. M. Eglen, "Three-dimensional cell cultures in drug discovery and development.," SLAS Discov. Adv. life Sci. R D **22**, 456–472 (2017).

95. J. A. Inzana, D. Olvera, S. M. Fuller, J. P. Kelly, O. A. Graeve, E. M. Schwarz, S. L. Kates, and H. A. Awad, "3D printing of composite calcium phosphate and collagen scaffolds for bone regeneration," Biomaterials **35**, 4026–4034 (2014).

96. S. Gomes, I. B. Leonor, J. F. Mano, R. L. Reis, and D. L. Kaplan, "Natural and genetically engineered proteins for tissue engineering.," Prog. Polym. Sci. **37**, 1–17 (2012).

97. C. R. Almeida, T. Serra, M. I. Oliveira, J. A. Planell, M. A. Barbosa, and M. Navarro, "Impact of 3-D printed PLA- and chitosan-based scaffolds on human monocyte/macrophage responses: Unraveling the effect of 3-D structures on inflammation," Acta Biomater. **10**, 613–622 (2014).

98. F. Pati, J. Jang, D.-H. Ha, S. Won Kim, J.-W. Rhie, J.-H. Shim, D.-H. Kim, and D.-W. Cho, "Printing three-dimensional tissue analogues with decellularized extracellular matrix bioink," Nat. Commun. **5**, 1–11 (2014).

99. J. D. Kim, J. S. Choi, B. S. Kim, Y. Chan Choi, and Y. W. Cho, "Piezoelectric inkjet printing of polymers: Stem cell patterning on polymer substrates," Polymer (Guildf). **51**, 2147–2154 (2010).

100. T. J. Keane and S. F. Badylak, "Biomaterials for tissue engineering applications," Semin. Pediatr. Surg. **23**, 112–118 (2014).

101. J. Zhu, "Bioactive modification of poly(ethylene glycol) hydrogels for tissue engineering," Biomaterials **31**, 4639–4656 (2010).

102. L. Lu, S. J. Peter, M. D. Lyman, H. L. Lai, S. M. Leite, J. A. Tamada, S. Uyama, J. P. Vacanti, R. Langer, and A. G. Mikos, "In vitro and in vivo degradation of porous poly(DL-lactic-co-glycolic acid) foams.," Biomaterials **21**, 1837–1845 (2000).

103. P. M. Crapo, T. W. Gilbert, and S. F. Badylak, "An overview of tissue and whole organ decellularization processes," Biomaterials **32**, 3233–3243 (2011).

104. V. Russo, C. Yu, P. Belliveau, A. Hamilton, and L. E. Flynn, "Comparison of human adipose-derived stem cells isolated from subcutaneous, omental, and intrathoracic adipose tissue depots for regenerative applications.," Stem Cells Transl. Med. **3**, 206–217 (2014).

105. V. Z. Beachley, M. T. Wolf, K. Sadtler, S. S. Manda, H. Jacobs, M. R. Blatchley, J. S. Bader, A. Pandey, D. Pardoll, and J. H. Elisseeff, "Tissue matrix arrays for high-throughput screening and systems analysis of cell function," Nat. Methods **12**, 1197–1204 (2015).

106. D. B. Kolesky, R. L. Truby, A. S. Gladman, T. A. Busbee, K. A. Homan, and J. A. Lewis, "3D bioprinting of vascularized, heterogeneous cell-laden tissue constructs," Adv Mater **26**, 3124–3130 (2014).

107. W. Zhu, J. Li, Y. J. Leong, I. Rozen, X. Qu, R. Dong, Z. Wu, W. Gao, P. H. Chung, J. Wang, and S. Chen, "3D-printed artificial microfish," Adv. Mater. **27**, 4411–4417 (2015).

108. A. Faulkner-Jones, C. Fyfe, D.-J. Cornelissen, J. Gardner, J. King, Aidan Courtney, and W. Shu, "Bioprinting of human pluripotent stem cells and their directed differentiation into hepatocyte-like cells for the generation of mini-livers in 3D," Biofabrication **7**, 44102 (2015).

109. K. Kang, Y. Kim, S. B. Lee, J. S. Kim, S. Park, W. Kim, H.-M. Yang, S.-J. Kim, J. Jeong, and D. Choi, "Three-dimensional bio-printing of hepatic structures with direct-converted hepatocyte-like cells," Tissue Eng. Part A **24**, 576–583 (2018).

110. H. Kizawa, E. Nagao, M. Shimamura, G. Zhang, and H. Torii, "Scaffold-free 3D bio-printed human liver tissue stably maintains metabolic functions useful for drug discovery," Biochem. Biophys. Reports **10**, 186–191 (2017).

111. N. S. Bhise, V. Manoharan, S. Massa, A. Tamayol, M. Ghaderi, M. Miscuglio, Q. Lang, Y. Shrike Zhang, S. R. Shin, G. Calzone, N. Annabi, T. D. Shupe, C. E. Bishop, A. Atala, M. R. Dokmeci, and A. Khademhosseini, "A liver-on-a-chip

platform with bioprinted hepatic spheroids," Biofabrication **8**, 14101 (2016).

Chapter 2 Methods: Fabrication of a 3D tissue analog via rapid 3D bioprinting of cell-laden photocrosslinkable hydrogels

2.1 Biomaterial synthesis and scaffold characterization

Various photocrosslinkable biomaterials have been used for 3D printing of liver tissue models through DLP-based rapid bioprinting platform (1). In particular, GelMA, as a collagen-based scaffold, is used for supporting hepatocyte culture and functions in healthy liver models. GMHA, a hyaluronic acid-based scaffold, is added to support endothelial cell culture and proliferation as evident from past studies (2). Following the successful model establishment using GelMA and GMHA, printable liver dECM material is then explored as scaffolds for liver disease models. Photoinitiator preparation and scaffold property characterizations are also outlined.

2.1.1 Biomaterial synthesis and preparation

In this section, the synthesis of three types of biomaterials and their printing preparation are described in detail.

GelMA

GelMA was synthesized according to previously published procedures (3, 4). Porcine skin gelatin (Sigma Aldrich) was mixed at 10%(w/v) in phosphate buffered saline without calcium and magnesium (DPBS, Life Technologies) and stirred at 60°C until fully dissolved. Methacrylic anhydride (MA, Sigma Aldrich) was added to the solution at a rate

of 0.5 ml/min until a concentration of 8% (v/v) of MA was achieved in the gelatin solution. The solution was stirred for 3 hours at 60°C. Following a 2X dilution with warm DPBS, the solution was dialyzed against distilled water using dialysis tubing (13.5 kDA cutoff, Spectrum Laboratories) for 1 week at 45°C to remove the unreacted groups from the solution. The dialyzed GelMA solution was frozen overnight at -80°C and lyophilized in a Freeze dryer (Labconco) for one week. Freeze-dried GelMA foam was stored at -80°C until further usage (Figure 1a). Prepolymer solution at a specific concentration (wt/vol) was made by dissolving GelMA foam into DPBS, then sterilized by syringe filters (Millipore), aliquoted, and stored at 4 °C in the dark. The functionalization and subsequent photopolymerization reaction have been illustrated in Figure 1c.

GMHA

GMHA was synthesized according to a modified procedure (2, 5). Hyaluronic acid (200kD, total 1g, Lifecore) was mixed in 100 ml solution of water and acetone mixture (50:50) stirring at room temperature overnight. The solution was then purged with argon. Tri-ethylamine (7.2 ml, Sigma) at 20-fold molar excess was added dropwise. Glycidyl metacrylate (7.2ml, Sigma) at 20-fold molar excess was added dropwise until thoroughly mixed. The solution was covered in aluminum foil and allowed to react overnight. The solution was dialyzed across a tubing (3.5 kDa) against DI water in a beaker. Water was exchanged after 2, 4, and 24 hours. The dialyzed GMHA solution was frozen overnight at -80°C and lyophilized in a Freeze dryer (Labconco) for one week. Freeze-dried GMHA foam was stored at -80°C until further usage. The dialyzed GMHA solution was frozen

38

overnight at -80°C and lyophilized in a Freeze dryer (Labconco) for one week. Freeze-dried GMHA foam was stored at -80°C until further usage (Figure 1b). Prepolymer solution at a specific concentration (wt/vol) was made by dissolving GMHA foam into DPBS, then sterilized by syringe filters (Millipore), aliquoted, and stored at 4 °C in the dark. The functionalization and subsequent photopolymerization reaction have been illustrated in Figure 1d.

Liver dECM

Fresh porcine liver was sourced from three month old healthy Yorkshire pigs (40-45 kg) supplied by S&S Farms (Ramona, CA), which is an approved vendor by the Institutional Animal Care and Use Committee at the University of California San Diego. The pigs were euthanized with an overdose of pentobarbital and the fresh liver tissues were immediately harvested and transported on ice to the lab. Excess blood was rinsed and tissues were stored in DPBS supplemented with 1% (vol/vol) antibiotic/antimycotic (ABAM) (ThermoFisher Scientific) at -80°C prior to decellularization. All steps from tissue procurement to storage was performed within 2-3 h of harvesting to ensure preservation of tissue integrity and quality. For all experiments, at least three entire livers were pooled and processed into liver dECM to minimize potential batch-to-batch variations.

To prepare the liver dECM, all steps were performed in an incubator shaker set to 37°C and 120 rpm and all solutions were supplemented with 1% (vol/vol) ABAM and 0.01 mM phenylmethylsulfonyl fluoride (PMSF) (Sigma Aldrich). Frozen liver tissues were

thawed and minced finely with scissors into 0.5 cm^3 pieces. The minced liver was then subjected to three cycles of freeze thaw with 2 h washes in hypotonic solution in between. The tissues were then rinsed three times with 1X DPBS for 30 min each and washed in 1% (wt/vol) sodium dodecyl sulfate (SDS) (Sigma Aldrich) in DPBS for 48 h with 2-3 solution changes per day until white in appearance. The resulting tissue was rinsed thoroughly in deionized water for an additional 24 h with 2-3 solution changes per day and stored in 70% (vol/vol) ethanol at 4°C until further use. To prepare the liver dECM solution, the liver dECM was decontaminated by washing in 70% (vol/vol) ethanol for 24 h in an incubator shaker. Sterile deionized water was then used to rinse the tissue of residual ethanol for another 24 h prior to freezing and lyophilization for 48 h. Using a RestchTM MM400 mixer mill, the lyophilized liver dECM was loaded into the milling chamber containing two 10 mm stainless steel milling balls, immersed in liquid nitrogen for 3 min, and cryomilled for 2 min. Following this, the liver dECM powder was solubilized using pepsin (Sigma-Aldrich) at 1 mg/mL in 0.1 M HCl for 24 h at room temperature on a bench-top shaker. The solution was then neutralized with NaOH then frozen and lyophilized overnight. Next, the lyophilized solutions were cryomilled again by immersing in liquid nitrogen for 3 min and cryomilled for 2 min to yield a fine powder that can be readily reconstituted. The entire procedure was shown in in Figure 2a.

The process to remove cellular content was optimized to preserve the ultrastructure of the native ECM as well as collagen fibrils and key ECM constituents (Figure 2b). The absence of nuclear staining in the hematoxylin and eosin (H&E) stained sections showed the successful removal of cells. Additional deoxyribonucleic acid (DNA) quantification of

the liver dECM demonstrated a negligible amount of residual DNA of less than 50 ng/mg dry weight (6), which further confirms the successful removal of cellular content (Figure 2c). Following this, the preservation of major ECM constituents was assessed for the liver dECM. The optimized decellularization process was able to retain approximately 30% of GAG content in the liver dECM compared to that of native liver (Figure 2d). Moreover, after decellularization the collagen content was enriched in the liver dECM relative to the native liver control (Figure 2e). To develop photocrosslinkable liver dECM-based hydrogel materials for DLP-based rapid 3D bioprinting, liver dECM was combined with GelMA to produce a printable solution. The reaction mechanism is illustrated in Figure 2f.

2.1.2 Photoinitiator synthesis and preparation

Lithium phenyl-2,4,6 trimethylbenzoylphosphinate (LAP), served as the photoinitiator for the photopolymerization reaction, was synthesized according to previously published procedures (7, 8). The solution of 2,4,6-trimethylbenzoyl chloride (0.018 mol, Acros Organics) was added dropwise to an equimolar amount of continuously stirred dimethyl phenylphosphonite (Sigma Aldrich). The reaction mixture was stirred for 18 hours at room temperature and under argon. The mixture was then heated to 50 ˚C and a four-fold excess of lithium bromide (6.1 g, Sigma Aldrich) in 100 ml of 2-butanone (Sigma-Aldrich) was added. After 10 min, a solid precipitate formed. The mixture was cooled to room temperature, allowed to rest for four hours. The filtrate was washed and filtered 3 times with 2-butanone to remove unreacted lithium bromide and excess solvent

was removed by vacuum. Completely dried samples of LAP powder was stored in dark at -20 °C.

2.1.3 Mechanical property characterization of printed scaffold

Bioprinted constructs in a cylindrical shape (height 250μm and diameter 1mm) were tested for their mechanical properties. The samples were incubated at 37°C and 5% CO_2 following bioprinting until the measurement time points. Mechanical property measurements of the samples were carried out using a commercially available MicroSquisher (CellScale). Before recording measurements, each sample was preconditioned by compressing at 4 μm/s to remove hysteresis caused by internal friction. The compression test was conducted at 10% strain with a 2 μm/s strain rate. The elastic modulus was then calculated using an in-house MATLAB code with the force and displacement data collected from the SquisherJoy software.

Relationships between stiffness and material concentration as well as printing light exposure time were investigated using GelMA. A positive relationship was found between the scaffold mechanical property and the material concentration (Figure 3a). Similar relationship was demonstrated between scaffold mechanical property and printing exposure time (Figure 3b). Specifically, 5% (wt/vol) GelMA, with polymerized matrix stiffness similar to healthy liver tissues (9, 10), was chosen to support iPSC-derived hepatic cells (Figure 3c). GMHA, which has been shown to promote endothelial cell proliferation and support vascularization (2), was mixed at 2% (wt/vol) with 5% (wt/vol) GelMA at a 1:1 ratio for encapsulating the supporting endothelial and mesenchymal cells (Figure 3c).

2.2 Cell preparation and characterization

To print liver tissue model in healthy state, human iPSC-derived hepatic cells, which have potential for patient-specific studies and can avoid donor variations problem of primary human hepatocytes, were chosen. To establish models for HCC, HepG2 cell line was chosen as a stable and commonly used HCC line. Immediately before printing, cells were digested based on their respective protocols and resuspended in medium at a target density depending on application, as described in detail below.

2.2.1 Human iPSC hepatic differentiation and characterization

Integration-free human iPSCs generation and culture

The generation method of human iPSCs was carried out using human perinatal foreskin fibroblasts (ATCC) and human adult dermal fibroblasts (Cell Applications), which were purchased and maintained in Dulbecco's Modified Eagle's Medium (Corning) supplemented with 10% fetal bovine serum (Tissue Culture Biologicals) and ABAM (Corning) in a 37°C, 5% CO_2 incubator. Cells were passaged at a ratio of 1:6 every 3-5 days by 0.25% trypsin-EDTA (Corning) before reprogramming. To prepare for reprogramming, fibroblasts were seeded at a density of 2 x 10^5 cells/well in 6-well plates, and allowed to attach and spread for 48 hours. Reprogramming was performed following the instructions in a Sendai virus-based CytoTune kit (Life technologies) for the delivery of four factors Oct4, Sox2, Klf4 and c-Myc. Following successful reprogramming, matrigel growth factor reduced basement membrane matrix (Corning) was used as the substrate for the maintenance of the iPSCs culture in xeno-free and feeder-free Essential 8 medium (Life

Technologies) following the manufacturer's instructions. Cells were split at a ratio of 1:8 every 3-4 days by Versene (Life Technologies) before experiments.

In vitro iPSC hepatic differentiation

Before the initiation of hepatic differentiation, human iPSCs were dissociated into single cells by using accutase (Innovative Cell Technologies) and plated onto hESC-qualified matrigel substrate (Corning) coated 12-well plates. The seeded plates were incubated overnight at 37°C, 3% O_2 with 7% CO_2. The seeding density was controlled to achieve 80% to 100% confluency within the following day. The hepatic differentiation protocol was based on previous literature with some modifications (Figure 4a) (11). Briefly, induction into definitive endoderm cells was carried out by culturing human iPSCs at 37°C, ambient O_2 with 5% CO_2 for 4 days in HEPES-buffered RPMI1640 medium (Life Technologies), which was supplemented with 100 ng/ml activin A (R&D Systems), 10ng/ml bone morphogenetic protein 4 (BMP4, R&D Systems), 20ng/ml fibroblast growth factor-2 (FGF2, PeproTech) and 2% B27 minus insulin supplement (Life Technologies) for the first 2 days and with only 100 ng/ml activin A and 2% B27 minus insulin supplement for the remaining two days. Subsequent induction into hepatic endoderm cells was carried out by culturing definitive endoderm cells at 37°C, 4% O_2 with 7% CO_2 for 5 days in HEPES buffered RPMI1640 medium (Life Technologies) supplemented by 20ng/ml BMP4, 10ng/ml FGF2 and 2% B27 supplement (Life Technologies). The hepatic progenitor cells (HPCs) at this stage were cultured in 20 ng/ml HGF (PeproTech) and 2% B27 supplemented RPMI1640 medium (Life Technologies) for 5 days at 37°C, 4% O_2 with

7% CO_2. Further maturation was carried out by culturing immature hepatocytes in hepatocyte culture medium (HCM, Lonza) containing all supplied "singlequots" except for epidermal growth factor from the HCM "bullet" kit and 20 ng/ml oncostatin-M (OSM, Sigma-Aldrich) at 37°C, ambient O_2 with 5% CO_2. The medium for all stages of differentiation was refreshed every day.

After differentiation initiation, cells at each of the four major stages, i.e., definitive endoderm, hepatic endoderm, hepatic progenitor, and further hepatic maturation, expressed stage-specific markers as confirmed by immunofluorescent staining (Figure 4b). Hepatic specification was further confirmed by accessing the expressions of the four key liver-specific genes by real-time polymerase chain reaction (qPCR) analysis (Figure 4c). The expression levels of the hepatic lineage-specification gene hepatocyte nuclear factor 4α (HNF4a), fetal hepatic marker gene α-fetoprotein (AFP), and the more mature liver-specific genes transthyretin (TTR) and albumin (ALB) significantly increased as the differentiated cells matured over the various stages of hepatic differentiation (Figure 4c). In particular, the expression levels of HNF4a, the fetal hepatic marker AFP, and TTR after 10 d of differentiation were much higher than those at endodermal stage, suggesting that differentiated cells after day 10 entered hepatic lineages (Figure 4c) (12–14). Following hepatic lineage specification, cells entered hepatic progenitor stage, i.e., became HPCs after 12–14 d of differentiation, which further matured into HLCs after 17–19 d of differentiation (11, 14). Further characterization of HPCs immediately before encapsulation with flow cytometry showed that an average of 91% of cells were positive for both HNF4a and FoxA2, the hepatic specification markers (14), confirming their

45

hepatic progenitor nature and purity (Figure 5). The purity of cells at each differentiation stage was also assessed by flow cytometry as shown in Figure 5.

Before bioprinting, human iPSC-derived HPCs at their differentiation day 12-14 were digested by 0.25% trypsin-EDTA to prepare a cell suspension solution at 40 millions/ml. The solution was then aliquoted into 1.5 mL centrifuge tubes, placed on ice and used within 2 h.

2.2.2 Supporting cell maintenance

Human umbilical vein endothelial cells (HUVECs) and the adipose-derived stem cells (ADSCs) were chosen as the supporting cells representing the endothelial and mesenchymal lineages for their primitive nature and their potentials in forming functional vasculatures as shown and discussed in previous studies (15, 12, 16). ADSCs were used over other sources of mesenchymal stem cells for their easy availability from individuals and promising clinical applications (17). HUVECs and ADSCs were maintained in their respective culture media before encapsulation.

2.2.3 Cancer cell line culture

HepG2 cell line was purchased from ATCC and maintained in DMEM (Thermo Fisher Scientific) with 10% (vol/vol) fetal bovine serum (FBS) (Gibco). Cells were passaged every four days upon $80-90\%$ confluence using 0.25% (vol/vol) Trypsin-EDTA (Thermo Fisher Scientific).

Prior to bioprinting, cells were dissociated using 0.25% (vol/vol) Trypsin-EDTA and counted with a hemacytometer. A cell suspension in growth medium at 2.5 million cells per mL was prepared and 50 µL was aliquoted into each 1.5 mL centrifuge tube. The cell aliquots were placed on ice and used within 2 h.

2.3 Rapid 3D bioprinting

Rapid 3D bioprinting of hexagonal constructs with and without cells was carried out using a digital micromirror device (DMD)-based system. This custom built printing platform consists of a LED light source (Hamamatsu), a DMD chip (DLP Technology of Texas Instruments), aligning optics, and a movable stage controlled by a motion controller (Newport). The digital pattern of the hexagon was designed in Adobe Photoshop and loaded to the DMD chip before bioprinting.

2.3.1 Fabrication of acellular and mono-culture liver construct

For printing an acellular construct, the prepolymer solution was loaded to the space between a methacrylated coverslip fixed on the motion controller stage and a fixed polydimethylsiloxane (PDMS) layer, and then polymerized into a hexagonal construct following light exposure.

For printing a construct with one type of cells encapsulated, the prepolymer solution was mixed with cell suspension into a cell-material mixture. This cell-material mixture was then loaded to the same space between a methacrylated coverslip fixed on the motion controller stage and a fixed PDMS layer, and then polymerized into a hexagonal construct

47

following light exposure (Figure 6a). The height of the construct was controlled by the motion controller and set to be around 200 μm. Bioprinted constructs were then rinsed once in DPBS solution, followed by another rinse in medium and incubation in medium at 37°C and 5% CO2. Medium was replaced the next day following bioprinting and then every other day.

2.3.2 Fabrication of tri-culture platform

The two-step bioprinting process to print a 3D tri-culture model consisted of printing a hepatic cell layer followed by a second complementary layer of supporting cells that fits in the empty space of the first layer (Figure 6b). Immediately before UV exposure, cell suspension was mixed with the pre-polymer solution. For each printing step, 30μl of the mixture was administered manually by a pipette to the space between a methacrylated coverslip fixed on the stage of motion controller and a PDMS layer attached on a glass slide, and then exposed to the UV light ($88mW/cm^2$) with the liver mask loaded to the DMD chip. This first bioprinted layer was washed three times with warm DPBS and aspirated dry. The supporting cell suspension was then mixed with the pre-polymer solution, and administered to the space between the same coverslip and PDMS layer for a second UV exposure with the supporting cell mask loaded to the DMD chip. This bioprinted 3D tri-culture sample was then washed in both DPBS and medium, then incubated at 37°C with 5% CO_2. Culture medium was replaced on the following day and then every other day.

2.3.3 Fabrication of cancer invasion system

Rapid 3D bioprinting of cancer invasion model was carried out using the same DMD-based bioprinting platform as described in the above section. Three hexagons of HepG2 cells, each consisting of cells tracked with a specific fluorescence color to distinguish the matrix stiffness were printed. These steps were followed by a final print of the fibrous septa in between the hexagons (Figure 7). Prior to printing, three digital patterns of the hexagon and one pattern of fibrous septa were designed in Adobe Photoshop and loaded into the DMD chip. One day before printing, three flasks of HepG2 cells were tracked using CellTracker™ green CMFDA dye (5 µM, 1 h incubation), CellTracker™ orange CMTMR dye (5 µM, 1 h incubation), and Qtracker™ 705 cell labeling kit (15 nM, overnight incubation) respectively to label live cells with a specific color. Cells tracked by Qtracker™ 705 dye (imaged as in red pseudo color) were encapsulated in the soft matrix, cells tracked by green CMFDA dye (imaged as in green pseudo color) were encapsulated in the matrix of medium stiffness, cells tracked with orange CMTMR dye (imaged as in yellow pseudo color) were encapsulated in the stiff matrix representative of cirrhotic liver modulus.

On the day of printing, HepG2 cells of each color were digested and made into cell suspension as described in the previous section. The dECM-based prepolymer solution was added to the cell suspension. Next, 20 µl of the cell-material mixture with one tracking color was pipetted into the space between a methacrylated coverslip fixed on the motion controller stage and a fixed PDMS layer and then polymerized into a hexagonal construct following light exposure. The printed construct was rinsed with sterile DPBS, aspirated

49

dry, and the next cell-material mixture was loaded to the same space to print. The rinsing and printing was repeated one more time to print the third cell embedded hexagon. Following the printing of cells tracked with all three colors, collagen I-based prepolymer solution was added to the stage and the fibrous septa-like structure was printed in between the hexagons. The height of the entire construct was controlled by the motion controller and set to be around 200 μm. The bioprinted constructs were then rinsed once in DPBS, followed by another rinse in medium and incubation in medium at 37°C and 5% CO_2. Medium was replaced the next day following bioprinting and then every other day.

2.4 Assays designed for tissue model evaluation

2.4.1 Cell viability and metabolism analysis

Cell viability analysis was performed on day 1, 3 and 7 following bioprinting. Samples were washed with DPBS once following culture medium removal, then were incubated with 2μM calcein AM (live cell stain) and 4μM ethidium homodimer-1 (dead cell stain) solution at room temperature for 30 min. Imaging acquisition by a Leica DMI 6000B microscope (Leica Microsystems) was immediately carried out following incubation and washes. Alive cells, fluorescently labeled by calcein, and dead cells, fluorescently labeled by EthD-1, were counted for the respective samples z-stack in ImageJ.

Cell metabolism was analyzed by using CellTiter-Glo® 3D Viability Assay based on intracellular adenosine triphosphate (ATP) production. Briefly, duplicate samples were placed in a 24-well plate and equal volumes of media and CellTiter-Glo® 3D Reagent was

added. The samples were then shaken at 160 rpm for 1 h at room temperature to ensure effective extraction of ATP from the tissue constructs. Next, 200 µL of each sample was transferred into a white opaque-walled 96-well plate and the ATP content was calculated based on a ATP standard curve generated using ATP disodium salt according to the manufacturer's protocol. Luminescence was measured with a Tecan Infinite® M200 PRO microplate reader.

2.4.2 Phenotype characterization

The expression of specific intracellular proteins was mainly characterized by immunofluorescence staining and the subsequent imaging. For analysis on population purity in terms of percentage of cells expressing specific markers, fluorescence activated cell sorting (FACS) was performed.

Immunofluorescence Staining

Samples were fixed in 4% paraformaldehyde phosphate buffer solution (PFA, Wako) for 15 min at room temperature and subsequently blocked and permeabilized by 2% bovine serum albumin (BSA, Gemini Bio-Products) solution with 0.1% Triton X-100 (Promega) for 1 hour at room temperature. For human SOX17, FoxA2, HNF4a, AFP or Albumin staining, samples were incubated with mouse monoclonal antibodies against human SOX17 (1:50, R&D), rabbit monoclonal antibodies against human FoxA2/HNF3beta (1:100, Cell Signaling Technology), rabbit monoclonal antibodies against human HNF4a (1:100, Cell Signaling Technology), mouse monoclonal antibodies

against human AFP (1:100, Cell Signaling Technology) or rabbit polyclonal antibodies against human albumin (1:100, Cell Signaling Technology) overnight at 4°C respectively. For human E-cadherin and albumin staining, samples were incubated with mouse monoclonal antibodies against human E-cadherin (1:100, Cell Signaling Technology) and rabbit polyclonal antibodies against human albumin (1:100, Cell Signaling Technology) overnight at 4°C. Samples were washed 3 times with DPBS. Secondary antibody incubation was performed using fluorophore-conjugated anti-IgG antibodies (all at 1:200, Biotium) in 2% BSA solution for 1 hour at room temperature. Hoechst 33342 (1:2000, Life Technologies) nucleus counterstain was also performed with secondary antibody incubation. Fluorescently stained samples were stored in DPBS with 0.05% sodium azide (Alfa Aesar) at 4°C after three times of washing with DPBS.

FACS Analysis

The human iPSC-derivatives from 12 well plates were digested with 0.25% trypsin/EDTA. Digested cells were fixed in 4% PFA for 15 min at room temperature, followed by permeabilization in 1% BSA with 0.1% triton X at room temperature for 30 min. For human SOX17, FoxA2, HNF4a, AFP or Albumin staining, cells were incubated with mouse monoclonal antibodies against human SOX17 (1:50), rabbit monoclonal antibodies against human FoxA2/HNF3beta (1:100), rabbit monoclonal antibodies against human HNF4-a (1:100), mouse monoclonal antibodies against human AFP (1:100) or rabbit polyclonal antibodies against human albumin (1:100) overnight on a shaker at 4°C respectively. Secondary antibody incubation was performed using fluorophore-conjugated

anti-IgG antibodies (all at 1:200) in 1% BSA solution with 0.1% triton X for 45 min at room temperature. Stained cells were re-suspended in 500μl of 1% BSA solution with 0.05% azide and stored at 4°C before analysis. FACS was carried out using LSRFortessa cell analyzer (BD). Unstained control and secondary-only control were included in each experiment for threshold setting. FACS profiles were produced by using FlowJo software.

Quantification of spheroid size

ImageJ was used to generate z-projection image and render 3D reconstructions from the confocal z-stacks of hepatic spheroids within the bioprinted model. For spheroid size quantification, the diameters of spheroids in the direction of 0, 45, 90, and 135 degrees in the z-projection images were measured by ImageJ and averaged for comparison. 3D reconstruction of the stack from the same sample was used during measurement to ensure correct identification of individual spheroid. Three samples (n = 3) were used for each condition.

2.4.3 Evaluation of gene expression

Gene expression was evaluated by performing real-time polymerase chain reaction (qPCR). Cells that cultured as monolayer in plates were treated with ice-cold TRIzol reagent (Life Technologies) for 5 min then stored in -80°C fridge before RNA extraction. Bioprinted samples were treated with ice cold Trizol and pipetted for 5 min before storage in -80°C fridge. Total RNA from each Trizol sample was isolated using Direct-zol RNA MiniPrep Kit (Zymo Research). Extracted RNA samples were stored in -80°C fridge before

PCR experiments. During PCR experiments, cDNA was obtained by reverse transcription using M-MLV reverse transcriptase (Life Technologies) and oligo(dT)18 primer (Thermo Scientific). qPCR was performed using iQ SYBR Green Super mix (Bio-Rad) with specific primers (Valugene) and detected by Bio-Rad CFX Connect Real-Time PCR System (Bio-Rad). Relative quantification was performed based on the threshold cycle (Ct) of each sample, and the values were normalized against the input determined for the housekeeping gene, glyceraldehyde 3-phosphate dehydrogenase (GAPDH).

2.4.4 Evaluation of liver-specific functions

Anabolic liver function, in particular the secretion of albumin, and catabolic function, in particular the breakdown of amino acid into urea, were explored. Secreted albumin in the supernatant was measured by enzyme-linked immunosorbent assay (ELISA) and urea in the supernatant was measured by urea assay kit.

ELISA

The culture supernatants were collected from samples at various time points and stored in -80°C fridges before analysis. ELISA was performed according to the manufacturer's instructions by using albumin human ELISA kit (Abcam). The amount of albumin secretion was calculated according to the standard curve from each experiment, followed by normalization to the theoretical input cell number and time period.

Urea Secretion Quantification

The culture supernatants were collected from samples at various time points and stored in -80°C fridges before analysis. Urea production quantification was performed using QuantiChrom urea assay kit (BioAssay Systems) according to the manufacturer's instructions. The amount of urea secretion was calculated based on the standard curve from each experiment followed by normalization to the theoretical input cell number and time period.

2.4.5 Evaluation of drug metabolizing potential

Drug metabolism potential, in particular the upregulation of cytochrome P450 (CYP) genes was studied upon the addition of a known inducer as compared to the control conditions.

To assess CYP induction potential, the gene expression levels of CYPs in inducer (rifampicin)-treated and untreated samples were measured by real-time qPCR as described above. The cells were treated with rifampicin (25 μM, Sigma-Aldrich) for three days and assessed on day 7 following bioprinting; Non-treated samples were used as controls for comparison. Medium with inducer compounds were replaced daily. Relative quantification was performed against a standard curve and the values were normalized against the input determined for the housekeeping gene, glyceraldehyde 3-phosphate dehydrogenase (GAPDH).

2.4.6 Quantification of cancer cell outgrowth

Fluorescence images of HepG2 cells tracked in each color (representing each

matrix stiffness) on day 1, 3 and 7 were taken by Leica microscope as described in the above section. During the analysis of each sample, a hexagonal outline was drawn using the polygon selection tool in ImageJ on the bright field image to select out one hexagon. This hexagonal outline was then restored in the corresponding fluorescence channel and used to clear out all fluorescence signals within the hexagon. The total area of the outgrown cells in this tracked color was then measured using the particle analysis tool in ImageJ. These steps were repeated for each fluorescence channel to quantify the total outgrowth area of cells from each of the three hexagons. Five individual samples were used for each condition per time point.

2.4.7 Statistical analysis

Sample populations were compared using t-test or one-way Analysis of variance (ANOVA) performed with GraphPad Prism (GraphPad Software). P value smaller than 0.05 was used as the threshold for statistical significance. Data points on the graphs represent mean values with error bars representing standard error of the mean (SEM).

2.5 Acknowledgments

Chapter 2, in part, is a reprint of the published article, "Deterministically patterned biomimetic human iPSC-derived hepatic model via rapid 3D bioprinting." Ma X, Qu X, Zhu W, Li Y, Yuan S, Zhang H, Liu J, Wang P, Lai CSE., Zanella F, Feng G-S, Sheikh F, Chien S, Chen SC. Proceedings of the National Academy of Sciences, 2016. This chapter, in part, has also been submitted for publication of the material as it may appear in the Journal of Biomaterials, 2018, Ma X, Yu C, Wang P, Xu W, Wan X, Lai CSE, Liu J, Koroleva-maharajh A, Chen SC. The dissertation author was the primary investigator and author of these papers.
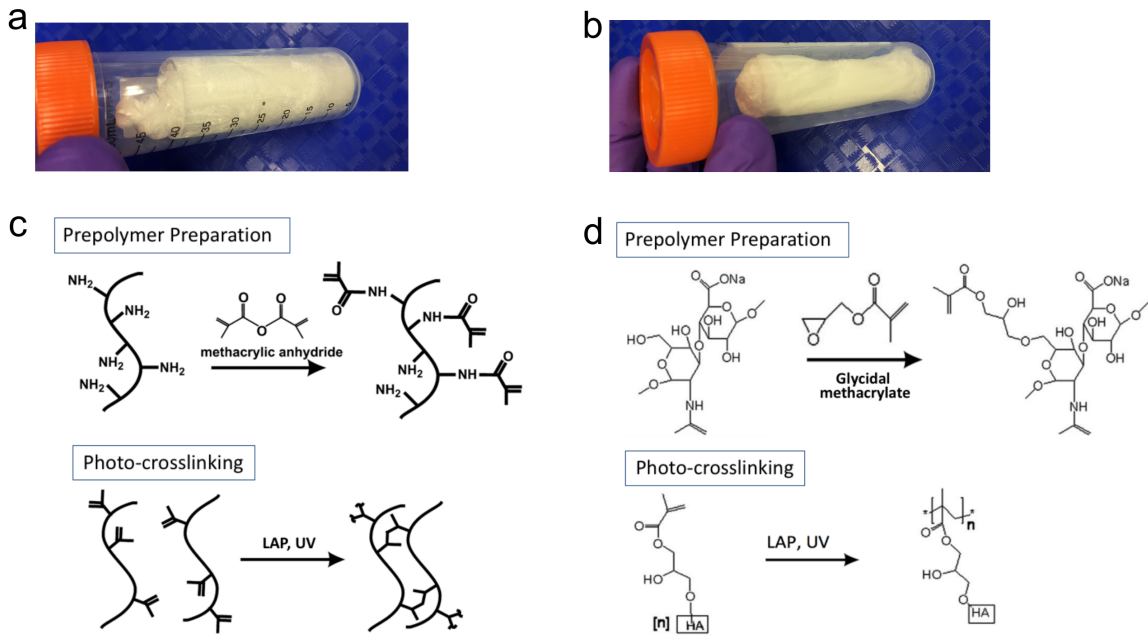
Figure 2-1. Synthesized biomaterials and reaction mechanism. (a) Image of freeze-dried GelMA foam in a 50mL conical tube. (b) Image of freeze-dried GMHA foam in a 50mL conical tube. (c) Prepolymer preparation and photo-crosslinking reactions for GelMA. (d) Prepolymer preparation and photo-crosslinking reactions for GMHA.
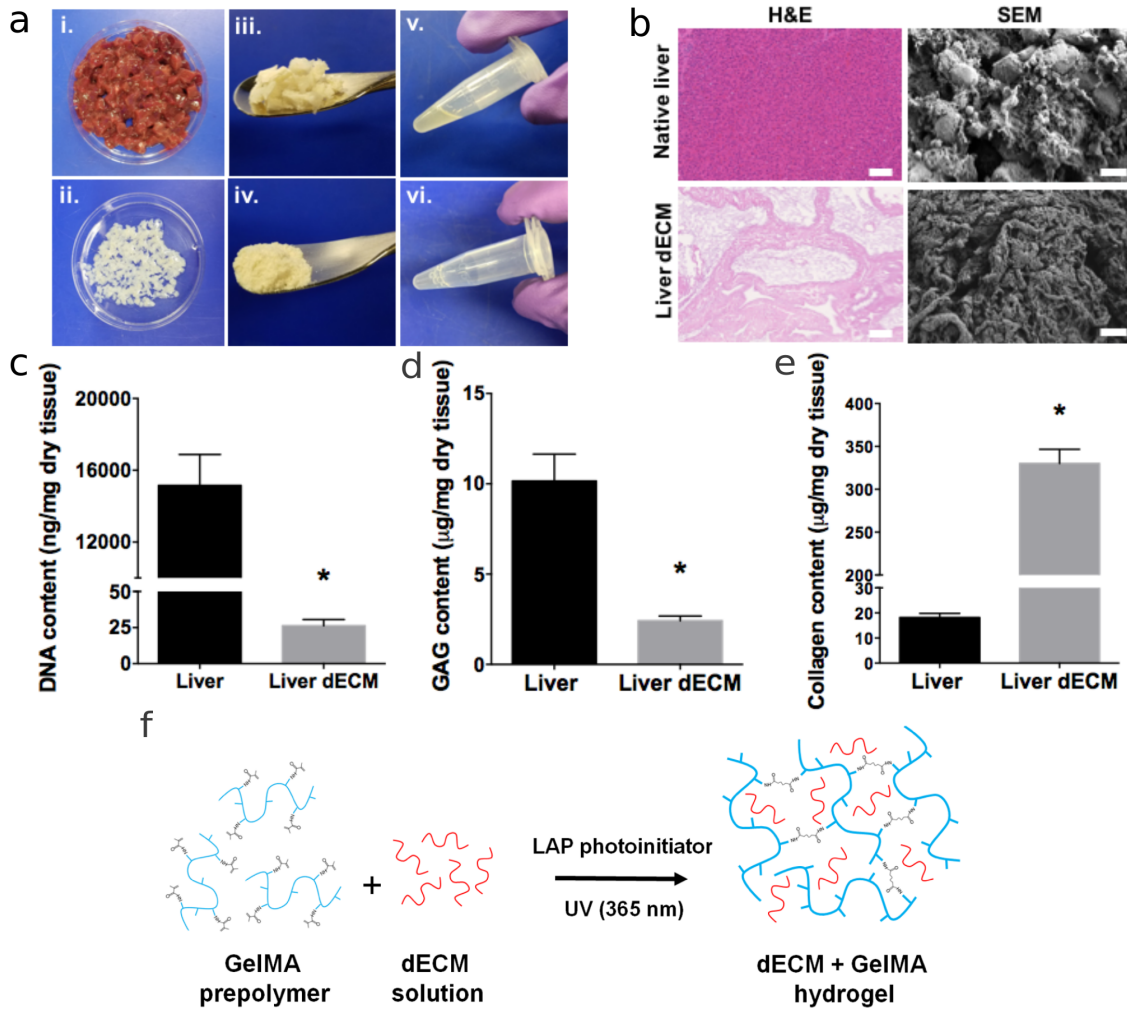
Figure 2-2. Liver dECM preparation and characterization. (a) Decellularization of porcine liver and processing into a printable solution: i) fresh liver tissue, ii) liver dECM, iii) lyophilized liver dECM, iv) cryomilled liver dECM, v) pepsin solubilized liver dECM, vi) liver dECM-GelMA prepolymer solution. (b) Representative H&E stains and SEM images of the native liver and liver dECM showing full decellularization via removal of cells (scale bar = 100 μm) and preservation of intact collagen fibrils and ultrastructure (scale bar = 10 μm). (c) Quantification of DNA content of liver dECM and native liver. (d) Quantitative measurement of GAG content of liver dECM and native liver. (e) Quantitative measurement of collagen content of liver dECM and native liver. (f) Schematic diagram showing the photo-crosslinking reaction of dECM-GelMA mixture. All error bars represent SEM, and n = 4 for all data points. $*P \leq 0.05$.
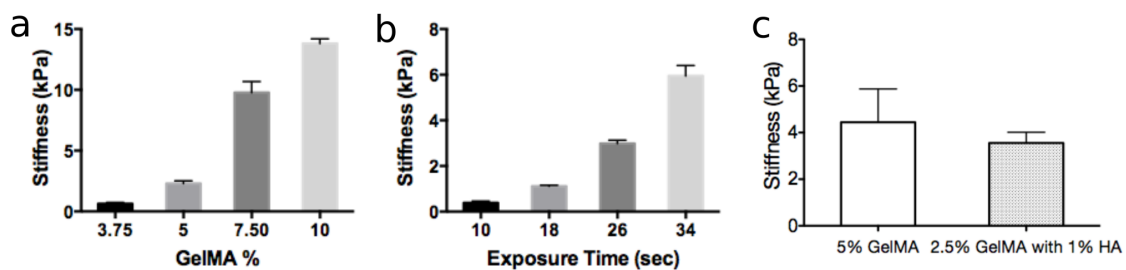
Figure 2-3. Mechanical property of printed scaffolds. (a) Bar chart showing the relationship between scaffold stiffness and GelMA concentration. n = 5. (b) Bar chart showing the relationship between scaffold stiffness and printing exposure time. n = 5 (c) Bar chart showing the scaffold stiffness for 5% GelMA and 2.5% GelMA with 1% HA. n = 3. Error bars represent SEM for all plots, *P ≤ 0.05.
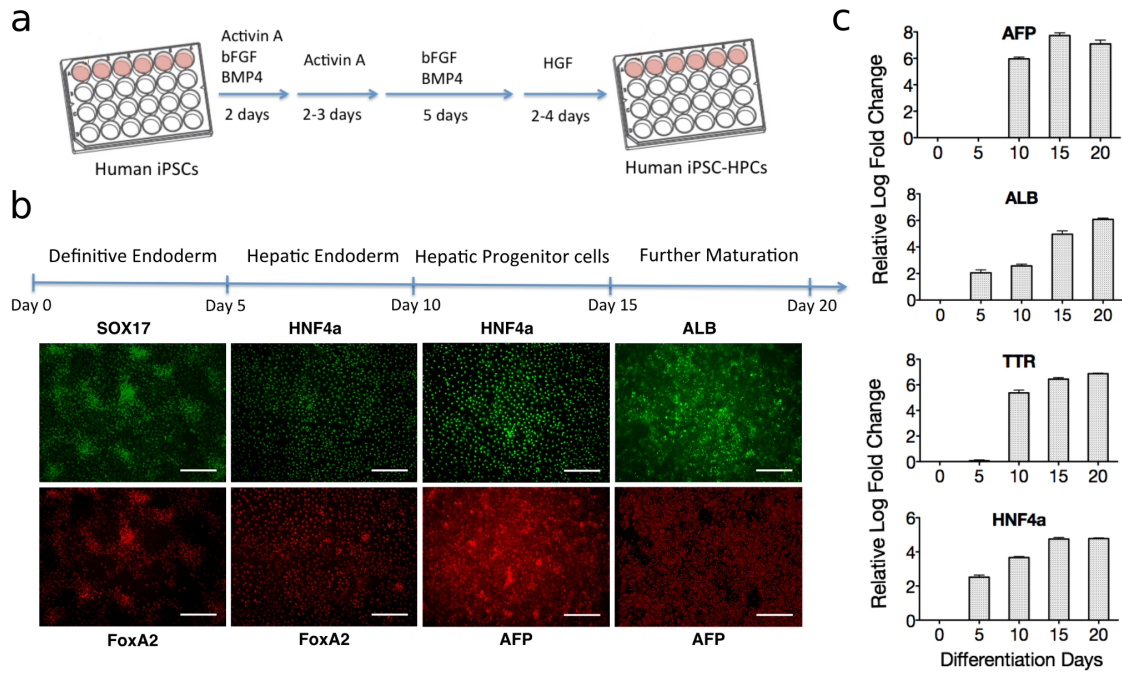
Figure 2-4. Characterizations of iPSC hepatic differentiation. (a) Schematic diagram outlining the differentiation protocol. (b) Four major human iPSC hepatic differentiation stages and the corresponding immunofluorescence images showing staining of the respective stage-specific markers. All scale bars are at 500μm. (c) Gene expression profiles by qPCR showing the expressions of ALB, HNF4a, TTR and AFP of samples at iPSC hepatic differentiation day (DD) 0, 5, 11, 16 and 20. All fold changes are relative to the expression level of human iPSCs. Error bars represent SEM, and n=3 for all data points.
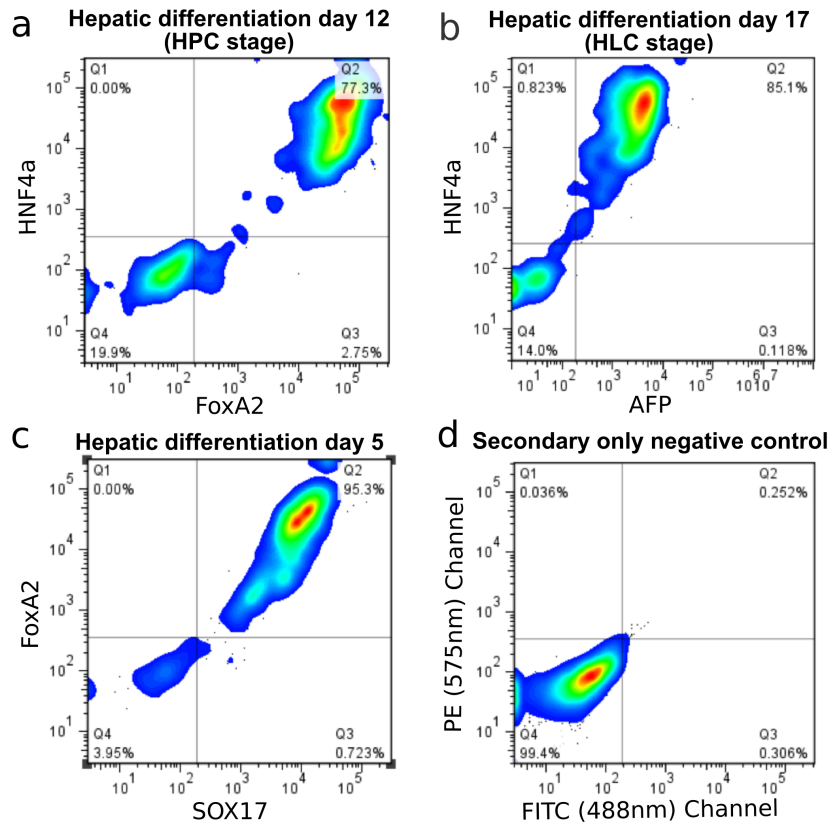
Figure 2-5. Representative flow cytometric profiles of cells. The purity of cell populations on (a) day 12 (HPCs), (b) day 17 (HLCs) and (c) day 5 (endodermal stage) of differentiation was assessed based on their expressions of stage-specific markers by flow cytometry. (d) Population incubated only by secondary antibodies was used as a negative control in the flow cytometry experiments. Q2 on the top right quadrant indicates the population expressing both markers for the stage.
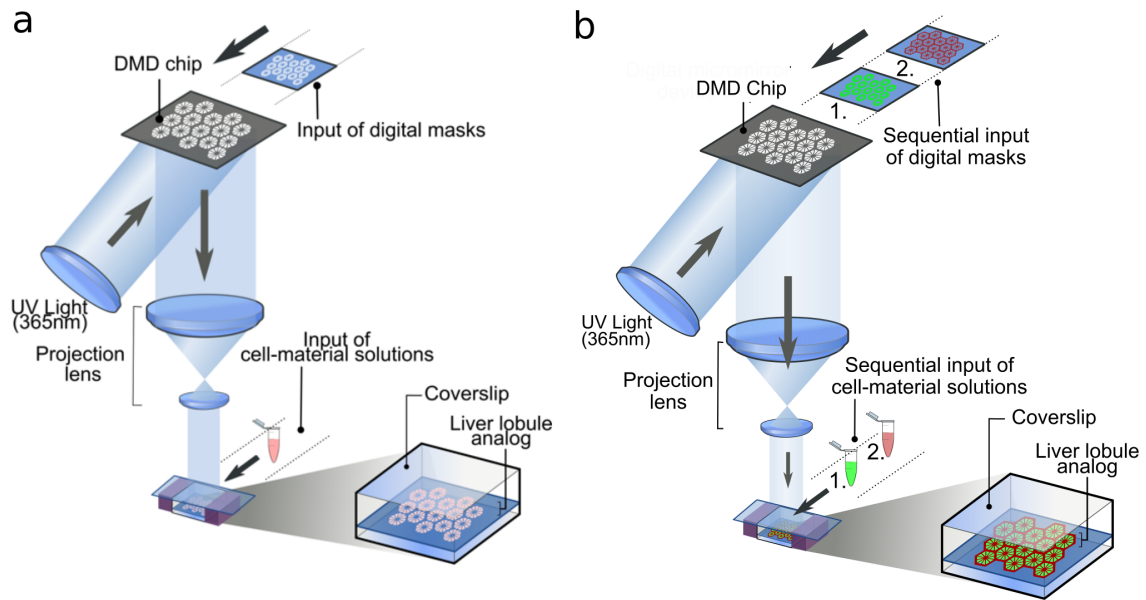
Figure 2-6. Schematic diagrams of 3D bioprinting process. (a) 3D bioprinting of acellular construct or mono-culture liver tissue model. (b) 3D bioprinting of tri-culture liver tissue model.
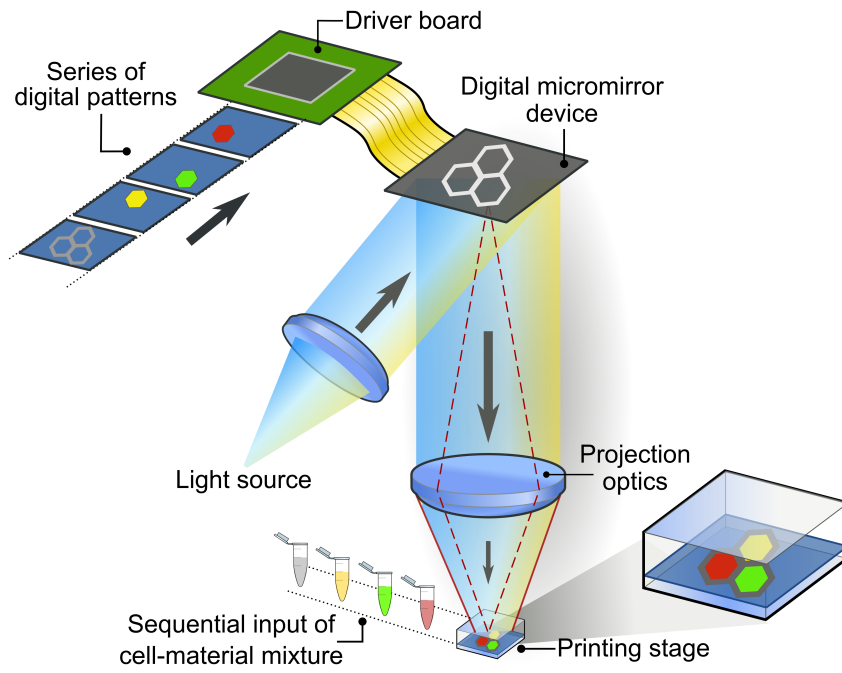
Figure 2-7. Schematic diagram showing 3D bioprinting of liver cancer invasion model.

2.6 References

1.   W. Zhu, X. Ma, M. Gou, D. Mei, K. Zhang, and S. Chen, "3D printing of functional biomaterials for tissue engineering," Curr. Opin. Biotechnol. **40**, 103–112 (2016).

2.   J. B. Leach, K. A. Bivens, C. W. Patrick, and C. E. Schmidt, "Photocrosslinked hyaluronic acid hydrogels: Natural, biodegradable tissue engineering scaffolds," Biotechnol. Bioeng. **82**, 578–589 (2003).

3.   J. W. Nichol, S. T. Koshy, H. Bae, C. M. Hwang, S. Yamanlar, and A. Khademhosseini, "Cell-laden microengineered gelatin methacrylate hydrogels," Biomaterials **31**, 5536–5544 (2010).

4.   R. Gauvin, Y.-C. Chen, J. W. Lee, P. Soman, P. Zorlutuna, J. W. Nichol, H. Bae, S. Chen, and A. Khademhosseini, "Microfabrication of complex porous tissue engineering scaffolds using 3D projection stereolithography," Biomaterials **33**, 3824–3834 (2012).

5.   X. Ma, X. Qu, W. Zhu, Y.-S. Li, S. Yuan, H. Zhang, J. Liu, P. Wang, C. S. E. Lai, F. Zanella, G.-S. Feng, F. Sheikh, S. Chien, and S. Chen, "Deterministically patterned biomimetic human iPSC-derived hepatic model via rapid 3D bioprinting," Proc. Natl. Acad. Sci. **113**, 2206–2211 (2016).

6.   P. M. Crapo, T. W. Gilbert, and S. F. Badylak, "An overview of tissue and whole organ decellularization processes," Biomaterials **32**, 3233–3243 (2011).

7.   B. D. Fairbanks, M. P. Schwartz, C. N. Bowman, and K. S. Anseth, "Photoinitiated polymerization of PEG-diacrylate with lithium phenyl-2,4,6-trimethylbenzoylphosphinate: polymerization rate and cytocompatibility.," Biomaterials **30**, 6702–6707 (2009).

8.   X. Qu, W. Zhu, S. Huang, Y. Li, S. Chien, and K. Zhang, "Relative impact of uniaxial alignment vs form-induced stress on differentiation of human adipose derived stem cells," Biomaterials **34**, 9812–9818 (2013).

9.   O. Rouvie, M. A. Dresner, P. J. Rossman, L. J. Burgart, J. L. Fidler, and R. L. Ehman, "MR elastography of the liver : preliminary results," Radiology **240**, 440–448 (2006).

10.   J. You, S. Park, D. Shin, D. Patel, V. K. Raghunathan, M. Kim, C. J. Murphy, G. Tae, and A. Revzin, "Characterizing the effects of heparin gel stiffness on function of primary hepatocytes," Tissue Eng. Part A **19**, 2655–2663 (2013).

11.   S. K. Mallanna and S. a Duncan, "Differentiation of hepatocytes from pluripotent

stem cells," Curr. Protoc. Stem Cell Biol. **26**, Unit 1G.4. (2013).

12. T. Takebe, R.-R. Zhang, H. Koike, M. Kimura, E. Yoshizawa, M. Enomura, N. Koike, K. Sekine, and H. Taniguchi, "Generation of a vascularized and functional human liver from an iPSC-derived organ bud transplant," Nat. Protoc. **9**, 396–409 (2014).

13. K. Si-Tayeb, F. P. Lemaigre, and S. A. Duncan, "Organogenesis and development of the liver," Dev. Cell **18**, 175–189 (2010).

14. A. DeLaForest, M. Nagaoka, K. Si-Tayeb, F. K. Noto, G. Konopka, M. A. Battle, and S. A. Duncan, "HNF4A is essential for specification of hepatic progenitors from human pluripotent stem cells," Development **138**, 4143–4153 (2011).

15. T. Takebe, K. Sekine, M. Enomura, H. Koike, M. Kimura, T. Ogaeri, R.-R. Zhang, Y. Ueno, Y.-W. Zheng, N. Koike, S. Aoyama, Y. Adachi, and H. Taniguchi, "Vascularized and functional human liver from an iPSC-derived organ bud transplant," Nature **499**, 481–484 (2013).

16. J. D. Baranski, R. R. Chaturvedi, K. R. Stevens, J. Eyckmans, B. Carvalho, and C. C. S. Solorzano R D, Yang M T, Miller J S, Bhatia S N, "Geometric control of vascular networks to enhance engineered tissue integration and function," Proc. Natl. Acad. Sci. U. S. A. **110**, 7586–7591 (2013).

17. W. Tsuji, J. P. Rubin, and K. G. Marra, "Adipose-derived stem cells: Implications in tissue regeneration," World J. Stem Cells **6**, 312–321 (2014).

Chapter 3 Results: Establishment of a 3D biomimetic liver model in healthy condition with drug metabolizing capability

3.1 Introduction

The liver plays a critical role in the synthesis of important proteins and the metabolism of xenobiotic; the failure of these functions is closely related to disease development and drug-induced toxicity (1). For these reasons, *in vitro* liver models have been extensively developed to serve as platforms for pathophysiological studies and as alternatives to animal models in drug screening and hepatotoxicity prediction (2–4). Human primary hepatocytes, considered as one of the most mature liver cell sources, lose many liver-specific functions rapidly when cultured *in vitro* due to the great discrepancies between the native and culture environments (5, 6). In addition, the practical difficulties in obtaining liver biopsy samples from every patient further hinder their use in personalized liver models. Consequently, hepatocytes derived from human iPSCs, with the potential to be patient-specific and easily accessible, have been widely acknowledged as the most promising cell source for developing personalized human hepatic models (7, 8).

Many groups have reported monolayer differentiation of the human iPSCs into HLCs and their ability to metabolize drugs (7, 9, 10). Nevertheless, human iPSC-derived HLCs are still considered immature in terms of many liver-specific gene expressions, functions and CYP enzyme activities (7, 10). Major liver functions are tightly linked to the 3D assembly of hepatocytes with the supporting cell types from both endodermal and mesodermal origins in a hexagonal lobule unit. Current approaches to use HLCs for *in vitro*

liver model, however, are mostly limited to 2D culture or simple 3D spheroid cultures (4, 7, 11–15). The lack of a biomimetic microenvironment provided from the 3D interactions of parenchymal and non-parenchymal cell types along the hepatic differentiation stages may potentially be one of the limiting factors to functional maturation of the HPCs, as well as the functional preservation of HLCs *in vitro* (16, 17).

Over the last decades, micro-technology tools have emerged to forge the advances in tissue engineering (4, 18–21). While a majority of these microfabrication techniques are limited to the generation of simple 2D geometries with selected materials, DLP-based 3D printing provides superior speed and scalability for the fabrication of complex 3D microstructure (22–25). Moreover, this computer-aided, photopolymerization-based technique offers the flexibility to fabricate a great variety of 3D designs and incorporate a wide range of functional elements including live cells, biomolecules, as well as nanoparticles (26–28). Here we present the application of our customized DLP-based 3D bioprinting system to the development of a 3D hydrogel-based tri-culture model that possesses the physiologically relevant cell combination and micro-architecture. The DLP-based 3D bioprinting system allows us to embed iPSC-HPCs and the supporting cells from both endothelial and mesenchymal origins in a 3D microscale hexagonal hydrogel construct, which progressively promotes cell re-organization and re-alignment within the biomimetic architecture. Furthermore, we demonstrate the improvement of liver-specific gene expression, functions and CYP induction in iPSC-HPCs cultured in the 3D tri-culture model as compared to those in conventional 2D monolayer culture and 3D HPC-only models.

To the best of our knowledge, this is the first report of an *in vitro* hepatic model that combinatorially mimic the several *in vivo* features of liver by providing a 3D culture environment for iPSC-derived hepatic cells in tri-culture with supporting cells in a biomimetic liver lobule pattern. The application of DLP-based 3D bioprinting technology in tissue engineering enables the development of a 3D model for both the maturation and the subsequent maintenance of iPSC-derived hepatic cells, and hence can potentially be used for personalized medicine.

3.2 Results and discussion

3.2.1 3D bioprinted tri-culture liver tissue model with a physiologically relevant design

To create a patient-specific hepatic model that mimics the native architecture and cell composition, we encapsulated human iPSC-derived hepatic cells and the endothelial- and mesenchymal-originated supporting cells in complementary patterns that mimic the hepatic lobule structure by photopolymerization of the hydrogel matrices. We first synthesized the biocompatible and photopolymerizable hydrogel solutions and examined the mechanical stiffness of these hydrogel matrices following light-induced polymerization, as described in chapter 2. Two patterns resembling the anatomical structures of hepatocytes and supporting cells were designed (Figure 1a). The pattern dimensions were adjusted so that the bioprinted structures have lobule dimension approximated that of the human liver lobules *in vivo*. The patterns were transferred to both GelMA and GMHA hydrogels by DLP-based 3D bioprinting technology (Figure 1b), which utilized a DMD chip to generate

photomasks based on input digital patterns for photopolymerization of the hydrogel solutions as previously described in chapter 2. To spatially pattern multiple types of cells and hydrogels, the digital masks were applied in a two-step sequential manner to create a first layer of iPSC-derived hepatic cells supported by 5% GelMA followed by a second complementary layer of supporting cells supported by 2.5% GelMA and 1%HA.

By using this approach, we generated a 3D printed model of iPSC-derived hepatic cells and the supporting cells representing the non-parenchymal cells from endothelial and mesenchymal origins in liver Figure 1c. The model, measured 3 x 3 mm with a thickness of approximately 200 microns, consisted of an array of liver lobule-structure with the physiological dimensions. Thus, this DLP-based 2-step bioprinting approach provided an efficient and flexible way to create a 3D *in vitro* hepatic model that represents the *in vivo* hepatic structure.

The application of rapid 3D bioprinting process to our study allows the flexible use of digital masks (23, 26, 27), and thus facilitates the process of liver lobule pattern design and modification. Moreover, the projection optics of the system focuses light patterns at micron-level resolution, thus enabling the biofabrication of the liver lobule hydrogel construct within several seconds with minimal UV illumination. The thickness of the construct, controlled by the motion controller of the system, can be flexibly adjusted based on various design criteria such as diffusion limitation in models where vascularized system is not fully developed or large scale construct in case of fully vascularized models. As such, the rapid and highly flexible bioprinting system is an excellent tool for building 3D tissue constructs with physiologically relevant dimensions. The two complementary hexagonal

patterns not only mimic the *in vivo* micro-architecture, but also enable both direct contacts at the pattern interface and possible local paracrine interactions between hepatic cells and supporting cells within the hexagons. The *in vitro* liver construct has its lobule diameter within the range of the healthy human liver lobule dimension. In addition to mimicking the native dimension, we also controlled the compressive moduli of the hydrogel matrices for both hepatic cells and supporting cells, since the matrix stiffness has been shown to strongly affect the functions of hepatocytes (29). We carefully adjusted the light exposure time and the percentage of photocrosslinkable materials, the two critical factors in controlling the degree of crosslinking and thus the stiffness of the materials, so that the average compressive moduli of the hydrogel matrices mimicked that of the reported liver tissue (29).

3.2.2 Comparison of differentiated hepatic cells used for 3D hydrogel encapsulation

Human iPSCs generated from fibroblasts were induced to differentiate into hepatic lineage by a four-stage differentiation protocol, i.e. definitive endoderm, hepatic endoderm, hepatic progenitor and further hepatic maturation, as described in chapter 2 (9). Following hepatic lineage specification, cells entered hepatic progenitor stage i.e. became HPCs after 12-14 days of differentiation, which further matured into HLCs after 17-19 days of differentiation (9, 30). Cells at both hepatic progenitor and maturation stages, i.e. HPCs and HLCs, respectively, have demonstrated their potentials in organizing into vascularized liver buds (12, 14), and in the construction of *in vitro* models with simple geometry (11, 13, 15). In order to determine the stage of cells along the differentiation

pathway that is more suitable for hydrogel encapsulation, HPCs and the relatively more mature HLCs were compared in terms of their albumin secretion time course following encapsulation in GelMA (Figure 2). Although neither cell type in 3D hydrogel culture was able to maintain the peak albumin secretion level, the encapsulated HPCs showed a more sustained secretion with a higher quantity (Figure 2). These findings suggest that HPCs may serve as a better candidate for *in vitro* liver model after several days of *in vitro* maturation.

The use of hepatic cells from proper stages is very important to the success of an *in vitro* liver model. The hepatic differentiation protocol used in our study is similar to that in many reports (7, 10). Our results of characterization of each differentiation stage by both immunofluorescent staining of key markers and expression levels of important genes are within the ranges of those observed in literature (7, 10), suggesting that the differentiation process has been successful. The characterizations of the cells along differentiation stages and before encapsulation by staining and flow cytometry are important in controlling the quality and purity of iPSC-HPCs for the bioprinting process and thus the functional performance of the model. Moreover, future study on mesenchymal to epithelial transition process, which is omitted by many current hepatic differentiation protocols (7, 9, 13, 14), can be carried out to understand in depth the differentiation from HPCs to more mature hepatic epithelia. When assessing the albumin production levels of iPSC-HPCs and HLCs following GelMA encapsulation, the higher magnitude and more sustained level of albumin produced following the peak by HPCs supported their potential to be better candidates for the 3D hydrogel encapsulation. This may be due to that HLCs in the later

stage of differentiation process have a more mature status than HPCs, are more metabolic active as in adult hepatocytes, and hence may not adapt to the encapsulated environment. Moreover, the fact that HPCs are maintained under hypoxia differentiation, whereas HLCs are cultured in nomoxia conditions, would facilitate the transition of the former into hydrogel encapsulation. In addition to characterizing key liver markers and metabolic product secretion, which we focused in this study, potential cholangiocytes derived from the bi-potential iPSC-HPCs may be further characterized in future studies. Such characterizations on biliary system, as well as further characterization of hepatic epithelia are important in verifying a mature and functional liver model with biliary system.

3.2.3 Cell viability following printing

To better understand the activities of cells after bioprinting, cell viability was characterized. The combinational effect of the entire bioprinting process, i.e. from cell suspension preparation to light-induced photopolymerization of cell suspension and material mixture, on cell viability was evaluated by viability assay on samples from day 0 to 7. Live and dead cells as characterized by calcein and ethidium homodimer-1, respectively, were quantified (Figure. 3). There were on average 76% viable cells when measured within 2 hours following bioprinting. No significant change was observed within the first three days, whereas after around a week live cells accounted for 65% of the total population, suggesting that the majority of cells were still viable. Characterization of cell viability of iPSC-HPCs showed that an acceptable number of cells remained viable following the whole process of bioprinting and also during the subsequent culture.

3.2.4 3D printed pattern maintenance over time

We next observed the pattern maintenance and potential cell migrations within their patterns using fluorescently labeled iPSC-HPCs (green) and supporting cells (red). Within the first day after bioprinting, cells appeared as individual spheroids patterned in their respective structures from the optical mask (Figure 4). In about three to seven days, the red fluorescently labeled HUVECs and ADSCs aligned along the hydrogel pattern of the matrix, demonstrating the sinusoid-like structures within liver lobule (Figure 5a). When observed under bright field, the patterns gradually became blurred over time, but were well distinguishable when observed under fluorescent channels, suggesting that the whole structure became an integrated construct without losing the intrinsic patterns designed for different cell types (Figure 4). Both iPSC-HPCs and supporting cells were able to stay in their designated patterns for at least ten days. The construct, although appearing as a slab under brightfield, not only maintained the intrinsic hexagonal structures but also showed cell reorganization within them over time.

3.2.5. Cellular realignment and reorganization over time

Over the course of one week, iPSC-HPCs formed aggregates with each other (Figure 5b). Hepatocytes in aggregate or spheroid culture have been shown to be able to maintain viability and metabolic functions for a longer period of time than those in monolayer cultures, possibly due to the better retainment of *in vivo* hepatic morphological characteristics (31–34). To further study the iPSC-HPC aggregates, immunofluorescent stainings were performed on E-cadherin, an epithelial marker that had been shown to

74

protect primary hepatocyte from apoptosis (35), and intracellular albumin, a functional hepatic marker. Aggregates after seven days of culture were stained positively for both E-cadherin and albumin, demonstrating functional spheroid formation (Figure 5b). In addition, the average aggregate sizes of iPSC-HPCs in 3D tri-culture model and iPSC-HPC-only model were characterized and compared (Fig. 3*D*). The 3D tri-culture condition showed greater spheroid formation than the iPSC-HPC-only condition by an average of around 10%. The larger spheroid size suggests a greater extent of cell junctions and potentially better hepatic functional performance (Figure 5c) (32). Together, these results suggest that both iPSC-HPCs and the supporting cells were able to re-organize in their designated pattern of the 3D tri-culture model over time, and that the extent of cell-cell interactions of iPSC-HPCs in 3D tri-culture model, as characterized by average spheroid size, was more than that in 3D HPC-only model.

The staining of E-cadherin and albumin expression over time demonstrated a cell–cell interaction and gradual maturation of HPCs. In line with aggregate formation, the realignment of supporting cells along the hydrogel lines can potentially facilitate channel formation and possible vascularization (36). The greater HPC aggregate size observed in this 3D triculture model further supports the beneficial effects from supporting cells as widely reported in 2D coculture models (15, 37).

3.2.6 Liver-specific gene expression and function over time

Although the greater extent of cell re-organization found in the 3D tri-culture model were encouraging, it was also important to explore the maturation level based on liver-

specific gene expression and functions. To address this question, we first compared the relative expression levels of the hepatic marker genes in iPSC-HPCs from 3D tri-culture model, iPSC-HPC-only model, and the conventional 2D monolayer culture. The expression levels of the hepatic markers that are highly expressed in mature hepatocytes, i.e., HNF4a, TTR and ALB, were higher in tri-culture condition as compared to the other two (Figure 6a). The expression levels of fetal hepatic marker AFP were not significantly different among the three conditions, but a trend of reduced expression level was observed in both the 3D HPC-only and 3D tri-culture model (Figure 6a). Together, these findings showed a relatively more mature gene expression profile of iPSC-HPCs in the 3D tri-culture model.

Next, we compared the anabolic and catabolic functional aspects of the iPSC-HPCs in different models. The levels of albumin secretion by iPSC-HPCs in different models over the period of 19 days were compared (Figure 6b). Albumin secretion declined in all three models following their respective peak, but iPSC-HPCs in tri-culture model were able to maintain the highest level of secretion among the three conditions 5 days after bioprinting (Figure 6b). Similarly, urea production levels from breaking down of amino acids were compared over time (Figure 6c). The iPSC-HPCs in tri-culture condition were shown to maintain the urea production level to a greater extent than the other two conditions.

In line with many structural changes observed previously, there are also functional advancements in HPCs cultured in the 3D tri-culture model. The increased expression of TTR in iPSC-HPCs in 3D tri-culture correlated with that of HNF4a, which controls the

expressions of both TTR and other hepatocyte nuclear factors that regulate the expression of several hepatic genes (30). The improved ALB expression also agrees with the increased albumin secretion from HPCs cultured in 3D tri-culture model 7 d following bio- printing. Despite the eventual decline in albumin and urea production, the relatively higher secretion level over time suggests that iPSC-HPCs in 3D tri-culture model attained a more mature stage than those in merely 3D encapsulation or 2D monolayer culture.

3.2.7 CYP enzyme induction

Encouraged by the observed functional enhancement, we proceeded to investigate the expression levels of key enzymes in liver drug metabolism, i.e., CYPs in iPSC-HPCs from the three experimental conditions. Specifically, we evaluated quantitatively the expression of the five key CYPs, CYP1A2, CYP2B6, CYP2C9, CYP2C19, and CYP3A4, which account for 60% of human drug oxidation (38). Among the five CYPs, the iPSC-HPCs in 3D tri-culture model showed a significantly higher expression of CYP3A4, which is the most common CYP enzyme and estimated to be involved in the metabolism of approximately half the currently used drugs (Figure 7) (39). Although not significant, iPSC-HPCs in 3D triculture model demonstrated the highest average expression levels of CYP1A2, CYP2B6, CYP2C9, and CYP2C19 (Figure 7).

In addition to the evaluation on the baseline CYP expression levels without any drug treatment, the inductions of mRNA transcripts of the five CYPs in iPSC-HPCs were further evaluated by treating samples with an inducer, rifampicin, which is a bactericidal antibiotic drug with potential risk of hepatotoxicity. The induction by rifampicin led to

significant increases in CYP3A4, CYP2C9 and CYP2C19 expression levels in iPSC-HPCs from 3D tri-culture model culture when compared with untreated controls (Figure 7). Such significantly increased CYP expressions from rifampicin treatment were not observed in iPSC-HPCs from either 2D monolayer culture or 3D-HPC-only model, though a trend of improved expression was also observed. The rifampicin treatment did not cause significant changes in CYP1A2 expression level of iPSC-HPCs from any of the conditions (Figure 7). This observation was expected as rifampicin was less likely to induce CYP1A2 as reported (40). However, rifampicin incubation also did not affect significantly the expression of CYP2B6 (Figure 7), which was previously reported to be induced by rifampicin in adult hepatocytes (41, 37). Taken together, these results showed that 3D tri-culture model provided an environment for iPSC-HPCs that improved not only anabolic and catabolic functions, but also the key CYP expression levels and the drug induction potential.

The significant induction by rifampicin of CYP3A4, CYP2C9, and CYP2C19 expression levels shows that iPSC-HPCs after 7 d in 3D tri-culture are able to respond positively to rifampicin as reported for primary hepatocytes (37), thus potentially improving the metabolism and clearance of the drug. Rifampicin is also an inducer of CYP2B6; therefore, the fact that rifampicin treatment did not lead to induction of CYP2B6 under any of the conditions suggests that iPSC-HPCs at this stage may still be incompetent in terms of their drug metabolism capability. Further characterization on the RNA profiling of additional phase I and II enzymes and comparison with adult liver expression profiles can be carried out in future work to provide an in-depth understanding of the maturation level and the drug metabolizing capability of the model.

3.3 Acknowledgments

Chapter 3 is a reprint of the published article, "Deterministically patterned biomimetic human iPSC-derived hepatic model via rapid 3D bioprinting." Ma X, Qu X, Zhu W, Li Y, Yuan S, Zhang H, Liu J, Wang P, Lai CSE., Zanella F, Feng G-S, Sheikh F, Chien S, Chen SC. Proceedings of the National Academy of Sciences, 2016. The dissertation author was the primary investigator and author of this paper.
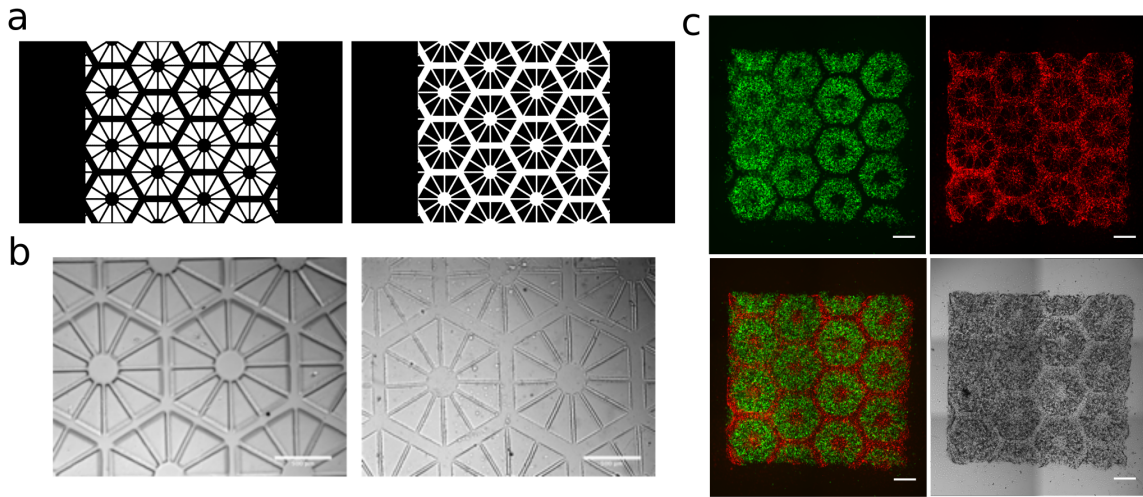
Figure 3-1. 3D bioprinted hepatic construct. (a) Grey scale digital masks corresponding to liver lobule structure (left) and vascular structure (right) designed for 2-step bioprinting. The white patterns represent the light reflecting patterns for photopolymerization. (b) Bright field images showing the patterns of 5% GelMA (left) and 2.5% GelMA with 1% HA (right) scaffolds without cells. Scale bars are at 500μm. (c) Images (5X) taken under fluorescent and bright field channels showing patterns of fluorescently labeled iPSC-HPCs (green) in 5% GelMA and supporting cells (red) in 2.5%GelMA with 1% HA on Day 0. All scale bars are at 500 μm.
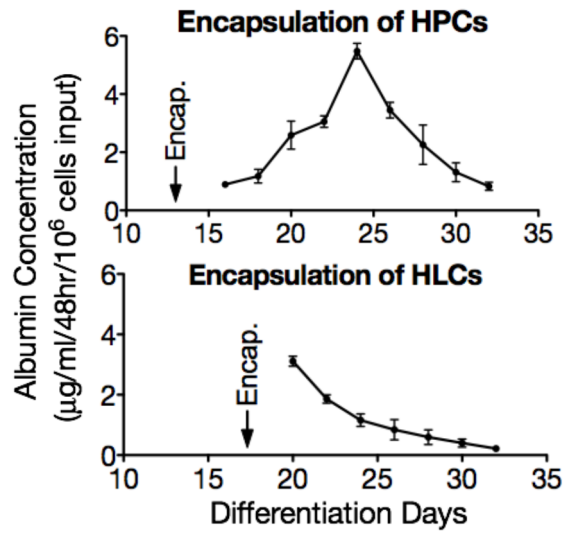
Figure 3-2. Albumin secretion levels of HPCs and HLCs over time following their encapsulation by bioprinting. Albumin measurements were carried out beginning day 3 of encapsulation. Error bars represent SEM, and n=3 for all data points.
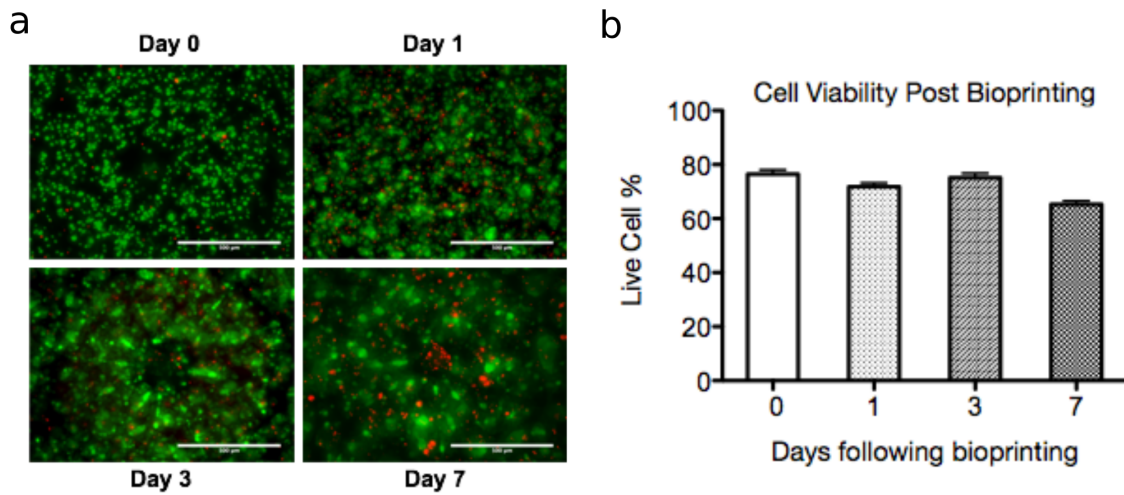
Figure 3-3. Cell viability analysis following bioprinting process. (a) Fluorescent images showing staining of live cells by calcein (green) and dead cells by ethidium homodimer-1 (red) on day 0, 1, 3 and 7 following bioprinting. Scale bars are at 500μm. (b) Bar chart quantified the live cell percentage on day 0, 1, 3 and 7 following bioprinting. Error bars represent SEM, and n=3 for all data points.
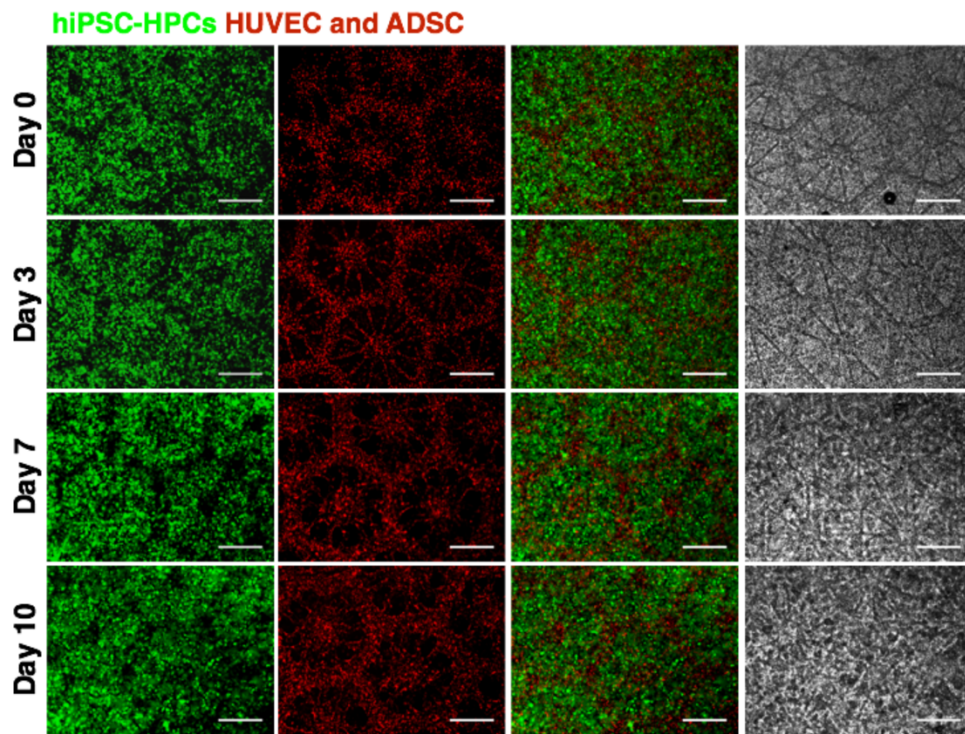
Figure 3-4. Pattern maintenance over time. Fluorescent images (5X) of bioprinted construct consisting of tracked cells on day 1, 3, 7 and 10. All scale bars are at 500 μm.
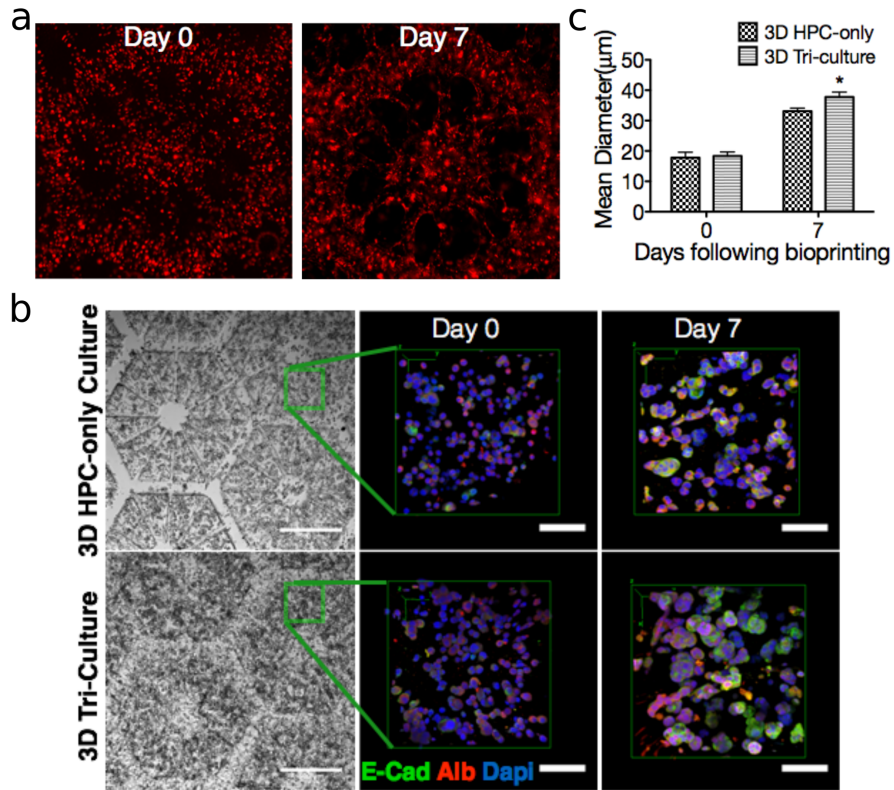
Figure 3-5. Cellular realignment and reorganization over time. (a) Fluorescent images showing supporting cells arrangement on both day 0 and 7 following bioprinting. (b) Grey scale images (5X) and confocal immunofluorescence images (40X) showing albumin (Alb), E-cadherin (E-Cad), nucleus (Dapi) staining of iPSC-HPCs in 3D HPC-only (with no supporting cells) constructs and in 3D tri-culture constructs. Scale bars are at 500μm in bright field and 100μm in fluorescent images respectively. (c) Bar graph showing mean diameters of spheroids within both HPC-only constructs and tri-culture constructs on day 0 and 7. Error bars represent SEM, and n=3 for all data points.
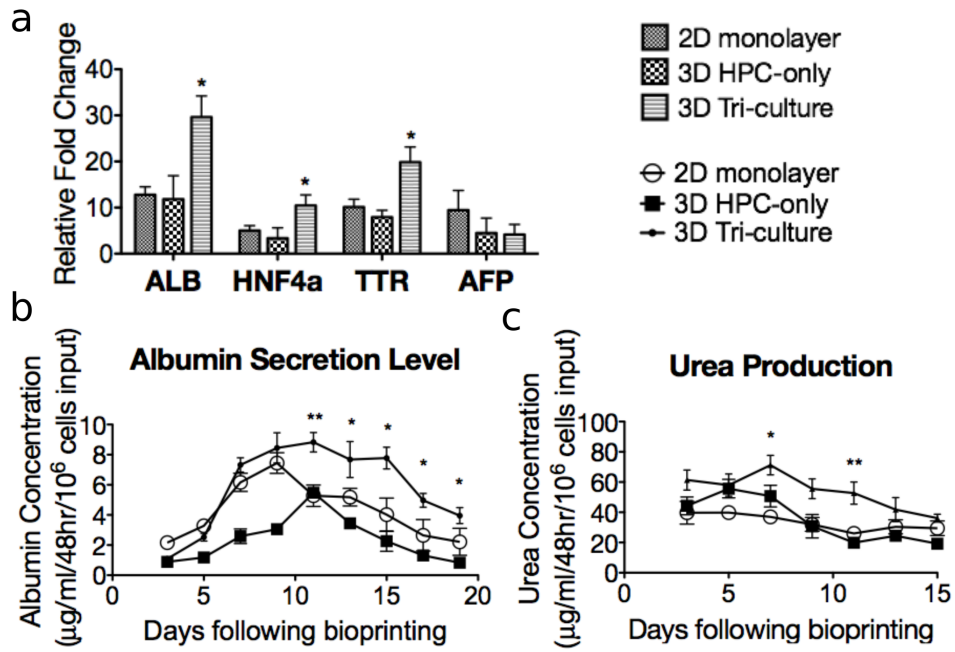
Figure 3-6. Gene expression and functional characterization of the hepatic model. (a) Gene expression profiles comparing the ALB, HNF4a, TTR and AFP expression levels of HPCs in 2D monolayer culture, 3D HPC-only culture model and 3D tri-culture model on day 7 following bioprinting. (b) Albumin secretion levels of HPCs in three different conditions over time. (c) Urea secretion levels of HPCs in three different conditions over time. Error bars represent SEM, and n=3 for all data points.
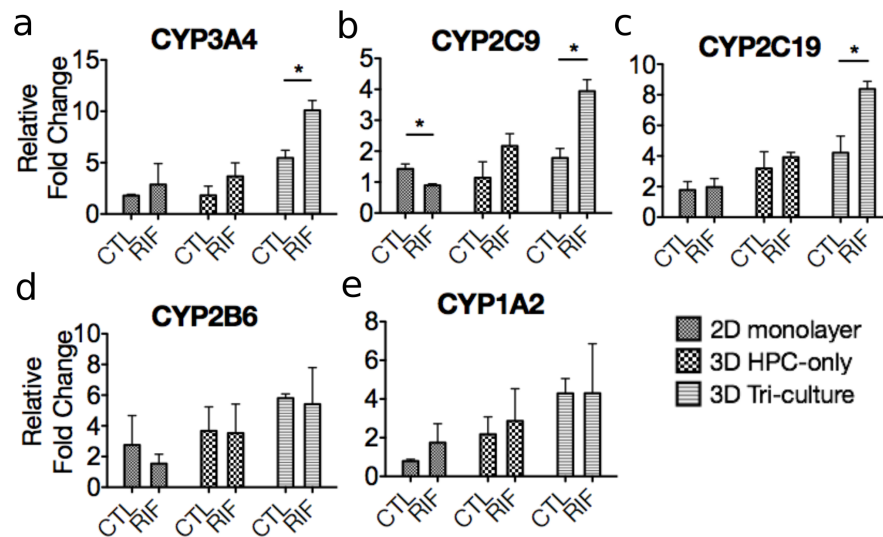
Figure 3-7. CYP enzyme induction. Gene expression profiles showing expression levels of (a) CYP3A4, (b) CYP2C9, (c) CYP2C19, (d) CYP2B6 and (e) CYP1A4 in untreated (CTL) and rifampicin treated (RIF) samples from three conditions on day 7 following bioprinting. All gene expression fold changes are relative to the expressions of iPSC-HPCs on day 12 of differentiation before bioprinting. Error bars represent SEM, and n=3 for all data points.

3.4 References

1.   N. Kaplowitz, "Idiosyncratic drug hepatotoxicity," Nat. Rev. Drug Discov. **4**, 489–499 (2005).

2.   C. Guguen-Guillouzo, A. Corlu, and A. Guillouzo, "Stem cell-derived hepatocytes and their use in toxicology," Toxicology **270**, 3–9 (2010).

3.   L. Choucha Snouber, A. Bunescu, M. Naudot, C. Legallais, C. Brochot, M. E. Dumas, B. Elena-Herrmann, and E. Leclerc, "Metabolomics-on-a-chip of hepatotoxicity induced by anticancer drug flutamide and its active metabolite hydroxyflutamide using HepG2/C3a microfluidic biochips," Toxicol. Sci. **132**, 8–20 (2013).

4.   D. Y. No, K.-H. Lee, I. Seo, and S.-H. Lee, "3D liver models on a microplatform: well-defined culture, engineering of liver tissue and liver-on-a-chip," Lab Chip **15**, 3822–3837 (2015).

5.   L. G. Sivaraman, A Leach, J K Townsend, S Iida, T Hogan, B J Stolz, D B Fry, R Samson, L D Tannenbaum, S R Griffith, "A microscale in vitro physiological model of the liver: predictive screens for drug metabolism and enzyme induction," Curr. Drug Metab. **6**, 569–591 (2005).

6.   N. J. Hewitt, M. J. Gómez Lechón, J. B. Houston, D. Hallifax, H. S. Brown, P. Maurel, J. G. Kenna, L. Gustavsson, C. Lohmann, C. Skonberg, A. Guillouzo, G. Tuschl, A. P. Li, E. LeCluyse, G. M. M. Groothuis, and J. G. Hengstler, "Primary hepatocytes: current understanding of the regulation of metabolic enzymes and transporter proteins, and pharmaceutical practice for the use of hepatocytes in metabolism, enzyme induction, transporter, clearance, and hepatotoxicity studies," Drug Metab. Rev. **39**, 159–234 (2007).

7.   R. E. Schwartz, H. E. Fleming, S. R. Khetani, and S. N. Bhatia, "Pluripotent stem cell-derived hepatocyte-like cells," Biotechnol. Adv. **32**, 504–513 (2014).

8.   S. N. Bhatia, G. H. Underhill, K. S. Zaret, and I. J. Fox, "Cell and tissue engineering for liver disease," Sci. Transl. Med. **6**, 245sr2 (2014).

9.   S. K. Mallanna and S. a Duncan, "Differentiation of hepatocytes from pluripotent stem cells," Curr. Protoc. Stem Cell Biol. **26**, Unit 1G.4. (2013).

10.   Y. Kondo, T. Iwao, K. Nakamura, T. Sasaki, S. Takahashi, N. Kamada, T. Matsubara, F. J. Gonzalez, H. Akutsu, Y. Miyagawa, H. Okita, N. Kiyokawa, M. Toyoda, A. Umezawa, K. Nagata, T. Matsunaga, and S. Ohmori, "An efficient method for differentiation of human induced pluripotent stem cells into hepatocyte-

like cells retaining drug metabolizing activity," Drug Metab. Pharmacokinet. **29**, 237–243 (2014).

11. K. Takayama, K. Kawabata, Y. Nagamoto, K. Kishimoto, K. Tashiro, F. Sakurai, M. Tachibana, K. Kanda, T. Hayakawa, M. K. Furue, and H. Mizuguchi, "3D spheroid culture of hESC/hiPSC-derived hepatocyte-like cells for drug toxicity testing," Biomaterials **34**, 1781–1789 (2013).

12. T. Takebe, K. Sekine, M. Enomura, H. Koike, M. Kimura, T. Ogaeri, R.-R. Zhang, Y. Ueno, Y.-W. Zheng, N. Koike, S. Aoyama, Y. Adachi, and H. Taniguchi, "Vascularized and functional human liver from an iPSC-derived organ bud transplant," Nature **499**, 481–484 (2013).

13. C. Du, K. Narayanan, M. F. Leong, and A. C. A. Wan, "Induced pluripotent stem cell-derived hepatocytes and endothelial cells in multi-component hydrogel fibers for liver tissue engineering," Biomaterials **35**, 6006–6014 (2014).

14. T. Takebe, R.-R. Zhang, H. Koike, M. Kimura, E. Yoshizawa, M. Enomura, N. Koike, K. Sekine, and H. Taniguchi, "Generation of a vascularized and functional human liver from an iPSC-derived organ bud transplant," Nat. Protoc. **9**, 396–409 (2014).

15. D. R. Berger, B. R. Ware, M. D. Davidson, S. R. Allsup, and S. R. Khetani, "Enhancing the functional maturity of induced pluripotent stem cell-derived human hepatocytes by controlled presentation of cell-cell interactions *in vitro*," Hepatology **61**, 1370–1381 (2015).

16. Y. Kim and P. Rajagopalan, "3D hepatic cultures simultaneously maintain primary hepatocyte and liver sinusoidal endothelial cell phenotypes," PLoS One **5**, 1–10 (2010).

17. K. Kim, K. Ohashi, R. Utoh, K. Kano, and T. Okano, "Preserved liver-specific functions of hepatocytes in 3D co-culture with endothelial cell sheets," Biomaterials **33**, 1406–1413 (2012).

18. A. Khademhosseini, R. Langer, J. T. Borenstein, and J. P. Vacanti, "Microscale technologies for tissue engineering and biology," Proc. Natl. Acad. Sci. U. S. A. **103**, 2480–2487 (2006).

19. A. Faulkner-Jones, C. Fyfe, D.-J. Cornelissen, J. Gardner, J. King, A. Courtney, and W. Shu, "Bioprinting of human pluripotent stem cells and their directed differentiation into hepatocyte-like cells for the generation of mini-livers in 3D.," Biofabrication **7**, 44102 (2015).

20. V. L. Tsang, A. a Chen, L. M. Cho, K. D. Jadin, R. L. Sah, S. DeLong, J. L. West, S. N. Bhatia, V. Liu Tsang, A. a Chen, L. M. Cho, K. D. Jadin, R. L. Sah, S. DeLong, J. L. West, and S. N. Bhatia, "Fabrication of 3D hepatic tissues by additive photopatterning of cellular hydrogels.," FASEB J. **21**, 790–801 (2007).

21. J. A. S. Neiman, R. Raman, V. Chan, M. G. Rhoads, M. S. B. Raredon, J. J. Velazquez, R. L. Dyer, R. Bashir, P. T. Hammond, and L. G. Griffith, "Photopatterning of hydrogel scaffolds coupled to filter materials using stereolithography for perfused 3D culture of hepatocytes.," Biotechnol. Bioeng. **112**, 777–787 (2015).

22. A. P. Zhang, X. Qu, P. Soman, K. C. Hribar, J. W. Lee, S. Chen, and S. He, "Rapid fabrication of complex 3D extracellular microenvironments by dynamic optical projection stereolithography," Adv. Mater. **24**, 4266–4270 (2012).

23. K. C. Hribar, P. Soman, J. Warner, P. Chung, and S. Chen, "Light-assisted direct-write of 3D functional biomaterials," Lab Chip **14**, 268–275 (2014).

24. C. Cha, P. Soman, W. Zhu, M. Nikkhah, G. Camci-Unal, S. Chen, and A. Khademhosseini, "Structural reinforcement of cell-laden hydrogels with microfabricated three dimensional scaffolds," Biomater. Sci. **2**, 703–709 (2014).

25. K. C. Hribar, D. Finlay, X. Ma, X. Qu, M. G. Ondeck, P. H. Chung, F. Zanella, A. J. Engler, F. Sheikh, K. Vuori, and S. Chen, "Nonlinear 3D projection printing of concave hydrogel microstructures for long-term multicellular spheroid and embryoid body culture," Lab Chip **15**, 2412–2418 (2015).

26. P. Soman, P. H. Chung, A. P. Zhang, and S. Chen, "Digital microfabrication of user-defined 3D microstructures in cell-laden hydrogels," Biotechnol. Bioeng. **110**, 3038–3047 (2013).

27. M. Gou, X. Qu, W. Zhu, M. Xiang, J. Yang, K. Zhang, Y. Wei, and S. Chen, "Bio-inspired detoxification using 3D-printed hydrogel nanocomposites.," Nat. Commun. **5**, 3774 (2014).

28. W. Zhu, J. Li, Y. J. Leong, I. Rozen, X. Qu, R. Dong, Z. Wu, W. Gao, P. H. Chung, J. Wang, and S. Chen, "3D-printed artificial microfish," Adv. Mater. **27**, 4411–4417 (2015).

29. J. You, S. Park, D. Shin, D. Patel, V. K. Raghunathan, M. Kim, C. J. Murphy, G. Tae, and A. Revzin, "Characterizing the effects of heparin gel stiffness on function of primary hepatocytes," Tissue Eng. Part A **19**, 2655–2663 (2013).

30. A. DeLaForest, M. Nagaoka, K. Si-Tayeb, F. K. Noto, G. Konopka, M. A. Battle,

and S. A. Duncan, "HNF4A is essential for specification of hepatic progenitors from human pluripotent stem cells," Development **138**, 4143–4153 (2011).

31.   J. Z. Tong, S. Sarrazin, D. Cassio, F. Gauthier, and F. Alvarez, "Application of spheroid culture to human hepatocytes and maintenance of their differentiation," Biol. Cell **81**, 77–81 (1994).

32.   R. Glicklis, J. C. Merchuk, and S. Cohen, "Modeling mass transfer in hepatocyte spheroids via cell viability, spheroid size, and hepatocellular functions," Biotechnol. Bioeng. **86**, 672–680 (2004).

33.   T. T. Chang and M. Hughes-Fulford, "Monolayer and spheroid culture of human liver hepatocellular carcinoma cell line cells demonstrate distinct global gene expression patterns and functional phenotypes," Tissue Eng. Part A **15**, 559–567 (2009).

34.   T. T. Chang and M. Hughes-Fulford, "Molecular mechanisms underlying the enhanced functions of three-dimensional hepatocyte aggregates.," Biomaterials **35**, 2162–2171 (2014).

35.   J. L. Luebke-Wheeler, G. Nedredal, L. Yee, B. P. Amiot, and S. L. Nyberg, "E-cadherin protects primary hepatocyte spheroids from cell death by a caspase-independent mechanism," Cell Transplant. **18**, 1281–1287 (2009).

36.   J. D. Baranski, R. R. Chaturvedi, K. R. Stevens, J. Eyckmans, B. Carvalho, R. D. Solorzano, M. T. Yang, J. S. Miller, S. N. Bhatia, and C. S. Chen, "Geometric control of vascular networks to enhance engineered tissue integration and function," Proc. Natl. Acad. Sci. **110**, 7586–7591 (2013).

37.   S. R. Khetani and S. N. Bhatia, "Microscale culture of human liver cells for drug development.," Nat. Biotechnol. **26**, 120–126 (2008).

38.   S. F. Zhou, J. P. Liu, and B. Chowbay, "Polymorphism of human cytochrome P450 enzymes and its clinical impact," Drug Metab. Rev. **41**, 89 (2009).

39.   F. P. Guengerich, "Cytochrome P-450 3A4: regulation and role in drug metabolism," Annu. Rev. Pharmacol. Toxicol. **39**, 1–17 (1999).

40.   J. T. Backman, M. T. Granfors, and P. J. Neuvonen, "Rifampicin is only a weak inducer of CYP1A2-mediated presystemic and systemic metabolism: studies with tizanidine and caffeine," Eur. J. Clin. Pharmacol. **62**, 451–461 (2006).

41.   S. R. Faucette, H. Wang, G. A. Hamilton, S. L. Jolley, D. Gilbert, C. Lindley, B. Yan, M. Negishi, and E. L. LeCluyse, "Regulation of CYP2B6 in primary human

hepatocytes by prototypical inducers.," Drug Metab. Dispos. **32**, 348–358 (2004).

Chapter 4 Results: Development of a liver cancer model with tunable mechanical property for cancer progression study

4.1 Introduction

HCC is ranked as the fifth most common malignant cancer and the second most frequent cause of cancer related mortality worldwide (1). Over 80% of HCCs develop and progress in the form of advanced liver fibrosis or cirrhosis, which is characterized by the development of stiff hepatocellular nodules surrounded by fibrous bands (2, 3). HCC development and progression are strongly affected by the liver ECM stiffness and correlated to stiffness values greater than that of healthy liver parenchyma (4, 5). In addition, the progression of HCC also involves invasion of tumor tissue into the fibrous septa (6). Traditional approaches to study HCC progression involved simply regulating 2D substrate stiffness, which, however, is not representative of the 3D mechanical environment in native liver and therefore could incur results inconsistent with those from 3D approaches (7–11). Current studies examining the liver mechanical properties with 3D matrix models, however, do not reflect the clinically reported stiffness range and the microarchitecture of cirrhotic liver and thus provide less insightful results in understanding HCC progression under diseased conditions (9, 12). In addition to the importance of a relevant 3D mechanical environment, the biomaterial used to study cancer progression has also been shown to play an important role in regulating cancer growth and proliferation (13). Current hydrogel matrices used to modulate stiffness, including alginate and gelatin (9, 12), lack the biochemical cues inherent in the native liver ECM. Therefore, a

biomimetic platform combining liver ECM as a tissue-specific biomaterial and a 3D mechanical environment with tissue-scale organization relevant to diseased liver is critical in studying the biomechanical contributions of the cirrhotic environment on HCC growth and invasion.

Native liver ECM is composed of a wide range of proteins, collagens, glycosaminoglycans, and growth factors that could provide a complex microenvironment to better support liver cell viability and functionality compared to simple protein matrices used in current 2D or 3D cell culture systems (14–16). More importantly, it has been widely established that liver dECM supports liver progenitor differentiation as well as hepatocyte and HCC cell line culture, and is regarded as a promising naturally-derived biomaterial for *in vitro* liver cell culture (17–19). To date, the use of liver dECM in *in vitro* cell culture is largely limited to 2D coatings or 3D gels in simple geometries (19–21), which lack a biomimetic design that mimics HCC nodule surrounded by fibrous bands. In addition, the lack of methods tuning the mechanical property of dECM materials restrain their application to pathological conditions where tissue architecture and mechanical properties are both important in affecting disease progression. DLP-based 3D bioprinting, with the capability to pattern a wide range of functional elements including live cells, biomolecules, and nanoparticles provides superior speed for the fabrication of complex 3D geometries and precise control over material properties (22–24). Here we present a DLP-based rapid 3D bioprinting approach to fabricate cellularized liver dECM-based scaffolds with tunable mechanical properties to serve as a platform for studying the effects of pathologically relevant 3D matrix stiffness on HCC progression and invasion. Furthermore, we

93

demonstrated a novel proof-of-concept HCC migration and invasion model with a biomimetic fibrous septa design to visualize HepG2 cell invasive behavior that was consistent with our findings at the genetic level.

To the best of our knowledge, this is the first report for DLP-based 3D bioprinting of liver dECM-based hydrogels with tunable mechanical properties to study HCC growth and invasion in a diseased mechanical environment. Moreover, this *in vitro* dECM-based 3D biomimetic liver platform can be used to model the behavior of various liver cancer cells under specific fibrotic environments to help elucidate disease mechanisms in biological studies and for applications in preclinical drug screening.

4.2 Results and discussion

4.2.1 Photocrosslinkable liver dECM materials with key liver ECM components for rapid 3D printing

To develop photocrosslinkable liver dECM-based hydrogel materials for DLP-based rapid 3D bioprinting, liver dECM was combined with photocrosslinkable GelMA to produce a printable solution. The liver decellularization process involved sequential steps of detergent-based washing, pepsin solubilization, freeze drying, and cryomilling to produce a fine liver dECM powder that can be reconstituted upon use, as described in chapter 2. Here, our DLP-based 3D bioprinter that uses a DMD chip to generate layered, digital optical patterns for photopolymerization was used to fabricate liver dECM-based scaffolds with user defined design. More specifically, a hexagonal digital pattern with dimensions adjusted to approximate the size of one liver lobule (1 mm diameter) was used

for printing the dECM-based scaffolds (Figure 1a). The printed constructs were stained and visualized for the presence of key ECM components. Overall, the dECM-GelMA hydrogels showed positive staining of collagen I, collagen IV, fibronectin, and laminin similar to those observed in the liver dECM stains (Figure 1b). Together, we showed that combining liver dECM with GelMA produced a photocrosslinkable solution that can be readily printed into hexagonal lobule shapes using DLP-based rapid 3D bioprinting.

Liver dECM biomaterials have been used in *in vitro* liver cell culture with increasing popularity due to its capability to provide a complex tissue-specific ECM microenvironment (17–19). ECM proteins including GAG, collagen I, collagen IV, fibronectin, and laminin were all present in the dECM-based scaffolds demonstrating the successful preservation of key ECM components necessary for supporting cell culture. The development of a photocrosslinkable liver dECM-based hydrogel biomaterial enabled the use of liver dECM for DLP-based rapid 3D bioprinting, which has not been previously reported. Such application allows researchers to readily print dECM-based hydrogel constructs with complex shape and pre-determined mechanical properties at high resolution within seconds.

4.2.2 Effects of liver dECM hydrogel materials on HCC culture

Upon successful liver decellularization to produce a photocrosslinkable dECM-based hydrogel, *in vitro* culture studies using HepG2 cells, a widely used HCC line, were performed to examine the cell viability and liver-specific gene expression of encapsulated cells. Here, we compared the culture of HepG2 cells using liver dECM-based scaffolds to

collagen I-based scaffolds and GelMA scaffolds, which have been commonly used in liver cell culture and for creating tissue engineered liver constructs (22, 25). To eliminate possible effects contributed by the scaffold mechanical properties on HepG2 cell viability and expression profile, the stiffness of all three scaffolds were kept within the healthy liver range (Figure 2). Viability studies demonstrated by Live/Dead^{TM} staining of the HepG2 cells over 7 days showed a similar level of viability in the liver dECM and collagen I-based scaffolds, however, a lower number of live cells were observed in the GelMA scaffolds at the 3-day and 7-day time points (Figure 3a). Fluorescence images of HepG2 cells cultured in each of the three groups all showed positive staining for both albumin (ALB) and E-cadherin (ECAD), suggesting that all three types of scaffolds supported albumin production and epithelial cell junction formation (Figure 3b). Furthermore, a significantly lower expression of the proliferation marker gene *MKI67* in cells cultured in GelMA was observed when compared to the liver dECM-based and collagen I-based scaffolds at 7 days (Figure 3c), which is consistent with the observed lower viability stains in the GelMA samples at 7 days. There was also a trend for higher expression of the metabolic markers *ALB* and *AFP* in cells cultured in liver dECM-based scaffolds than those in other two groups (Figure 3c). Collectively, these results demonstrate that the addition of liver dECM and collagen into the GelMA scaffolds better supported the viability of HepG2 cells compared to GelMA scaffolds alone, and that liver dECM-based scaffolds supported the highest level of expression of proliferation and metabolic markers overall.

The printed liver dECM-based scaffolds supported the culture of encapsulated HepG2 cells over 7 days *in vitro* as well as the expression of key liver genes and proteins.

In particular, a similar number of viable cells in the dECM-based and collagen I-based hydrogels demonstrated that our liver dECM material was comparable to traditionally used collagen I for HepG2 cell culture. Fluorescent images confirmed the presence of liver albumin and epithelial marker in the HepG2 cell encapsulated dECM-based, collagen I-based, and GelMA scaffolds. These positive results are consistent with literature findings that liver dECM, GelMA, and collagen I support HepG2 cell and hepatocyte viability and morphology (19, 22, 26). A further evaluation of gene expression revealed a better supportive role of the liver dECM-based scaffold on HepG2 cells than collagen I-based and GelMA scaffolds, as evident by the higher relative expression of *ALB, AFP, and MKI67*. This is consistent with the role of decellularized ECM scaffolds as a cell-instructive substrate to promote cell functionality and phenotype in a tissue-specific manner (27, 28).

4.2.3 Tuning stiffness of liver dECM materials to match cirrhotic liver

The improved viability and gene expression of HepG2 cells in the printed liver dECM-based scaffolds encouraged us to further explore the possibility of creating scaffolds with well-defined mechanical properties. We first investigated the relationship between printing conditions and scaffold mechanical property using our rapid 3D bioprinter. By varying the exposure time regionally, mechanical properties can be easily changed within the same construct (Figure 4a). Similarly, scaffolds of uniform mechanical property can be printed using the corresponding exposure time (Figure 4b). Mechanical testing measurements of the liver dECM-based constructs demonstrated a positive linear relationship between stiffness and exposure time as shown in Figure 4c. In particular, three

different exposure times of 10 s, 20 s, and 40 s were chosen to produce scaffolds with stiffness values of approximately 0.5 kPa, 5 kPa and 15 kPa, which each corresponds to the softer than healthy range (soft), healthy liver range (medium), and cirrhotic range (stiff), respectively (29). Using these printing conditions, both acellular and cell-embedded scaffolds were fabricated and stiffness measurements were performed to determine the stability of the scaffolds across the 7-day culture period. In this case, the changes in stiffness over 7 days were not significant for all conditions in scaffolds with and without cells (Figure 4d and e). Overall, these results indicate that the rapid 3D bioprinting of liver dECM-based scaffolds provided a robust and stable mechanical environment for HepG2 cells over the entire culture period.

In this work, our rapid DLP-based 3D bioprinting technology enabled the flexible design of physiologically relevant geometries as well as precise control over hydrogel mechanical properties. By changing the light exposure time, changes in stiffness can be easily controlled without modifying the hydrogel components and thus eliminating effects contributed by different material concentrations or chemical composition on cell behavior. Notably, this capability to create complex acellular and cell-embedded dECM-based hydrogel constructs has not yet been achieved by other 3D bioprinting platforms in liver tissue engineering (20, 30).

4.2.4 Effect of matrix stiffness on hydrogel pore size and molecular diffusion

Increased stiffness from material crosslinking could vary the pore size of the hydrogel scaffolds thus pose potential impact on molecular diffusion to cells and affect

cellular behavior. To study the impact on pore size from varying scaffold stiffness, scanning electron microscope images of soft, medium and stiff scaffolds were taken (Figure 5a). Large pores were found in soft scaffold whereas smallest pored were observed in stiff scaffold. Despite the pore size variation, the diameter of the pores in stiff scaffolds was still in the range of 10-20μm, comparable to the average size of animal cells. To further study the impacts on molecular diffusion, diffusion profiles of fluorescent dextran molecules (4.4 kDa and 60-85 kDa respectively) into the printed constructs were compared between the soft, medium and stiff scaffolds over time (Figure 5b and c). No significant differences were observed in the amount of diffusion into each of the scaffolds at each time point (Figure 5d and e). This indicated that increasing stiffness posed no significant impact on the diffusion of molecules with sizes larger than most growth factors.

The decreasing trend of hydrogel scaffold pore size with increased crosslinking and thus increased stiffness observed here is consistent with the literature reports. The pore size observed in the stiff scaffolds is large enough for cells to move through and therefore should not provide significant barrier to growth factor diffusion through the scaffold. This is further proven by the diffusion profiles of 60-85 kDa dextran molecules across all scaffolds. These similar diffusion profiles of dextran molecules into soft, medium and stiff constructs suggested that the difference in cell behavior cultured in scaffolds of varied stiffness should not be caused by the molecular diffusion variation.

4.2.5 Effects of matrix stiffness on HCC growth

99

To better understand how varying liver dECM-based matrix stiffness affects liver cancer cell growth and invasion potential, viability, spheroid formation, and gene expression of encapsulated HepG2 cells were characterized. First, Live/Dead^{TM} staining was performed on all three stiffness groups one day following printing (Figure 6a). Quantification of live cell number showed greater than 80% viability in all groups with no significant difference between samples under different exposure times or stiffness values, which verified that the fabrication conditions did not negatively impact initial cell viability (Figure 6b). Next, the cell viability and growth of HepG2 cells in the bioprinted liver dECM-based scaffolds of different stiffness were then monitored over 7 days (Figure 6c). For scaffolds with soft and medium stiffness, cellular aggregation and spheroid formation was observed 3 days post printing with increasing spheroid size during the entire culture period. In contrast, only a few small aggregates were formed by HepG2 cells cultured in the stiff scaffolds. Measurements of the spheroid size for each stiffness group confirmed that a significantly higher growth of HepG2 cells was observed when cultured in the soft and medium scaffolds compared to minimal growth in the stiff dECM-based scaffolds (Figure 6c).

To further confirm these observations, the expression of proliferation, apoptosis markers, and common liver-specific markers were investigated on day 7 of culture. No significant differences in expression for all markers was observed between cells cultured in soft and medium scaffolds. However, a significantly lower expression in the *MKI67, ALB*, and *AFP* was observed in HepG2 cells cultured in the stiff scaffolds along with a higher expression of the apoptosis marker *CASP8* (Figure 7a). These results demonstrated

that HepG2 cells exhibited a lower viability and slower growth when cultured in the stiff dECM-based scaffolds, and showed that a cirrhotic matrix stiffness significantly downregulated the expression of the liver-specific markers *ALB* and *AFP*.

The high viability of HepG2 cells observed in all conditions one day after printing confirmed that the variation in 3D bioprinting exposure time did not affect initial cell viability. However, a decrease in HepG2 cell viability on day 3 and 7 of culture with considerably smaller spheroid size indicated that there was significant growth restriction on HepG2 cells when embedded in dECM-based scaffolds with a stiffness similar to cirrhotic liver. These findings are consistent with literature reports on reduced viability and growth in cancer cells cultured in stiff 3D hydrogels (9, 31). A further evaluation on the gene expression confirmed these results as attributed by the lower levels of the proliferation marker *MKI67*, *ALB*, and *AFP* expression coupled with higher levels of the apoptosis marker *CASP8*. Overall, a stiff scaffold similar to that of cirrhotic liver markedly reduced liver-specific gene expression and cell proliferation in HepG2 cells, and supports the hypothesis that a cirrhotic mechanical environment plays a significant role in liver function impairment in patients with cirrhosis and HCC (32).

4.2.6 Effects of cirrhotic matrix stiffness on HCC invasion potential

Following the investigation of cancer cell growth, the impact of dECM-based scaffold stiffness on the migration and invasion potential of encapsulated HepG2 cells was assessed. The expression of insulin-like growth factor 2 (*IGF2*), which encodes for the angiogenesis factor that could accelerate tumor progression (33), was significantly higher

101

in HepG2 cells cultured in the stiff scaffolds as compared to the soft and medium scaffolds after 7 days (Figure 7b). Additionally, the expression of major matrix metalloproteinases (MMPs) *MMP2* and *MMP9* involved in HCC invasion were also upregulated in the stiff scaffolds as compared to the soft and medium conditions. Furthermore, a significantly higher expression of Twist-related protein 1 (*TWIST1*), which is correlated with HCC metastasis through the induction of epithelial-to-mesenchymal transition (EMT) (34), was observed in HepG2 cells cultured in the stiff and medium scaffolds (Fig. 4E).

The impacts of the cirrhotic matrix on HepG2 cell migratory and invasive behavior is critical in better understanding the observed increase in liver cancer malignancy under cirrhotic conditions (2). Significantly elevated expression of *IGF2* in HepG2 cells cultured in scaffolds with cirrhotic liver stiffness suggests that this disease-related mechanical environment could potentially accelerate tumor progression (33). Both *MMP2* and *MMP9* encode for key enzymes involved in degradation of basement membrane proteins and are closely correlated to HCC tumor invasion, metastasis, and recurrence (35). More specifically, the high expression of both *MMP2* and *MMP9* in the stiffest scaffold points to an increased potential for migration and invasion behavior of HCC cells due to the cirrhotic mechanical environment. In particular, significantly higher *MMP9* expression is strongly correlated to a more advanced tumor stage and higher HCC recurrence risk (36). These findings may help partially explain the high mortality rate in patients with HCC since its development is strongly coupled with liver cirrhosis (1, 2). Furthermore, the higher expression of *TWIST1* in HepG2 cells cultured in both the medium and stiff scaffolds also indicated a higher possibility of EMT induction and HCC metastasis within a cirrhotic

102

environment (34). Together, these results demonstrated that a stiffer dECM-based scaffold induced an upregulation of genes encoded for ECM degradation enzymes and key transcriptional factors involved in EMT, which suggest a higher migration and invasion potential in these liver cancer cells.

4.2.7 Establishment of a 3D printed platform to visualize stromal invasion in response to stiffness

Encouraged by the results from the gene expression profile, we developed a 3D bioprinted liver cancer invasion model to aid in visualizing the potential migration and invasion of HepG2 cells into surrounding tissues when cultured under various stiffness. The biomimetic design consists of three hexagonal lobules each possessing different stiffness that correspond to the soft, medium, and stiff scaffolds established prior. Each hexagonal unit is interconnected with a collagen I-based scaffold to represent the fibrous septa-like structure found in the fibrotic liver architecture. To monitor cell invasion from each hexagonal lobule into the surrounding collagenous septa, HepG2 cells in each region were stained using fluorescent CellTracker^{TM} dye (i.e. red = soft, green = medium, yellow = stiff).

A total of four digital patterns were designed to print the final 3D liver cancer model (Figure 8a) in which three hexagonal patterns were used to print regions of three different stiffness and the last pattern for mimicking the inter-lobule fibrous septa. To minimize the possible effects of stiffness of the surrounding septa on HepG2 cell invasion, the collagen I-based septa regions were printed at similar mechanical properties as the healthy medium

stiffness dECM-based hexagon. Here, acellular constructs were first printed to test the feasibility of this printing approach followed by the printing of cell-embedded constructs (Figure 8b).

Fluorescence and bright field images of the liver cancer invasion model were evaluated over 7 days. A minimal amount of outgrowth from each of the hexagonal regions was observed across all conditions following the first day of culture. After 3 and 7 days of culture, an increased number of HepG2 cells was observed in the collagen septa region from the stiff scaffold, whereas fewer cells were observed crossing the septa-lobule boundary from the soft and medium conditions (Figure 8c). To quantify the area of HepG2 cell outgrowth, all three hexagonal regions in the fluorescence images were blacked out and the cells present in the collagen septa region was quantified (Figure 8d). In this case, there was a significantly higher area of cellular outgrowth from the stiff matrix than from the other two conditions at 3 and 7 days (Figure 8e). Taken together, this bioprinted liver cancer invasion model could be used to visualize and quantify the invasion of HCC cells into the surrounding stromal regions. In this case, HepG2 cells cultured in a cirrhotic mechanical environment showed the highest degree of invasion into the adjacent septa regions. These observations were consistent with their high migration and invasion potential as observed at the genetic level for the stiff scaffolds.

The ability to visualize increase in migration and invasion behavior induced by the cirrhotic matrix stiffness would be a valuable *in vitro* tool for monitoring cancer cell dynamics under diseased conditions. Common *in vitro* cancer migration and invasion platforms use traditional approaches such as scratch assays, transwell cell invasion assays,

and spheroid encapsulation invasion assays (37, 38). While these studies contribute some information on the tendency of cancer cell migration, they are very limited in providing a biomimetic 3D environment to recapitulate the stromal invasion process where liver cancer cells demonstrate invasive growth into the portal tracts and fibrous septa. Here, the establishment of a 3D liver cancer invasion model that incorporates the fibrous septa between liver nodules of varied stiffness served as a biomimetic platform to visualize the effect of cirrhotic matrix stiffness on the invasion of HepG2 cells into the fibrous septa regions. In particular, the ability to rapidly and precisely pattern different cells and biomaterials into their assigned locations using our 3D bioprinting platform enabled the fabrication of the complex native liver microarchitecture with micron scale resolution. By labelling the cells with different fluorescent CellTracker^{TM} dyes corresponding to scaffolds of different stiffness, the encapsulated HepG2 cells could be easily and clearly tracked in a visual manner for invasion behavior. In this design, the collagen I-based septa region was chosen to have a stiffness matched to the dECM-based hexagon of medium stiffness to reduce any potential for spontaneous outgrowth of HepG2 cells from the dECM-based lobules into the collagen I-based septa regions due to abnormal mechanical properties. Furthermore, a minimal amount of invasion of HCC occurred when they were cultured in the medium stiffness condition, thus suggesting that the cells did not migrate towards the collagen I-based septa regions because of differences in biomaterial composition. Interestingly, a higher degree of invasion into the surrounding septa regions of HepG2 cells originating from the stiff hexagonal region demonstrated that HCC cells cultured in a cirrhotic matrix stiffness were more invasive as compared to those in healthy or softer

105

matrices. Therefore, we conclude that the increased migratory and invasive behavior observed in this biomimetic liver cancer invasion model is primarily due to the cirrhotic scaffold stiffness. These results have profound implications that high stiffness alone in a cirrhotic liver could play a significant role to potentiate cancer stromal invasion and future metastasis. Furthermore, liver tissue mechanical property, currently used as a fibrosis diagnostic marker and HCC risk prediction (29), could later be identified as a therapeutic target for reducing HCC invasion and metastasis in patients with advanced fibrotic and cirrhotic liver disease.

4.3 Acknowledgments

Chapter 4, in full, has been submitted for publication of the material as it may appear in the Journal of Biomaterials, 2018, Ma X, Yu C, Wang P, Xu W, Wan X, Lai CSE, Liu J, Koroleva-maharajh A, Chen SC. The dissertation author was the primary

investigator and author of this paper.

Figure 4-1. Characterization of printed liver dECM scaffolds. (a) Digital pattern designed for bioprinting and the bright field image showing printed scaffolds using the pattern (scale bar = 500 μm). (b) Fluorescence images showing positive staining of collagen I, collagen IV, fibronectin, and laminin in pure liver dECM material and dECM-based scaffolds (scale bar = 200 μm).
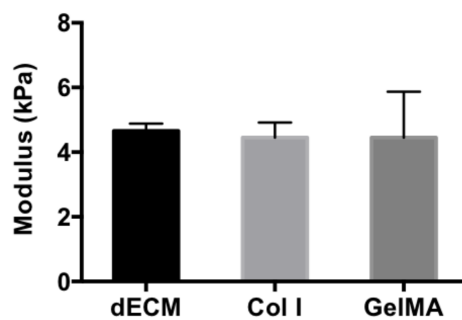
Figure 4-2. Mechanical property characterization of liver dECM-based, collagen I-based, and GelMA scaffolds. Compressive modulus of liver dECM-based (dECM), collagen I-based (Col I), and GelMA hydrogel scaffolds. Error bars represent SEM, and n = 3 for all data points.
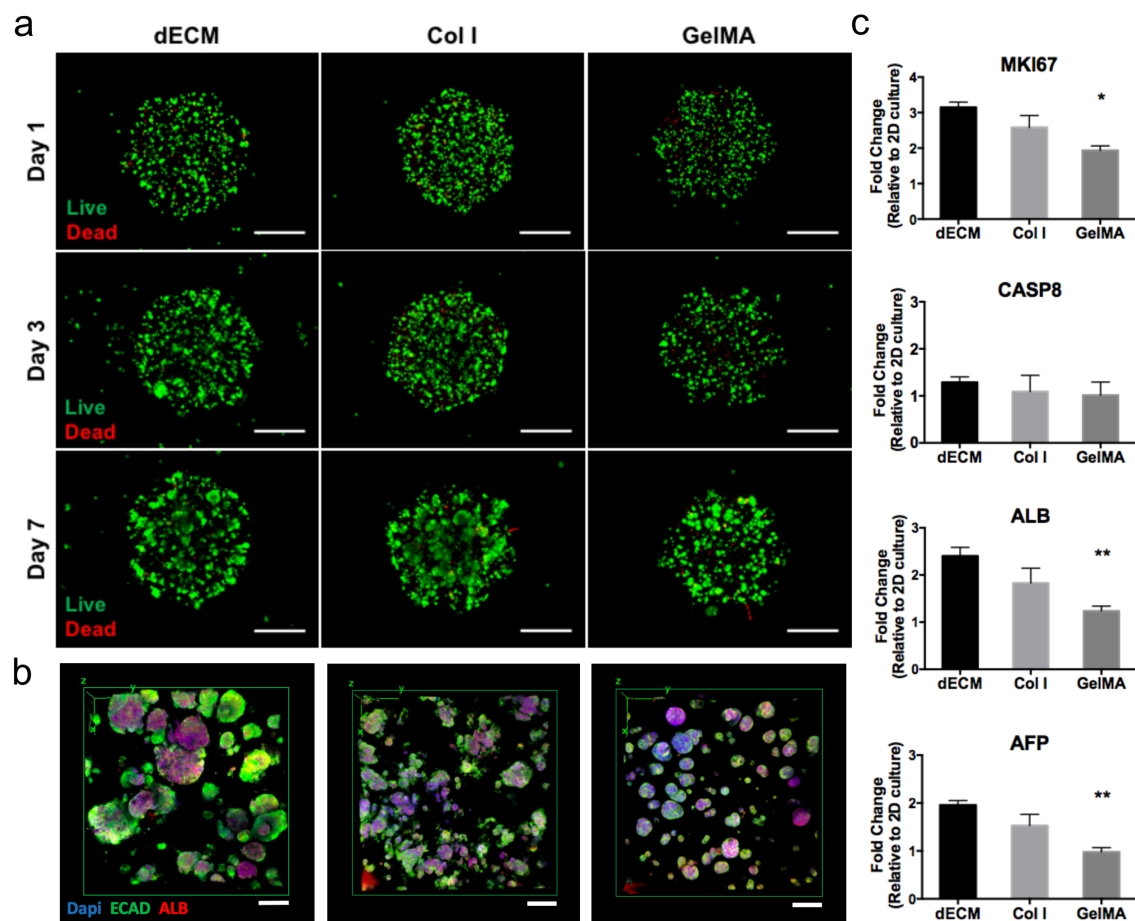
Figure 4-3. Characterization of HepG2 cells cultured in dECM-based, collagen I-based, and GelMA constructs. (a) Fluorescence images showing Live/Dead^{TM} stain of HepG2 cells cultured in dECM-based (dECM), collagen I-based (Col I), and GelMA constructs over 7 days (scale bar = 500 μm). (b) Fluorescence images showing staining of E-cadherin (ECAD) and albumin (ALB) in HepG2 cells cultured in dECM-based, collagen I-based, and GelMA constructs on day 7 (scale bar = 100 μm). (c) Gene expression analysis of MKI67, CASP8, ALB, and AFP of HepG2 cells cultured in dECM-based, collagen I-based and GelMA constructs on day 7. Error bars represent SEM, and n = 3 for all data points. *P ≤ 0.05, **P ≤ 0.01.
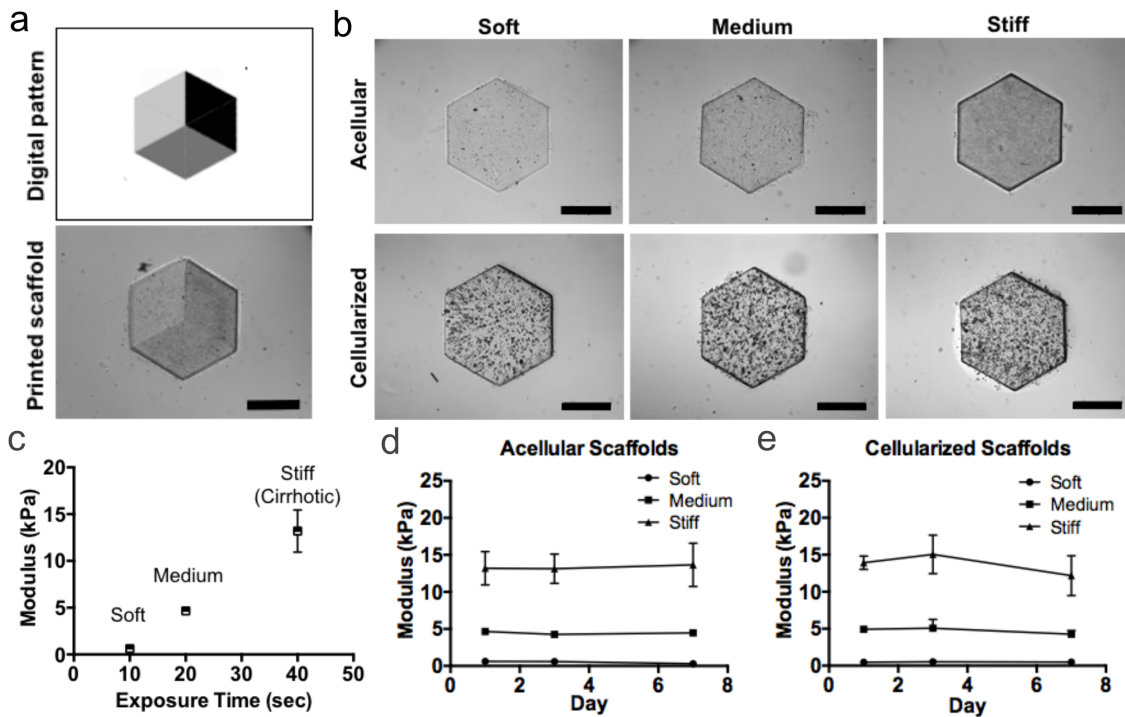
Figure 4-4. 3D bioprinted liver dECM-based scaffolds with tunable stiffness. (a) Digital pattern (top) with greyscale used to control the exposure time in which the darker color corresponds to longer exposure time, and the bright field image (bottom) showing printed scaffolds using the pattern in which darker grey scale regions represent increased stiffness (scale bar = 500 μm). (b) Bright field images showing acellular and cellularized dECM-based scaffolds with three stiffness values (scale bar = 500 μm). (c) Plot showing the relationship between scaffold compressive modulus and printing exposure time one day after printing. Error bars represent SEM, and n = 3 for all data points. (d) Quantitative plot showing the compressive moduli of acellular scaffolds over 7 days. Error bars represent SEM, and n = 3 for all data points. (e) Quantitative plot showing the compressive moduli of cell-embedded scaffolds over 7 days. Error bars represent SEM, and n = 5 for all data points.
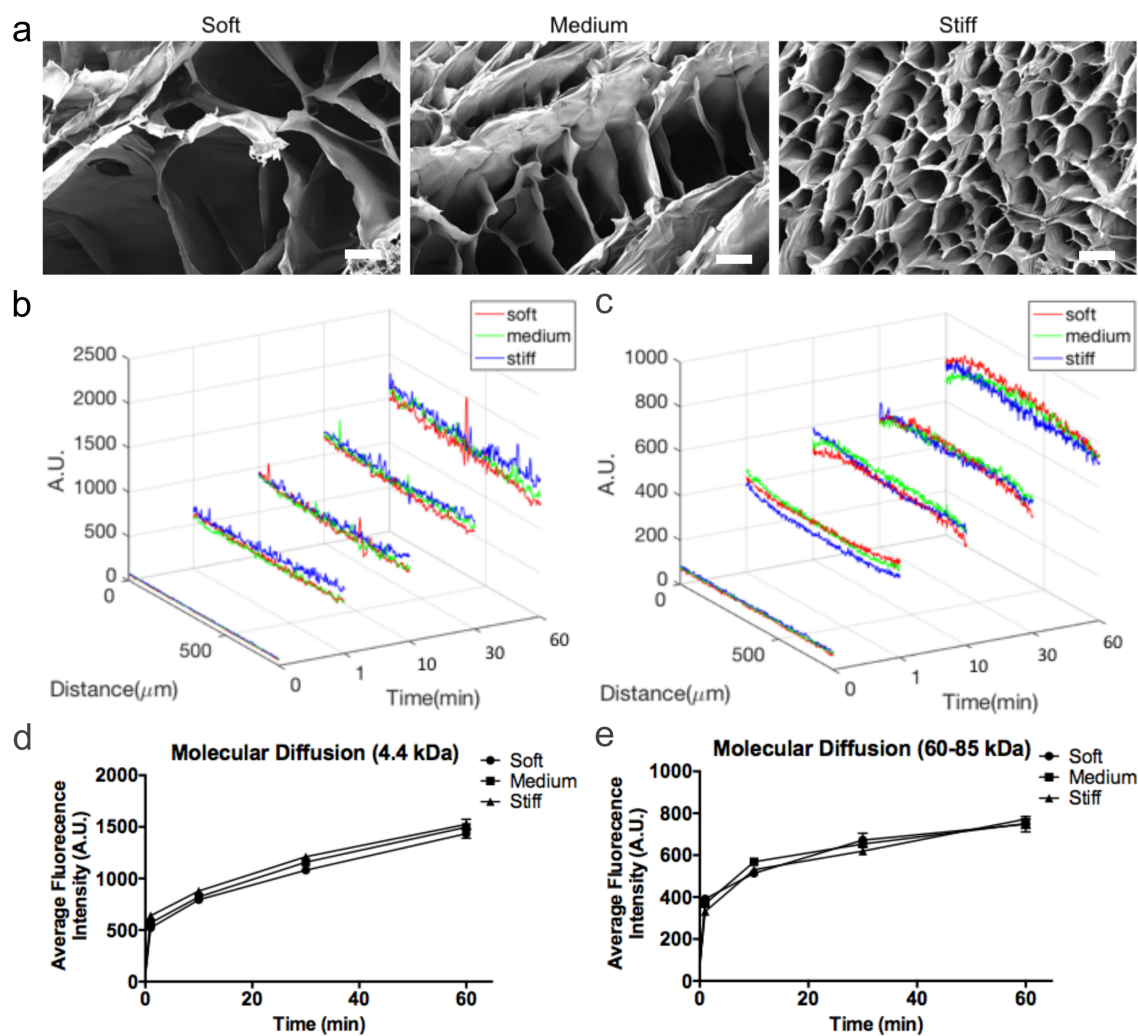
Figure 4-5. Ultrastructure and diffusion profile characterization for liver dECM-based scaffolds. (a) Scanning electron microscope images showing the ultrastructure of dECM scaffolds (scale bar = 20 µm). (b) Representative plots of fluorescence signals of 4.4 kDa TRITC-dextran molecules across the soft, medium and stiff scaffolds over time. (c) Representative plots of fluorescence signals of 60-85 kDa TRITC-Dextran molecules across the soft, medium and stiff scaffolds over time. (d) Quantitative plot showing the average fluorescence intensity of dextran molecules (4.4 kDa) diffused into 3D printed dECM-based scaffolds. Error bars represent SEM, and n = 4 for all data points. (e) Quantitative plot showing the average fluorescence intensity of dextran molecules (60-85 kDa) diffused into 3D printed dECM-based scaffolds. Error bars represent SEM, and n = 4 for all data points.
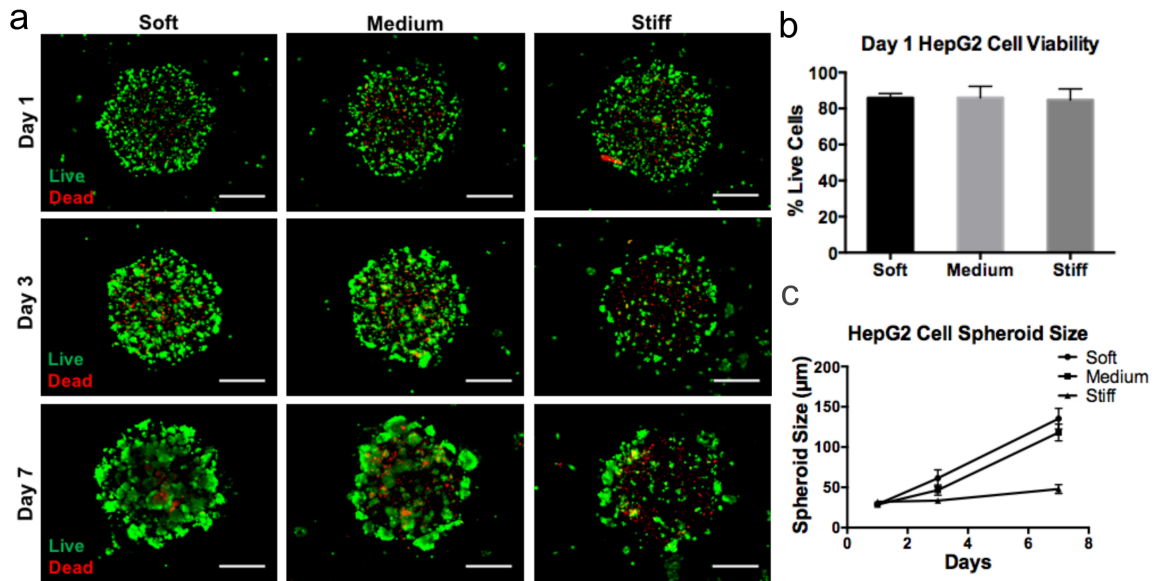
Figure 4-6. Characterization of HCC growth in dECM-based scaffolds with varied stiffness. (a) Fluorescence images showing Live/Dead[TM] stain of HepG2 cells cultured in soft, medium, and stiff scaffolds over 7 days (scale bar = 500 µm). (b) Quantification of viable cell percentage in scaffolds of varied stiffness one day following cell encapsulation. Error bars represent SEM, and n = 3 for all data points. (c) Quantitative plot showing changes in HCC spheroid size over time under soft, medium, and stiff conditions. Error bars represent SEM, and n = 3 for all data points.
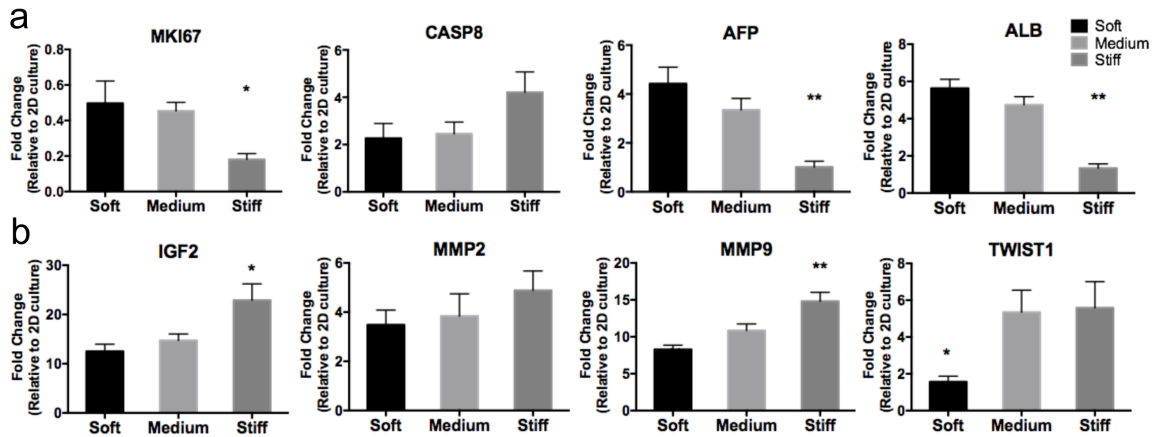
**Figure 4-7**. Characterization of HCC gene expression in dECM-based scaffolds with varied stiffness. (a) Gene expression of MKI67, CASP8, ALB, and AFP of HepG2 cells cultured in soft, medium, and stiff conditions of dECM-based scaffolds on day 7. (b) Gene expression of IGF2, MMP2, MPP9, and TWIST1 in HepG2 cells cultured in scaffolds of varied stiffness. Error bars represent SEM, and n = 4 for all data points. *P ≤ 0.05, **P ≤ 0.01.

Figure 4-8. 3D bioprinted liver cancer invasion model with varied scaffold stiffness. (a) Hexagonal patterns used to print regions of varied stiffness (first three patterns) and fibrous septa in between the lobules. (b) Bright field images showing printed scaffolds without and with cells (scale bar = 500 µm). (c) Merged fluorescence and paired bright field images showing the tracked HepG2 cell locations relative to their assigned hexagonal regions over 7 days. Red = soft, green = medium, yellow = stiff condition. (scale bar = 500 µm). (d) Fluorescence images (top row) showing the highlighted outgrowth area of cells from the hexagonal scaffolds of varied stiffness over time (scale bar = 500 µm), and circled regions (bottom row) in the same set of images for area quantification. (e) Quantitative plot showing the percent area of cell invasion originating from the three different scaffolds over time. Error bars represent SEM, and n = 5 for all data points. **P ≤ 0.01, ***P ≤ 0.001.
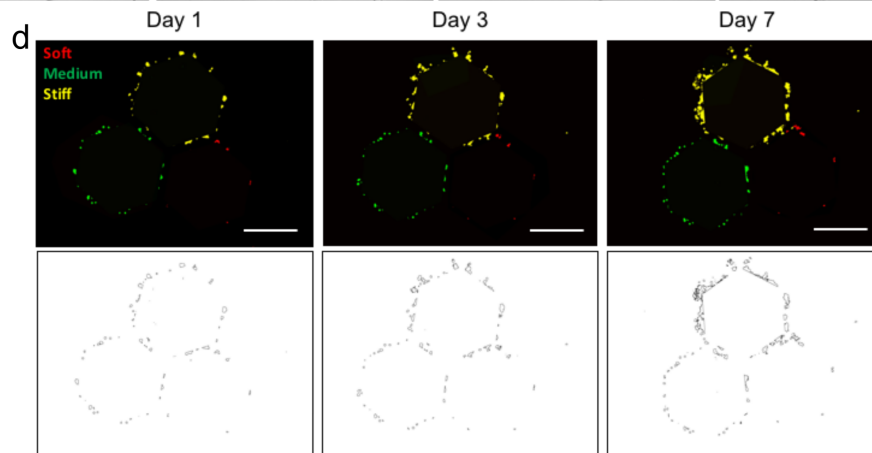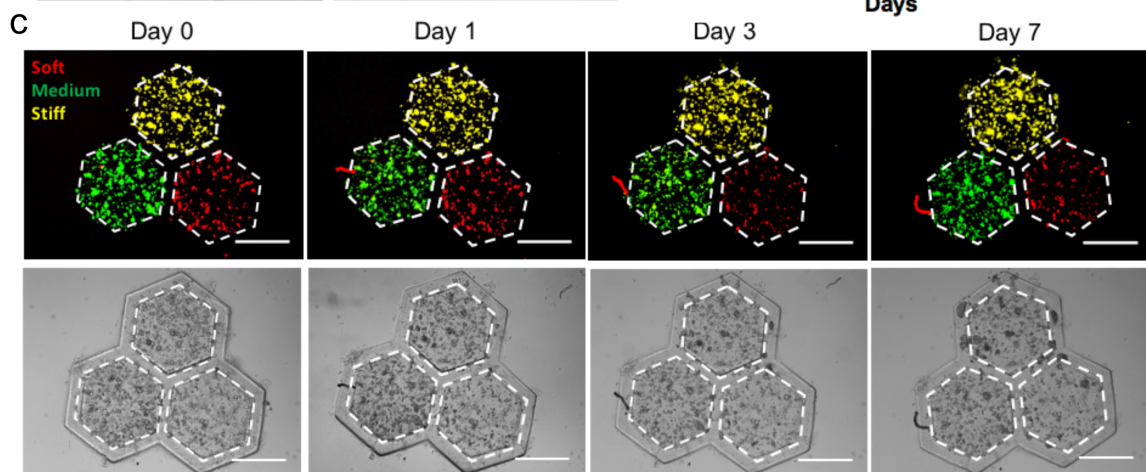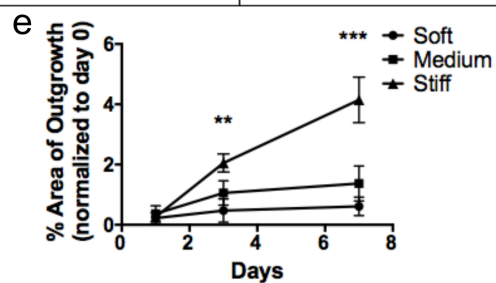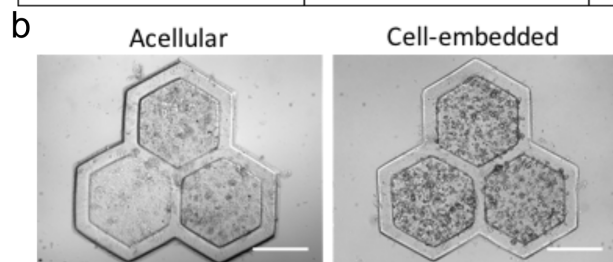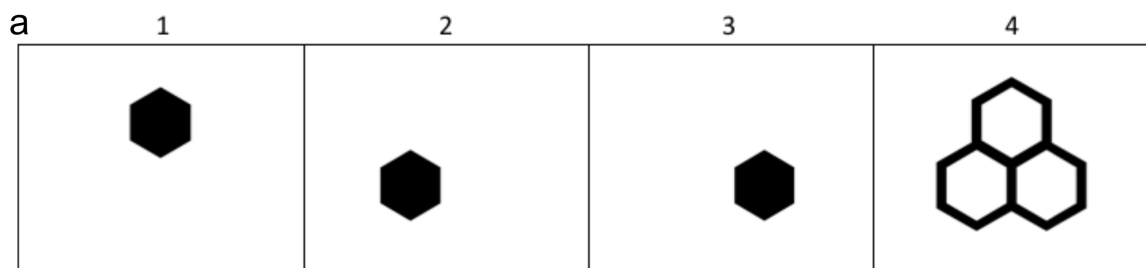
4.4 References

1.	J. Ferlay, I. Soerjomataram, R. Dikshit, S. Eser, C. Mathers, M. Rebelo, D. M. Parkin, D. Forman, and F. Bray, "Cancer incidence and mortality worldwide: Sources, methods and major patterns in GLOBOCAN 2012," Int. J. Cancer **136**, E359–E386 (2015).

2.	G. Fattovich, T. Stroffolini, I. Zagni, and F. Donato, "Hepatocellular carcinoma in cirrhosis: incidence and risk factors.," Gastroenterology **127**, S35-50 (2004).

3.	D. Schuppan and N. H. Afdhal, "Liver cirrhosis.," Lancet **371**, 838–851 (2008).

4.	R. Masuzaki, R. Tateishi, H. Yoshida, T. Sato, T. Ohki, T. Goto, H. Yoshida, S. Sato, Y. Sugioka, H. Ikeda, S. Shiina, T. Kawabe, and M. Omata, "Assessing liver tumor stiffness by transient elastography," Hepatol. Int. **1**, 394–397 (2007).

5.	W. Ling, Q. Lu, C. Lu, J. Quan, L. Ma, J. Li, D. He, J. Liu, J. Yang, T. Wen, H. Wu, H. Zhu, and Y. Luo, "Effects of vascularity and differentiation of hepatocellular carcinoma on tumor and liver stiffness: In vivo and in vitro studies," Ultrasound Med. Biol. **40**, 739–746 (2014).

6.	F. Kondo, "Histological features of early hepatocellular carcinomas and their developmental process: for daily practical clinical application," Hepatol Int **3**, 283–293 (2009).

7.	J. Schrader, T. T. Gordon-Walker, R. L. Aucott, M. van Deemter, A. Quaas, S. Walsh, D. Benten, S. J. Forbes, R. G. Wells, and J. P. Iredale, "Matrix stiffness modulates proliferation, chemotherapeutic response, and dormancy in hepatocellular carcinoma cells," Hepatology **53**, 1192–1205 (2011).

8.	A. D. Doyle and K. M. Yamada, "Mechanosensing via cell-matrix adhesions in 3D microenvironments," Exp. Cell Res. **343**, 60–66 (2016).

9.	M. K. Aparnathi, J. S. Patel, and P. D. Patel, "Effect of gel porosity and stiffness on culture of HepG2 cells encapsulated in gelatin methacrylate hydrogels," Biosci. Biotech. Res. Comm. **9**, 463–470 (2016).

10.	R. Zhang, M. Ma, G. Dong, R.-R. Yao, J.-H. Li, Q.-D. Zheng, Y.-Y. Dong, H. Ma, D.-M. Gao, J.-F. Cui, Z.-G. Ren, and R.-X. Chen, "Increased matrix stiffness promotes tumor progression of residual hepatocellular carcinoma after insufficient heat treatment.," Cancer Sci. **108**, 1778–1786 (2017).

11.	Y. You, Q. Zheng, Y. Dong, Y. Wang, L. Zhang, T. Xue, X. Xie, C. Hu, Z. Wang, R. Chen, Y. Wang, J. Cui, and Z. Ren, "Higher matrix stiffness upregulates

osteopontin expression in hepatocellular carcinoma cells mediated by integrin β1/GSK3β/β-catenin signaling pathway," PLoS One **10**, e0134243 (2015).

12. C. Liu, Y. Liu, H. Xie, S. Zhao, X. Xu, L. Fan, X. Guo, T. Lu, G.-W. Sun, and X. Ma, "Role of three-dimensional matrix stiffness in regulating the chemoresistance of hepatocellular carcinoma cells," Biotechnol. Appl. Biochem. **62**, 556–562 (2015).

13. S. Pradhan, I. Hassani, J. M. Clary, and E. A. Lipke, "Polymeric biomaterials for in vitro cancer tissue engineering and drug testing applications.," Tissue Eng. Part B. Rev. **22**, 470–484 (2016).

14. B. E. Uygun, A. Soto-Gutierrez, H. Yagi, M.-L. Izamis, M. A. Guzzardi, C. Shulman, J. Milwid, N. Kobayashi, A. Tilles, F. Berthiaume, M. Hertl, Y. Nahmias, M. L. Yarmush, and K. Uygun, "Organ reengineering through development of a transplantable recellularized liver graft using decellularized liver matrix," Nat. Med. **16**, 814–820 (2010).

15. G. Mazza, K. Rombouts, A. Rennie Hall, L. Urbani, T. Vinh Luong, W. Al-Akkad, L. Longato, D. Brown, P. Maghsoudlou, A. P. Dhillon, B. Fuller, B. Davidson, K. Moore, D. Dhar, P. De Coppi, M. Malago, and M. Pinzani, "Decellularized human liver as a natural 3D-scaffold for liver bioengineering and transplantation," Sci. Rep. **5**, 13079 (2015).

16. P. M. Baptista, M. M. Siddiqui, G. Lozier, S. R. Rodriguez, A. Atala, and S. Soker, "The use of whole organ decellularization for the generation of a vascularized liver organoid," Hepatology **53**, 604–617 (2011).

17. K.-M. Park, K. H. Hussein, S.-H. Hong, C. Ahn, S.-R. Yang, S.-M. Park, O.-K. Kweon, B.-M. Kim, and H.-M. Woo, "Decellularized liver extracellular matrix as promising tools for transplantable bioengineered liver promotes hepatic lineage commitments of induced pluripotent stem cells," Tissue Eng. Part A **22**, 449–460 (2016).

18. Y. Wang, C.-B. Cui, M. Yamauchi, P. Miguez, M. Roach, R. Malavarca, M. J. Costello, V. Cardinale, E. Wauthier, C. Barbier, D. A. Gerber, D. Alvaro, and L. M. Reid, "Lineage restriction of human hepatic stem cells to mature fates is made efficient by tissue-specific biomatrix scaffolds," Hepatology **53**, 293–305 (2011).

19. Y. Cheng, Y. Wang, Y. Z. Kang, P. Y. Hu, Y. Gao, and M. X. Pan, "In vitro culture of tumour-derived hepatocytes in decellularised whole-liver biological scaffolds," Digestion **87**, 189–195 (2013).

20. H. Lee, W. Han, H. Kim, D.-H. Ha, J. Jang, B. S. Kim, and D.-W. Cho, "Development of liver decellularized extracellular matrix bioink for three-

dimensional cell printing-based liver tissue engineering," Biomacromolecules **18**, 1229–1237 (2017).

21. J. S. Lee, J. Shin, H. M. Park, Y. G. Kim, B. G. Kim, J. W. Oh, and S. W. Cho, "Liver extracellular matrix providing dual functions of two-dimensional substrate coating and three-dimensional injectable hydrogel platform for liver tissue engineering," Biomacromolecules **15**, 206–218 (2014).

22. X. Ma, X. Qu, W. Zhu, Y.-S. Li, S. Yuan, H. Zhang, J. Liu, P. Wang, C. S. E. Lai, F. Zanella, G.-S. Feng, F. Sheikh, S. Chien, and S. Chen, "Deterministically patterned biomimetic human iPSC-derived hepatic model via rapid 3D bioprinting," Proc. Natl. Acad. Sci. **113**, 2206–2211 (2016).

23. W. Zhu, X. Qu, J. Zhu, X. Ma, S. Patel, J. Liu, P. Wang, C. S. E. Lai, M. Gou, Y. Xu, K. Zhang, and S. Chen, "Direct 3D bioprinting of prevascularized tissue constructs with complex microarchitecture," Biomaterials **124**, 106–115 (2017).

24. M. Gou, X. Qu, W. Zhu, M. Xiang, J. Yang, K. Zhang, Y. Wei, and S. Chen, "Bio-inspired detoxification using 3D-printed hydrogel nanocomposites.," Nat. Commun. **5**, 3774 (2014).

25. Y.-J. Wang, H.-L. Liu, H.-T. Guo, H.-W. Wen, and J. Liu, "Primary hepatocyte culture in collagen gel mixture and collagen sandwich.," World J. Gastroenterol. **10**, 699–702 (2004).

26. J. V. Castell and M. J. Gomez-Lechon, "Hepatocyte Transplantation," Methods Mol. Biol. **481**, 35–46 (2009).

27. K. P. Robb, A. Shridhar, and L. E. Flynn, "Decellularized matrices as cell-instructive scaffolds to guide tissue-specific regeneration," ACS Biomater. Sci. Eng. **ASAP**, (2017).

28. Y. Zhang, Y. He, S. Bharadwaj, N. Hammam, K. Carnagey, R. Myers, A. Atala, and M. Van Dyke, "Tissue-specific extracellular matrix coatings for the promotion of cell proliferation and maintenance of cell phenotype," Biomaterials **30**, 4021–4028 (2009).

29. S. Mueller and L. Sandrin, "Liver stiffness: a novel parameter for the diagnosis of liver disease.," Hepat. Med. **2**, 49–67 (2010).

30. F. Pati, J. Jang, D.-H. Ha, S. Won Kim, J.-W. Rhie, J.-H. Shim, D.-H. Kim, and D.-W. Cho, "Printing three-dimensional tissue analogues with decellularized extracellular matrix bioink," Nat. Commun. **5**, 1–11 (2014).

31. M. Cavo, M. Fato, L. Peñuela, F. Beltrame, R. Raiteri, and S. Scaglione, "Microenvironment complexity and matrix stiffness regulate breast cancer cell activity in a 3D in vitro model," Sci. Rep. **6**, 35367 (2016).

32. M. Pinter, M. Trauner, M. Peck-Radosavljevic, and W. Sieghart, "Cancer and liver cirrhosis: implications on prognosis and management," ESMO Open **1**, e000042 (2016).

33. H. Thomas, "Liver cancer: IGF2 — an epigenetic oncodriver in HCC," Nat. Rev. Gastroenterol. Hepatol. **13**, 625–625 (2016).

34. T. K. Lee, R. T. P. Poon, A. P. Yuen, M. T. Ling, W. K. Kwok, X. H. Wang, Y. C. Wong, X. Guan, K. Man, K. L. Chau, and S. T. Fan, "Twist overexpression correlates with hepatocellular carcinoma metastasis through induction of epithelial-mesenchymal transition," Clin. Cancer Res. **12**, 5369–5376 (2006).

35. Y. Itoh, "Membrane-type matrix metalloproteinases: Their functions and regulations," Matrix Biol. **44–46**, 207–223 (2015).

36. J. P. Kuyvenhoven, B. Van Hoek, E. Blom, W. Van Duijn, R. Hanemaaijer, J. H. Verheijen, C. B. H. W. Lamers, and H. W. Verspaget, "Assessment of the clinical significance of serum matrix metalloproteinases MMP-2 and MMP-9 in patients with various chronic liver diseases and hepatocellular carcinoma," Thromb. Haemost. **89**, 718–725 (2003).

37. E. Wiercinska, H. P. H. Naber, E. Pardali, G. van der Pluijm, H. van Dam, and P. ten Dijke, "The TGF-β/Smad pathway induces breast cancer cell invasion through the up-regulation of matrix metalloproteinase 2 and 9 in a spheroid invasion model system," Breast Cancer Res. Treat. **128**, 657–666 (2011).

38. C. R. Justus, N. Leffler, M. Ruiz-Echevarria, and L. V Yang, "In vitro Cell Migration and Invasion Assays," J. Vis. Exp. 1–8 (2014).

Chapter 5 Conclusions

The work presented in this dissertation provides a theoretical and experimental basis for understanding and applying the DLP-based rapid 3D bioprinting technology to build liver tissue models *in vitro*. The 3D bioprinting of liver tissue involves the integration of appropriate cells, biomaterials and subsequent assays to build and evaluate the tissue models. With the rationale to mimic native tissue structure, cellular composition and matrix conditions, liver tissue models in healthy and disease states were developed and studied. These models demonstrate the capability of DLP-based 3D bioprinting to build novel and complex structure that mimic native liver tissues in various conditions. The studies associated with each model support the hypothesis that tissue models with increased physiological relevancy demonstrated better functional maintenance in healthy state or recapitulate liver cancer behaviors in disease state.

5.1 DLP-based 3D bioprinting as a method for building *in vitro* liver constructs

Liver lobule consists of a variety of cell types arranged in 3D complex structure. Major liver functions are tightly linked to this 3D assembly of hepatocytes with the supporting cell types from both endodermal and mesodermal origins in a hexagonal lobule unit. DLP-based 3D bioprinting platform stands out from all other types of 3D bioprinting and microfabrication approaches as one of the most suitable platform for liver tissue engineering. This is essentially due to the capability of this platform to print 3D complex liver microarchitecture with multiple cell and material inputs at microscale resolution and

within seconds. Such capability is coupled with high flexibility in biomimetic pattern design and great compatibility with a variety of biomaterials proven to support liver cell culture *in vitro*. In particular, the biomaterials used in the printing system, GelMA and liver dECM, provide great support to liver cell culture *in vitro*. By supporting good cell viability, liver-specific gene expression and functions, GelMA serves as an excellent matrix material for iPSC-derived hepatic cell culture. Similarly, Liver dECM provides great support to HCC, in particular HepG2, culture *in vitro* by supporting good cell viability, growth and gene expression.

As such, the rapid and highly flexible DLP-based bioprinting system, which includes the 3D printer, material and handling protocol, is an excellent tool for building 3D liver tissue constructs with physiologically relevant cellular arrangement and feature dimensions.

5.2 Biomimetic and functional liver model in healthy state

Recent approaches that used iPSC-derived hepatic cells to develop personalized hepatic models have been largely limited to 2D or simple 3D culture and thus lost the liver structural and cellular composition information (1–7). The complex microarchitecture and cellular interactions in liver are thought to be essential to long-term hepatocyte functional maintenance as supported by many reports on the loss of liver-specific functions from hepatocytes taken out from the liver (8, 9). The purpose of this chapter is to develop a 3D *in vitro* hepatic model that patterns iPSC-HPCs and the relevant supporting cells in a liver lobule like structure and to investigate whether this 3D tri-culture model can promote iPSC-

HPCs maturation and functional preservation in the assigned 3D biomimetic structure.

Human iPSC-derived hepatic cells, despite their potential to have malignant transformation following in vivo transplantations, have been widely recognized as the most promising candidate for developing patient-specific human hepatic models *in vitro* (2, 10). Current *in vitro* liver models using iPSC-derived hepatic cells are largely limited by their lack of biomimicry (1–7). The 3D tri-culture model presented here highlights the successful application of DLP-based bioprinting technology to liver tissue engineering and thus the progress of the field to a level where the complex liver microarchitecture and cell composition can be studied in a physiologically relevant model. Further incorporation of functional and liver-specific vasculature based on liver sinusoidal endothelial cells and introduction of diseased cell types and extracellular environment during various development stages could open the door to establishing a more sophisticated, large-scale liver model with the potential to represent relevant diseases. The hepatic model developed in this chapter provides a 3D environment for iPSC-derived hepatic cells in tri-culture with supporting cells in a hepatic lobule microarchitecture, and has the ability to facilitate *in vitro* maturation and functional maintenance of iPSC-derived hepatic cells in a biomimetic microenvironment. Hence, this model demonstrates great potential to serve as a patient-specific platform for pathophysiological studies, early drug screening, and clinical translation.

5.3 Patterning matrix stiffness to study liver cancer progression in cirrhotic condition

In recent studies examining liver cancer cell behavior in a cirrhotic mechanical environment, traditional 2D plating approaches have been met with limitations in predicting cellular responses that normally occur in a 3D *in vivo* milieu (11, 12). Furthermore, current 3D models with tunable stiffness mostly utilize simple biomaterials such as alginate and gelatin, which poorly recapitulate the complexity of the native liver microenvironment (13, 14). Cancer cell attachment and proliferation has also been demonstrated to vary depending on the type of biomaterial used (15). Thus, naturally-derived dECM materials that better represent the liver ECM composition serve as an attractive candidate for engineering tissue models for liver cancer studies. In addition, past platforms studying liver cancer cell invasion and metastasis adopt simplistic designs that lack a biomimetic structure or well-defined mechanical properties, and have less physiologically relevant tissue properties necessary for elucidating liver cancer cell migration and invasion behavior (16). To address these limitations, the goal of this chapter is to develop photocrosslinkable liver dECM and a rapid light-based 3D bioprinting process to pattern liver dECM with clinically relevant mechanical properties to serve as a biomimetic platform for HCC progression study.

In this chapter, photocrosslinkable liver dECM with well-preserved key ECM components was developed and readily printed into liver lobule architectures using DLP-based rapid 3D bioprinting. The liver dECM-based scaffolds not only supported cell viability but also provided a stable physiologically relevant mechanical environment. When encapsulated in dECM scaffolds with cirrhotic stiffness, HepG2 cells demonstrated reduced growth along with an upregulation of invasion markers compared to healthy

controls. Moreover, 3D bioprinting of liver dECM in hexagonal nodules of varied stiffness enabled visualization of stromal invasion behavior from the nodule with cirrhotic liver stiffness which were consistent with findings at the genetic level.

The successful combination of this DLP-based 3D bioprinting technology with liver dECM-based hydrogels highlights the progress of the field to a level where complex ECM materials can be utilized to create micro-patterned scaffolds with targeted physical properties for biological studies. Further optimization on the distribution of biomaterials and stiffness according to clinical data as well as incorporating relevant patient cell types could open the door to establishing a more sophisticated liver fibrosis or cirrhosis disease model with potential to serve as early anticancer drug screening platforms. The 3D bioprinted dECM-based model in this chapter allows researchers to visualize the invasive response of HCC cells in scaffolds with cirrhotic liver stiffness and demonstrates great potential as a platform technology for pathophysiological studies and drug screening in the future.

5.4 Challenges and future work

DLP-based 3D bioprinting technology presents the capability of precisely positioning biomaterials and living cells to reconstruct complex structures that can be used for disease modeling and drug screening. Current work has demonstrated the application of this technology to build liver tissue models with organ-specific functions, drug testing potentials, and disease modeling. Despite these achievements, challenges still remain on the printing platform, cells, materials, vascularization and culture methods used to build

and maintain liver tissue models to fully recapitulates the cellular organization and structural complexity comparable to native tissues.

Technological challenges with regard to DLP-based 3D printing platforms include the need for increased resolution, biocompatibility and scaling-up. Higher printing resolution is still in great demand to produce complex single cell structures like liver sinusoid networks and space of Disse. The viability of cells in printing solution decreases as printing time increases, particularly for metabolically active hepatocytes. The biocompatibility of DLP-based 3D printing platforms is considered satisfactory in the aspects of cell viability, but the impacts on the gene expression and functional aspects are largely understudied. Further studies on the mechanical and optical impacts from the bioprinting process will provide more insights into the biocompatibility of 3D printing process. Lastly, there are still challenges to the scale-up of bioprinted tissue constructs. In order to consistently generate large amount of tissue models for clinical and commercial applications, future work is needed to standardize the printers, cells, materials as well as the printing process.

There are also great limitations on the window of materials used for DLP-based 3D bioprinting. Due to the requirements to be photocrosslinkable, the types of available materials are reduced to only a few. More work is needed to develop 3D-printable and cell-compatible materials with tunability on the mechanical, chemical and biological properties to recapitulate the protein composition as well as the native liver microenvironment of the specific patient at the targeted health stage.

To apply 3D printed tissue models to personalized drug screening and disease modeling, patient specific cell sources, including human iPSC-derived cells and primary diseased cells from patients, will be the main focus. However, the maturation of differentiated hepatic cells to reach the functional level of adult hepatocytes still remains a huge challenge in the field. Moreover, the incorporation of supporting cell types, including LSECs, HSCs and KCs, derived from the same stem cell source are very rare. Research to advance human iPSC differentiation protocol into parenchymal and non-parenchymal liver cell types with high efficiency, consistency and maturation is widely demanded. Future applications of using primary diseased cells from patients to build co-culture or tri-culture platforms will also provide more insights on the development of personalized liver disease modeling.

Bioprinting technology provides the possibility to develop *in vitro* liver tissue models, but this is only the front end of the development. Further innovations on post-printing culture platforms such as bioreactors and the incorporation of microfluidic devices will be needed to assist liver functional maturation and maintenance. Vascularization of current models to incorporate perfusable vessels also helps to further recapitulate the blood flow in liver lobule. Along with these developments, technological advancement in imaging systems and analyzing tools will also be in high demand to analyze larger tissue constructs.

Overall, advancements in both research and technology in the fields of medicine, engineering, and biology will be needed to solve the above mentioned challenges to fully

realize the potential of 3D bioprinting in developing sophisticated *in vitro* liver tissue models for precision medicine.

5.5 Acknowledgments

5.6 References

1. D. Yoon No, K.-H. Lee, J. Lee, and S.-H. Lee, "3D liver models on a microplatform: well-defined culture, engineering of liver tissue and liver-on-a-chip," Lab Chip **15**, 3822–3837 (2015).

2. R. E. Schwartz, H. E. Fleming, S. R. Khetani, and S. N. Bhatia, "Pluripotent stem cell-derived hepatocyte-like cells," Biotechnol. Adv. **32**, 504–513 (2014).

3. K. Takayama, K. Kawabata, Y. Nagamoto, K. Kishimoto, K. Tashiro, F. Sakurai, M. Tachibana, K. Kanda, T. Hayakawa, M. K. Furue, and H. Mizuguchi, "3D spheroid culture of hESC/hiPSC-derived hepatocyte-like cells for drug toxicity testing," Biomaterials **34**, 1781–1789 (2013).

4. T. Takebe, K. Sekine, M. Enomura, H. Koike, M. Kimura, T. Ogaeri, R.-R. Zhang, Y. Ueno, Y.-W. Zheng, N. Koike, S. Aoyama, Y. Adachi, and H. Taniguchi, "Vascularized and functional human liver from an iPSC-derived organ bud transplant," Nature **499**, 481–484 (2013).

5. C. Du, K. Narayanan, M. F. Leong, and A. C. A. Wan, "Induced pluripotent stem cell-derived hepatocytes and endothelial cells in multi-component hydrogel fibers for liver tissue engineering," Biomaterials **35**, 6006–6014 (2014).

6. T. Takebe, R.-R. Zhang, H. Koike, M. Kimura, E. Yoshizawa, M. Enomura, N. Koike, K. Sekine, and H. Taniguchi, "Generation of a vascularized and functional human liver from an iPSC-derived organ bud transplant," Nat. Protoc. **9**, 396–409 (2014).

7. D. R. Berger, B. R. Ware, M. D. Davidson, S. R. Allsup, and S. R. Khetani, "Enhancing the functional maturity of induced pluripotent stem cell-derived human hepatocytes by controlled presentation of cell-cell interactions *in vitro*," Hepatology **61**, 1370–1381 (2015).

8. L. G. Sivaraman, A Leach, J K Townsend, S Iida, T Hogan, B J Stolz, D B Fry, R Samson, L D Tannenbaum, S R Griffith, "A microscale in vitro physiological model of the liver: predictive screens for drug metabolism and enzyme induction," Curr. Drug Metab. **6**, 569–591 (2005).

9. N. J. Hewitt, M. J. Gómez Lechón, J. B. Houston, D. Hallifax, H. S. Brown, P. Maurel, J. G. Kenna, L. Gustavsson, C. Lohmann, C. Skonberg, A. Guillouzo, G. Tuschl, A. P. Li, E. LeCluyse, G. M. M. Groothuis, and J. G. Hengstler, "Primary hepatocytes: current understanding of the regulation of metabolic enzymes and transporter proteins, and pharmaceutical practice for the use of hepatocytes in metabolism, enzyme induction, transporter, clearance, and hepatotoxicity studies,"

Drug Metab. Rev. **39**, 159–234 (2007).

10. S. N. Bhatia, G. H. Underhill, K. S. Zaret, and I. J. Fox, "Cell and tissue engineering for liver disease," Sci. Transl. Med. **6**, 245sr2 (2014).

11. J. Schrader, T. T. Gordon-Walker, R. L. Aucott, M. van Deemter, A. Quaas, S. Walsh, D. Benten, S. J. Forbes, R. G. Wells, and J. P. Iredale, "Matrix stiffness modulates proliferation, chemotherapeutic response, and dormancy in hepatocellular carcinoma cells," Hepatology **53**, 1192–1205 (2011).

12. A. D. Doyle and K. M. Yamada, "Mechanosensing via cell-matrix adhesions in 3D microenvironments," Exp. Cell Res. **343**, 60–66 (2016).

13. R. Zhang, M. Ma, G. Dong, R.-R. Yao, J.-H. Li, Q.-D. Zheng, Y.-Y. Dong, H. Ma, D.-M. Gao, J.-F. Cui, Z.-G. Ren, and R.-X. Chen, "Increased matrix stiffness promotes tumor progression of residual hepatocellular carcinoma after insufficient heat treatment.," Cancer Sci. **108**, 1778–1786 (2017).

14. Y. You, Q. Zheng, Y. Dong, Y. Wang, L. Zhang, T. Xue, X. Xie, C. Hu, Z. Wang, R. Chen, Y. Wang, J. Cui, and Z. Ren, "Higher matrix stiffness upregulates osteopontin expression in hepatocellular carcinoma cells mediated by integrin β1/GSK3β/β-catenin signaling pathway," PLoS One **10**, e0134243 (2015).

15. M. R. Carvalho, D. Lima, R. L. Reis, V. M. Correlo, and J. M. Oliveira, "Evaluating biomaterial-and microfluidic-based 3D tumor models," Trends Biotechnol. **33**, 667–678 (2015).

16. Q. F. Ye, S. X. Cai, X. Z. Dai, X. Q. Yan, M. S. Zou, and Z. Xu, "Effects of matrix viscoelasticity on HepG2 cell metastasis in a microfluidic device," J. Med. Biol. Eng. **33**, 163–170 (2013).